2-1-2016

Composition and Manufacturing Effects on Electrical Properties of Li/FeS2 Thermal Battery Cathodes

Emilee Lolita Reinholz

Emilee Lolita Reinholz

Candidate

Chemical and Biological Engineering

Department

This thesis is approved, and it is acceptable in quality and form for publication:

Approved by the Thesis Committee:

P. Randall Schunk , Chairperson

Christopher A. Apblett

Sang M. Han

Scott A. Roberts

Composition and Manufacturing Effects on Electrical Properties of Li/FeS_2 Thermal Battery Cathodes

by

Emilee Lolita Reinholz

B.S., Chemistry, Santa Clara University, 2011

THESIS

Submitted in Partial Fulfillment of the
Requirements for the Degree of

Master of Science
Chemical Engineering

The University of New Mexico

Albuquerque, New Mexico

December, 2015

Dedication

This is dedicated to Barry and Raella. Barry, without you this would not have been possible. Thank you for how selfless you have been by taking on so much extra responsibility at home and encouraging me through this. You're an incredible husband.

And to Baby Raella, you make me so proud. Daddy and I are so grateful for you and love you so much.

"Science works by experiments. It watches how things behave... And the more scientific a man is, the more (I believe) he would agree with me that this is the job of science - and a very useful and necessary job it is too. But why anything comes to be there at all, and whether there is anything behind the things science observes - something of a different kind - this is not a scientific question. If there is 'Something Behind,' then either it will have to remain altogether unknown to men or else make itself known in some different way. The statement that there is any such thing, and the statement that there is no such thing, are neither of them statements that science can make... Supposing science ever became complete so that it knew every single thing in the whole universe. Is it not plain that the questions, 'Why is there a universe?' 'Why does it go on as it does?' 'Has it any meaning?' would remain just as they were?" -C.S. Lewis, in *Mere Christianity*

Acknowledgments

I have so much to be grateful for. First of all, I thank God for the people in my life, the ability to learn, and the opportunities given to me. I thank my parents for raising me with a strong faith and a strong work ethic. You two are amazing examples for me and encouraged my love of math and science. Thank you to my husband. You are such a blessing in my life and you truly demonstrate self-sacrifice. Thank you for making this possible for our family and for me.

I sincerely thank my advisors and mentors - Scott Roberts, Chris Apblett, Jeremy Lechman, and Randy Schunk - for guiding me through this. You have taught me so much and provided both constructive feedback and encouragement throughout. Thank you for all of the time you gave me. Scott, thank you for striving for excellence in this thesis and doing your best to prepare me for a career in modeling and simulation. Thank you to Christine Roberts, David Ingersoll, and Anne Grillet, who pointed me to these wonderful people in order to learn about the world of modeling and simulation! Thank you also to my manager, Trish. You have also encouraged me and helped me obtain the opportunity to pursue higher education. Thank you to my mentor, Melecita - I couldn't have asked for a better guide or a better person to help me through my early years as a Sandian. Thank you, also, to everyone who helped me get into the UPT program. And to my committee members, thank you for taking the time to read this manuscript and for your role in my thesis defense. Thank you to all who helped me with the work described in this thesis. This includes Linda Johnson, Ashley Allen, Jon Madison, Liz Huffman, Ryan Wixom, Barry Ritchey, and Burke Kernen. Thank you to Joe Romero, Dan Bolintineau, Steve Showalter, David Noble, and Hector Mendoza, for helpful discussions related to this work.

Sandia National Laboratories is a multi-program laboratory managed and operated by Sandia Corporation, a wholly owned subsidiary of Lockheed Martin Corporation, for the U.S. Department of Energy's National Nuclear Security Administration under contract DE-AC04-94AL85000.

Composition and Manufacturing Effects on Electrical Properties of Li/FeS_2 Thermal Battery Cathodes

by

Emilee Lolita Reinholz

B.S., Chemistry, Santa Clara University, 2011

M.S., Chemical Engineering, University of New Mexico, 2015

Abstract

Li/FeS_2 thermal batteries provide a stable, robust, and reliable power source capable of long-term electrical energy storage without performance degradation. These systems rely on a eutectic salt that melts at elevated temperature, activating the cell. When the electrolyte melts, the cathode becomes a suspension, with cathode particles suspended in a molten salt. The suspension experiences mechanical deformation, or "slumping." This slump changes the mechanical compression of the cell, as well as the tortuosity and electronic and ionic conductivity of the cell as the cathode mesostructure is reordered in response to the external compressive stress. The combined effect of deformation, component composition, and manufacturing conditions on electrical conductivity has not been studied, yet the cathode electrical properties are critically important to battery performance.

This thesis presents simulation results from a computer model in combination with experiments to elucidate the effects of electrical conductivity in FeS_2 cathode pellets when composition and manufacturing parameters are varied. Experiments

applied impedance spectroscopy measurements of pressed-powder cathode pellets before and after slumping. Pellets were manufactured with variations in pellet density, FeS_2 particle size distribution, and FeS_2 content. The results showed that prior to slumping, the electrical conductivity increased with pellet density and FeS_2 content. After slumping, pellets exhibited greater electrical conductivity, but the effects of processing parameters appear to have been erased, at least within the ranges tested.

The conformal decomposition finite element method (CDFEM) was applied to surface-meshed geometric representations of cathode microstructures generated from microcomputed tomography reconstructions. Results from the SIERRA/Aria finite element code indicate that the selected processing and composition parameters do not provide a clear trend on the preslumped electrical conductivity, but density slightly affected the postslumped conductivity. These results indicate that the simulations lacked fidelity compared to experiments. However, the simulations combined with experimental data provide a fundamental look at the effects of processing and composition on thermal battery microstructure and electrical conductivity. The understanding of manufacturing effects on battery performance is not well developed, and this effort represents a step forward in correlated and predicting performance of cells based upon observed manufacturing trends.

Contents

List of Figures

List of Figures

List of Tables

Glossary

A	Cross-sectional area (m^2)
$\mathbf{E}$	Electric field
h	Mesh size (μm)
I	Current (A)
l	Sample thickness (m)
$\mathbf{J}$	Current density (A/m^2)
$\mathbf{n}$	Outward normal vector
ρ	Electrical resistivity (Ωm) or density (g/cm^3), depending on the context
R_{fit}	Resistance (Ω)
$\boldsymbol{\sigma}$	Electrical conductivity ($1/\Omega$m)
$\boldsymbol{\sigma}_{\text{eff}}$	Effective electrical conductivity ($1/\Omega$m)
r	Particle radius (μm)
V	Electric potential, or voltage (V)

Chapter 1

Introduction

Thermal batteries are primary, or non-rechargeable, molten salt batteries that activate at hundreds of degrees above room temperature. German scientists developed early versions of this technology during World War II for military applications. Thermal batteries provide a stable, robust, reliable power source capable of withstanding storage for more than 25 years without performance degradation over a wide range of temperatures. Thermal batteries are rigorously tested for safety and reliability due to their military and flight applications. They supply power to guidance missiles, ordnance device proximity fuses, nuclear weapons electronics packages, emergency backup power for hydraulic systems in aircraft, and electronics packages in extended space flights, such as Galileo [1, 2].

The electrical material properties (e.g., electrical conductivity) of thermal battery electrodes and separators influence battery performance and reliability. Because aspects of material properties depend on microstructure, and microstructure is influenced by composition and processing methods (Fig. 1.1) [3], the relationship between processing, microstructure, material properties, and performance is important. It can be studied experimentally or computationally. This thesis describes a computational approach applied to observe the process-microstructure-property relationship

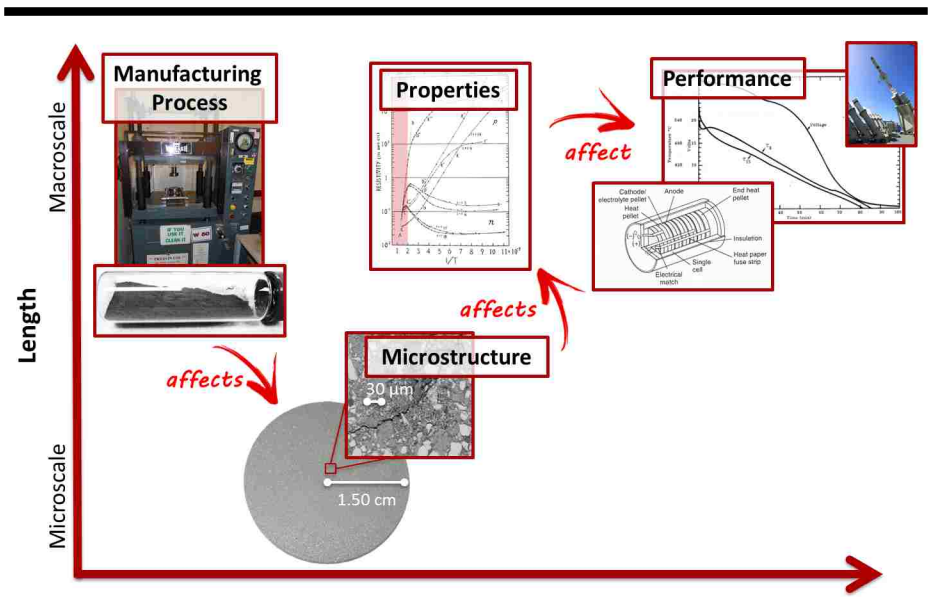

Figure 1.1: The process-microstructure-property-performance relationship.

of the effective electrical conductivity of Li/FeS_2 thermal battery cathodes, a critical property for thermal battery performance. The experimental approach for model validation is also described.

The chapter begins with a brief introduction to batteries and an overview of Li/FeS_2 thermal batteries and FeS_2 cathodes, a background on cathode composition and processing, and recent research aimed to enhance cathode properties and battery performance. Then, a physical description of electrical conductivity and experimental and computational conductivity measurement methods are provided. Next, generation of synthetic and experimental three-dimensional representative geometries for computational models is discussed. Finally, holes in current literature and a description of the thesis goal and approach are presented.

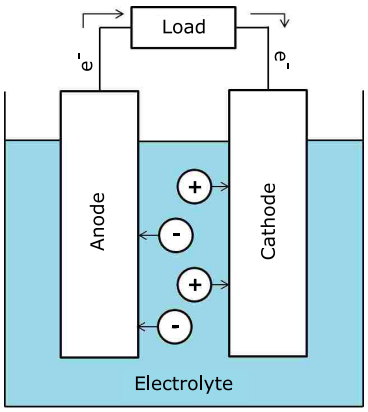

Figure 1.2: An electrochemical cell during discharge.

1.1 A Brief Introduction to Batteries

A *battery* is a device constructed of one or more electrochemical cells connected in series or in parallel. Each *cell* converts chemical energy to electrical energy with an oxidation-reduction ("redox") electrochemical reaction. Key components in a redox reaction include two electrodes, known as the anode and cathode, and the electrolyte. An electric circuit connects the electrodes for electron transfer. The *anode*, also called the negative or reducing electrode, oxidizes to donate electrons to the circuit. The *cathode*, also called the positive or oxidizing electrode, is reduced by accepting electrons from the anode. The *electrolyte* conducts ions and serves as the charge transfer medium between the anode and cathode. The electrolyte is typically in a liquid state at the battery's operating temperature [4].

During discharge, electrons flow from the anode through an external load to the cathode. The electric circuit is completed by the flow of *cations* (positively charged ions) toward the cathode, and *anions* (negatively charged ions) toward the anode [4]. Figure 1.2 illustrates discharge in an electrochemical cell.

Batteries are classified as primary or secondary. *Primary batteries* are non-rechargeable batteries, while *secondary batteries* can be recharged electrically to their

original condition [4]. Both have common commercial applications. For example, primary batteries include inexpensive, single-use AA alkaline cells that power small, portable electronic devices [5, 6]. Secondary batteries include AA nickel-zinc cells, which also power small electronics, and lithium-ion batteries that provide power to cell phones and laptops [7]. These three examples operate at room temperature. In contrast, thermal batteries, classified as primary reserve batteries, remain chemically inert until heat activation [2].

1.2 Overview of Li/FeS_2 Thermal Batteries

Thermal battery technology has been advanced with many chemistries, but Li/FeS_2, introduced in 1978 by Schneider and Bowser, is the most prominent one [8]. The electrochemistry of Li/FeS_2 batteries is well characterized, predictable, and the FeS_2 cathode material is inexpensive and accessible [1]. Like all thermal battery cells, Li/FeS_2 cells contain solid cathode, separator, anode, and heat source components (refer to Fig. 36.5 in [2]). Each battery is configured as a stack of cells. Each cell in the Li/FeS_2 battery stack includes four cylindrical, pressed powder pellets: an Fe/$KClO_4$ heat source, an FeS_2 cathode, a separator containing a molten salt LiCl/KCl eutectic electrolyte and MgO binder, and a Li-alloy anode (refer to Fig. 36.4d in [2]) [1, 2]. Pellets are prepared by uniaxially cold-pressing powder mixtures with a die and a mechanical press.

The cells remain inert until the heat source ignites, typically due to an electric igniter, a percussion primer, an inertial activator, or laser energy. The heat produced melts the eutectic electrolyte component of the separator, allowing battery discharge and current flow. Because the cathode and separator both contain electrolyte, upon thermal activation these components experience a mechanical deformation, or "slumping," due to the microstructural reordering (Fig. 1.3) [9]. In the cathode, the molten

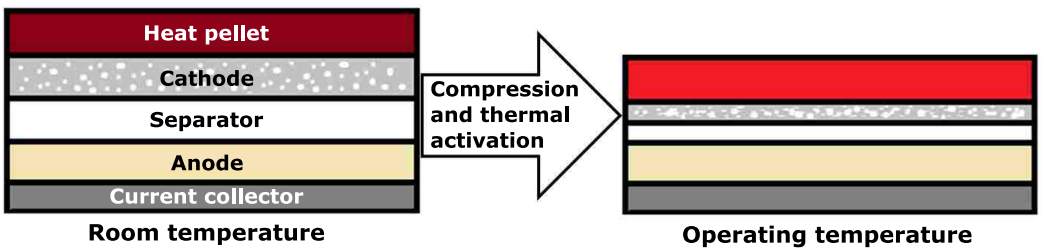

Figure 1.3: Simple diagram depicting the effects of slumping on a single cell. The change in height is purposely exaggerated.

electrolyte forms a suspension of solid FeS_2 particles and the microstructure reorganizes in response to uniaxial compression of the battery cell stack. In addition, a chemical component in the separator called a binder, typically MgO, immobilizes the non-viscous molten electrolyte during discharge. The battery stops discharging when the electrolyte resolidifies or when electrochemical reactions are exhausted [1, 2].

1.3 FeS_2 Cathodes: Properties, Composition, and Processing

The cathode, or catholyte, consists of FeS_2, LiCl/KCl eutectic electrolyte, MgO binder, and Li_2O, a lithiating agent to prevent large voltage spikes during battery activation [8]. The cathode microstructure is a bicontinuous network (Fig. 1.4). The network of solid FeS_2 particles permits electron percolation to maintain electrical conductivity. The other network consists of pore space, electrolyte, and binder, which at operating temperatures, the network permits electrolyte to flow for ionic conductivity. Electrochemical reactions occur at the FeS_2 particle surfaces.

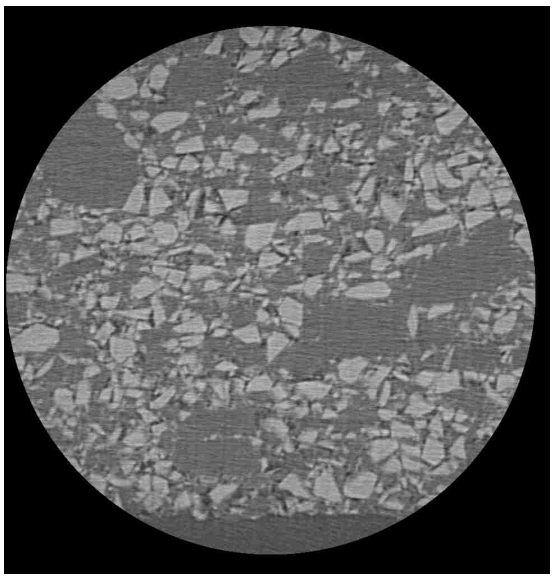

Figure 1.4: Cross-section of an FeS_2 cathode produced by microcomputed tomography. The light gray regions are FeS_2, the medium gray is electrolyte + binder, and the darkest regions are voids.

In the Li/FeS_2 electrochemical system, the polysulfide ion of FeS_2 is reduced at the cathode (Reaction 1) [8]. The cathode phases during discharge are described in Reaction 2 [1]. Battery designers typically target the first discharge reaction (Reaction 3), and sometimes the second (Reaction 4), to meet strict voltage requirements in battery design [8].

$$S_2^{2-} + 2e^- \rightarrow 2S^{2-} \quad \text{(Reaction 1)}$$

$$FeS_2 \rightarrow Li_3Fe_2S_4 \text{ (“Z-phase”)} \rightarrow Li_{2-x}Fe_{1-x}S_2(x \sim 0.2) + Fe_{1-x}S \rightarrow Li_2FeS_2 \text{ (“X-phase”)} \rightarrow Li_2S + Fe \quad \text{(Reaction 2)}$$

$$FeS_2 + \frac{3}{2}Li^+ + \frac{3}{2}e^- \rightarrow \frac{1}{2}Li_3Fe_2S_4 \quad \text{(Reaction 3)}$$

$$Li_3Fe_2S_4 + Li \rightarrow 2Li_2FeS_2 \quad \text{(Reaction 4)}$$

Electrical conductivity and semiconductor properties are key factors in battery performance [8,10]. FeS_2, or pyrite, is an ideal thermal battery cathode material. It is readily available, inexpensive [1], and a good semiconductor. As a semiconductor, the number of electrons excited into the conduction band increases with temperature [11] and so the electrical conductivity of FeS_2 is much higher at the battery's operating temperature than at room temperature. Room temperature (298K) natural FeS_2 conductivities range from 0.2 to 5623.2 $(\Omega m)^{-1}$ due to effects from minor and trace elements [12]. The dependence of electrical conductivity on temperature is favorable because FeS_2 must be electrically conductive to minimize cathode resistance [8]. Furthermore, the increase in electrical conductivity enhances the performance of Li/FeS_2 batteries in comparison to other thermal battery chemistries, such as $Ca/CaCrO_4$, due to greater battery power and lifetime [1].

Researchers strive to improve thermal battery performance by optimizing FeS_2 cathode composition and processing parameters. The FeS_2 particle size distribution has reemerged as an active area of interest after nearly three decades. In the 1990s, Guidotti studied the effects of FeS_2 particle size distributions on battery performance. He conducted 5-cell performance tests on lithiated catholyte mixes with two FeS_2 particle size distributions (<37 μm and 37-44 μm diameters). He found the FeS_2 particle size distributions that he used did not significantly affect battery activated life, but for the purpose of the study, he did not perform more extensive research on the effects of varying FeS_2 particle size distributions [13].

More recently, researchers have approached this topic by studying the differences between vastly different FeS_2 particle size distributions. Di Benedetto et al. [14] compared the performance of five-cell batteries built with cathodes of two very different FeS_2 particle size distributions. One had a nanoscale distribution (average crystallite size of 57 nm) and the other had a microscale distribution (approximately 20 μm). All pellets had the same density, thickness, and dimensions. He found the nanoscale sam-

ples had more extensive run time and higher capacity, two important performance parameters. The increase was likely due to greater surface area per unit volume, allowing a more complete electrochemical reaction before the electrolyte resolidified.

In a similar study, Au [15] used high energy ball milling to generate two size distributions. The average FeS_2 particle sizes were 1 μm and 25 nm. Cells were built with cathode pellets pressed with one of the two FeS_2 size distributions, a uniform mass, and a uniform pressing force. The results of single cell tests showed many properties improved with the nanoscale distribution: the pellets were 23% thinner, had 31% greater density, and demonstrated greater thermal stability when compared with the microscale distribution cathodes. Thermal decomposition of FeS_2 began at 500°C rather than 360°C. Smaller FeS_2 particles also improved cathode mechanical stability, which could decrease production costs by reducing material waste. Cathode pellets made with nanoscale particles contained twice the energy density of cathode pellets made with microscale particles when single cells were discharged at 1 and 0.4 A constant current until the cutoff potential of 0.8 V was reached. These results show how decreasing the FeS_2 particle size distribution could decrease the volume and mass of thermal batteries, increase energy density and specific energy, and increase the voltage or current capacity [2]. In addition to permitting a more complete electrochemical reaction than larger particles, smaller FeS_2 particles reduce internal cell resistance [16] and decrease pore space with improved particle packing because they can fit into small spaces [15].

In addition to particle size distribution and other composition variables, processing parameters affect cathode properties. As mentioned previously, cathode pellets are manufactured by uniaxially pressing powder mixtures. The press forming pressure determines the pellet density and affects the cell reactivity [2]. While this implies a relationship between density and material properties, little research on this relationship has been conducted. More than one study has been performed to observe

the effects of composition on cathode pellet forming pressure and the ability to form pellets [13, 15], however the influence of forming pressure and density on cathode properties was not indicated and requires investigation. It will be addressed in this thesis.

Composition and processing parameters can affect cathode pellet properties, and ultimately, battery performance. As discussed earlier in this section, cathode electrical conductivity is an important property with respect to battery performance, and will be the central material property studied in this thesis.

1.4 Electrical Conductivity

Electrical conductivity (σ) is a property that characterizes a material's ability to transport charge by conduction. This is in contrast to ionic conductivity, which characterizes ionic charge transfer in solution. Electrical conductivity rises with the number of free electrons. Semiconductors have a small concentration of free electrons in comparison with metals because semiconductors have stronger binding forces between atoms and their electrons [17]. The electron carrier concentration is dominated by temperature dependence [18]. As temperature increases, thermal energy excites electrons from the valence band into the conduction band, and electrical conductivity increases [17].

1.4.1 Experimental Methods of Measurement

The two most common semiconductor electrical conductivity measurement methods include the van der Pauw method [19] and electrochemical impedance spectroscopy [20]. Both methods apply a four-point electrode probe: two probes apply current and two measure the voltage difference.

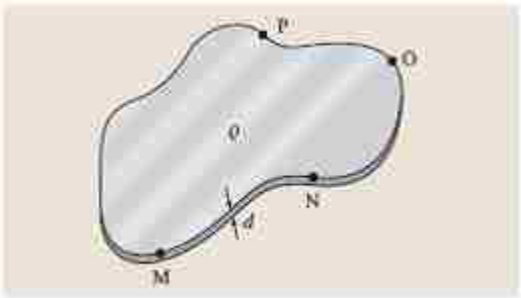

Figure 1.5: van der Pauw method applied to a material sample with arbitrary shape. M, N, O, and P refer to probe contact locations on the periphery [17].

The *van der Pauw method* can be used with material samples of arbitrary shape and thickness (d or l). Figure 1.5 shows a typical probe placement on a sample. Current (I) is applied at points M and N, and voltage (V) is measured at O and P. This leads to two resistance values, $R_{MN,OP}$ and $R_{NO,PM}$. The method also requires a geometry-dependent correction factor (c) which is specific to sample geometry and probe placement. Yamashita describes the calculation to find c for right circular cylinders, such as FeS_2 cathodes [21]. Using these variables, the electrical conductivity is calculated from the specific resistance (ρ) using the following equations [17, 19]:

$$exp(-\frac{\pi d R_{MN,OP}}{\rho}) + exp(-\frac{\pi d R_{NO,PM}}{\rho}) = 1 \tag{1.1}$$

$$\rho = \frac{V}{I} c \tag{1.2}$$

$$\sigma = \frac{1}{\rho} \tag{1.3}$$

$$\tag{1.4}$$

The van der Pauw method has four setup requirements: (1) ohmic contacts on the circumference, (2) very small contacts, (3) homogeneous sample thickness, and (4) no isolated holes in the sample [19]. For the purpose of this thesis, the experimental setup to test the conductivity of thermal battery cathode pellets requires (1) uniaxial compression and heating, (2) simultaneous measurement of the temperature and voltage drops across a sample, and (3) application of heat until the electrolyte melts to cause slumping. Because slumping would interfere with ohmic contacts on the sample circumference, electrochemical impedance spectroscopy suits these experimental needs more appropriately.

Electrochemical impedance spectroscopy (EIS) measures electrochemical behavior and electronic processes, including electron transport for electrical conductivity measurements. Applied current or voltage provides an electrical stimulus and the response is measured. The most common experiment involves the application of a single-frequency voltage or current to a sample interface while measuring the impedance, phase shift, and amplitude of the response at the given frequency. The impedance (Z) is defined as the Fourier transform of the voltage response differential equation divided by the Fourier transform of the periodic current excitation. Z is written as a complex number, $Z = a + jb$, and is plotted as a vector sum of the components a and b in Nyquist impedance plots. The system's electrical properties are obtained from a plot of the impedance over a wide frequency range followed by fitting the impedance response to a model of idealized electrical circuit elements. The circuit elements describe the system's electrochemical behavior and electronic processes [22].

Solid state material conductivity measurements involve sandwiching the material between two electronically conductive electrodes and measuring the impedance. The electrodes connect to four terminals for a four probe measurement. Four terminals are essential because they allow accurate measurement when the cable impedance is on the same order of magnitude as low impedance systems. The fit of the impedance

response to a circuit model gives the bulk resistance, R. For instance, if the material is purely resistive, the phase shift is zero and the impedance response fits a single resistor that describes the bulk resistance [22]. The relationship between the bulk resistance and measurements of the sample's geometry provide the material's conductivity using Eqns. 1.3 and 1.5 [23].

$$\rho = R\frac{A}{l} \qquad l = \text{sample thickness and } A = \text{cross-sectional area} \tag{1.5}$$

Good electrical contact between the electrodes and sample is critical to ensure the best possible electrical path to the material. The electric field lines across the sample should be parallel, such as with planar electrodes. In contrast, electrodes with point contacts would require perfect alignment for parallel electric field lines. The sample must have parallel faces and a well-defined cross section. A general purpose conductivity rig for ceramic material characterization consists of a spring-loaded harness the compresses a sample between two platinum foil electrodes. Alternatively, precious metal electrodes can be painted, vacuum evaporated, or sputtered onto the material [22].

EIS data interpretation can be challenging because ambiguities result from characterizing the system as idealized circuit elements. Idealized circuit elements may be inadequate to describe the system or multiple circuit configurations might describe the same system. Regardless, EIS is widely available, easy to use, and generates a good signal-to-noise ratio. It is a powerful technique used to study mass transport, chemical reaction rates, microstructure, defects, and the effect of composition on conductance [22].

Experimental methods are essential to measure the relationship between microstructure, bulk material properties, and materials processing. However, computational material models provide the ability to predict trends, performance, and design pa-

rameter sensitivities. Computational material models can make engineering design more efficient, less costly, and more reliable by enabling more selective experimentation [3]. Computational models can also aid in interpreting the underpinning physics of an experiment, once validated. For these reasons, a computational approach will also be used in this thesis to study the process-microstructure-property relationship for FeS_2 cathodes.

1.4.2 Computational Methods of Measurement

Bulk, effective electrical conductivity of a heterogeneous material can be estimated by direct numerical simulation at the mesoscale. A *heterogeneous material* consists of domains of multiple materials or phases, such as a composite or a polycrystal. FeS_2 cathode pellets are composite materials. The *mesoscale* here describes the intermediate length scale between the molecular level and a domain large enough to possess macroscopic, or *effective*, properties subject to the laws of classical physics [24]. Computational methods to determine effective properties are necessary because effective properties of heterogeneous materials, with constituent materials of experimentally determined bulk properties, cannot be calculated by simple mixture rules which ignore the complex interactions between phases. Microstructural features matter, even for isotropic materials. For example, phase connectedness makes a large difference in material characteristics, such as electrical percolation. However, connectedness cannot be described by mixture rules [24].

Computational methods and approaches that have been used to estimate the effective electrical conductivity of a heterogeneous material include percolation theory, effective medium approximations, and direct numerical models such as the finite element method. *Percolation theory* is a statistical physics approach of modeling the connectivity of elements (such as particles) within a random system. The *percolation threshold* is the point at which a cluster of elements spans the entire system and

long-range connectivity is first established. This approach is useful when assessing electrical percolation in conductive networks, a characteristic of a material's electrical conductivity. It has been applied to study the electrical conductivity of composite materials such as carbon nanotube composites [25,26], particulate composites [27], polymer and graphite composities [28], and metal-polymer composites [29,30]. Percolation theory approaches fall into two categories: *discrete percolation theory*, which models processes in lattices, and *continuum percolation theory*, which models processes in more realistic heterogeneous materials, such as transport in composite materials. The microstructure representations required for three-dimensional continuum percolation theory consist of a random distribution of idealized geometries (i.e., spheres, ellipsoids, disks, and cubes) within a matrix, or cell models with randomly assigned material phases. Universal characterization of microstructures by a size distribution of idealized geometries limits the applications of percolation theory [24]; furthermore, particle shape strongly influences the percolation threshold [10]. Thus, percolation theory it is not expected to model effectively conduction within microstructures with irregular geometries, like the FeS_2 particles in cathode pellets.

Effective medium approximations (EMA) employ a theoretical approach to estimate effective property trends of heterogeneous materials [24]. For example, Wang et al. applied an EMA to estimate the effective conductivity trends of lithium-ion batteries with nanostructured carbon networks, a porous, heterogeneous material [10]. EMA approaches have also been applied to study the thermal conductivity of multiwalled carbon nanotube composities [31] and the electrical conductivity of metal-insulator composites [32, 33]. EMAs apply simple microstructural information, such as volume fraction, feature shape, and feature size (whether monodispersive or polydispersive). Features are represented as spheres and ellipsoids. Effective-medium approximations include the Maxwell, self-consistent, and differential EMAs. The Maxwell and differential approximations do not estimate accurately effective conductivities of interacting features, i.e. as clusters of spheres or ellipsoids. While the self-consistent approximation can model clusters to estimate conductivity, it does not accurately estimate effective conductivity when the component phase conductivities differ significantly [24]. FeS_2 cathodes consist of clusters of highly irregular geometries and phases with electrical conductivities spanning several orders of magnitude. For these reasons and because the EMA approaches cannot predict quantitative behavior, EMAs may not effectively model conduction within FeS_2 cathodes.

The *finite element method* (FEM) is a prominent numerical modeling method that solves partial differential equations to predict physical responses of systems. FEM has been in use for at least 50 years and is widely used in engineering design to predict behavior in macroscopic systems [3]. FEM codes are available as powerful, user-friendly commercial software [34] (i.e., NASTRAN [35], ANSYS [36], MARC [37], ABAQUS [38], and ADINA [39]) for use in academia and industry. FEM imposes thermal, mechanical, and geometric constraints by applying the constitutive laws of transport phenomena to representative geometries of arbitrary shapes [3, 40]. This method simplifies a continuous system by discretization of the system to *finite elements*, or subdomains of the physical system defined and interconnected by nodes.

Meshing the features in a solid model (representative geometry) defines elements and nodes. Boundary conditions are then applied at the nodes or element faces to solve relevant balance equations and the complete system solution is obtained [34]. One limiting factor for FEM models is mesh generation on complex three-dimensional geometries, and analysis depends on a mesh with consistent quality [3]. More details concerning FEM and mesh generation will be discussed in Chapter 3.

FEM is used increasingly to model behaviors of microscale and mesoscale materials systems, both homogenous and heterogeneous. Examples of heterogeneous applications include studies of electrical conductivity of porous fiber networks [41] and carbon nanotube polymer composities [42], stiffness of nanotube polymer-reinforced composities [43], and effective elastic moduli of interpenetrating phase composites [44]. FEM and the similar finite volume method (FVM) have been applied to geometrically complex three-dimensional battery microstructures for studies of particle swelling and mechanical deformation for lithium-ion batteries [45,46]; electrochemistry and transport in lithium-ion battery electrodes [47]; tortuosity [48], area specific resistance [48, 49], and penetration depth of ionic current [49] of solid oxide fuel cell (SOFC) cathodes; and microkinetics of SOFC electrodes [50]. Application of FEM to these systems assumes the material system modeled behaves according to the constitutive relations of continuum mechanics in addition to macroscale behavior obtained from laboratory measurements [3]. For the purpose of estimating the effective electrical conductivity, a steady-state diffusion equation serves as the governing equation. Material properties are assigned to component phases of a heterogeneous material and used to solve for the effective property of the composite. While other discretization methods could be applied to solve this problem, the effective property approach and the unique attributes of FEM for complex representative geometries and diffusion problems make FEM the ideal method for estimating the electrical conductivity of FeS_2 cathodes and other porous, heterogenous materials with highly irregular geometries.

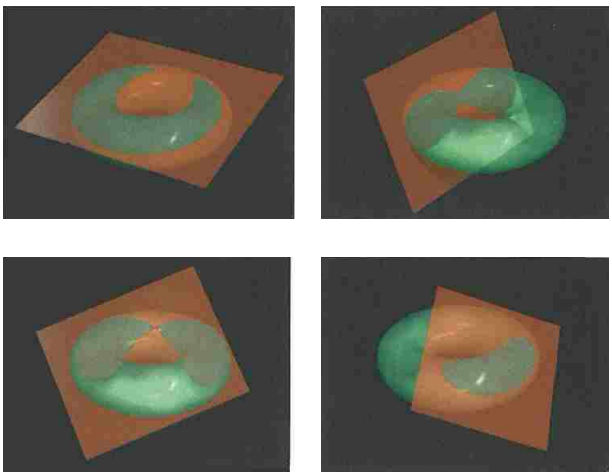

Figure 1.6: Visual demonstration of the limitations of 2D representative geometries to describe 3D structures [51].

1.5 Representative Geometry of Microstructure

Computation of material properties requires digital representative geometries, or geometric models, of material microstructure [3]. Representative geometries include two-dimensional (2D) and three-dimensional (3D) representations. Two-dimensional representative geometries provide limited structural information. As demonstrated by the planar cross-sections of a torus in Fig. 1.6, 2D representative geometries can lead to inaccurate assumptions about the 3D structure. No planar cross-section by itself reveals that the 3D structure is a torus. Three-dimensional representative geometries provide more complete information [51]. For this reason, 3D representative geometries will be used in this thesis.

1.5.1 Statistical and Synthetic Representations

Representative geometries are categorized as statistical, synthetic, and experimental [3]. Statistical methods to generate geometries include stereology and stochastic geometry, and synthetic methods involve cubic lattices of unit cells.

Stereology is the statistical examination of 1D and 2D data to develop synthetic, statistical representations of 3D structures [3, 24, 52]. This method deploys parameterized, idealized geometries (e.g. ellipsoids) using aspect ratios (length:width) and solidity (area:convex area). Characterization of the relationship between parameters provides data about the morphologies and spatial arrangements of features. Each feature is represented by voxels, the 3D version of pixels. The voxelated representation of each feature and the faces it shares with neighboring features determines the number of neighbors and connectivity [3].

Stereology has many advantages over other methods when experimental 3D data is unavailable and the 3D structures can be inferred from 2D data. Parameters such as sphere radius distribution and the mean feature width are generated statistically to nearly match experimental data. Stereological structures can be generated readily, and they are less expensive computationally than the data sets describing experimental 3D structures. For example, stereology has been successfully applied to generate 3D data from 2D cross-sections of rocks for geological applications [53]. However, stereology has many limitations. It cannot relate a feature's curvature with its size, shape, and the curvature of neighboring features. Stereology cannot characterize both neighboring features and next-nearest neighboring features. Statistical descriptors are far from complete and may not be adequate to represent highly irregular microstructures [3].

The *stochastic geometry* approach deploys statistical descriptors to characterize random patterns and generate representative geometries. Canonical n-point correla-

tion functions statistically describe microstructural details (e.g., phase volume fraction, interface surface area, shapes, sizes, spatial distribution, and connectivity). n increases with the amount of information embodied in the correlation function. For example, 1-point correlation functions are the simplest and provide the least information, while 2-point to n-point correlation functions describe the spatial arrangement of microstructural features, the arrangement of grains with particular microstructural parameters, and neighboring features. Like stereology, stochastic geometry employs idealized 3D microstructures [3, 24].

Unit cell representative geometries apply a unit cell as the smallest unit in a periodic microstructure with one or two phases. These geometries have been commonly applied to model battery microstructures [54–56], which is just one of many applications. The unit cell model lowers computational cost because its response is assumed equivalent to the macroscopic response of a periodic array of unit cells. This assumption limits the method's ability to calculate effective properties using constitutive equations. If the actual microstructure is not periodic and instead is irregular, the unit cell fails to reflect the system. For example, this method assumes a mechanical instability in a unit cell to be uniform throughout all unit cells in the macroscopic model [3].

Statistical and synthetic representative geometries may be inadequate for the 3D representation of highly irregular microstructures, such as FeS_2 cathodes. Irregular geometries are not well represented by idealized shapes, such as spheres and cylinders. Furthermore, representations generated by the methods described previously lack information about the true shape and size of 3D features and the relationship between neighboring features. Statistical and synthetic representations of microstructural features gathered from 2D characterization data are estimates and provide only reasonably accurate approximations. Representative geometries based on 3D data would more accurately represent the relationship between microstructure and ma-

terial properties. Fortunately, sophisticated laboratory and computational methods continue to emerge to enable engineers and scientists to develop real, or *experimental*, 3D representative geometries from 3D characterization data [3, 51].

1.5.2 Experimental Representations

Experimental representative geometries provide geometric and topological information which other geometries cannot depict. The true size, shape, and distribution of specific individual features and surroundings are observable [3]. The phase volume fractions, interfacial surface area, number of features in a volume, and connectivity between networks can be quantified. The primary challenges with these models include the significant amount of time and effort required to collect 3D data; cost, availability, and experimental complexity; and the amount of memory required to transmit and process 3D arrays of data [3, 51]. These issues are relevant, but automated instrumentation, software development, greater computational power, and other technological advancements are overcoming these challenges [3].

Two primary methods of 3D material characterization include serial sectioning and X-ray tomography. The optimal technique for a given material depends on the length scale and the type of material [3]. *Serial sectioning* is the most common method of 3D material characterization because it is widely available and has existed for almost nine decades. Serial sectioning involves 2D characterization of a planar surface followed by layer removal. These steps are repeated until the volume of interest is obtained. Then, computational reconstruction generates a 3D geometry from the 2D data. Important parameters of serial sectioning experiments include accurate determination of the section thickness removed during each step and generation of parallel surfaces during "slice" removal. The experimentalist must consider the precision of the sectioning technique, account for variability between sections, consider the spatial resolution and capabilities of the 2D characterization method, and determine a minimum target

resolution. Serial sectioning is destructive and requires substantial time for sectioning and computation, especially for manual serial sectioning [3].

Serial sectioning can be performed manually or with an automated system. Automated systems provide better control over section thickness as well as the ability to adjust imaging settings to maintain intensity and sharpness throughout the experiment. Systems that perform automated serial sectioning include the Alkemper and Voorhees micromiller [57, 58], the Genus-3D [59], the Robo-Met.3D, and focused ion beam scanning electron microscopy (FIB-SEM) [3]. Among these, the systems available for the author's use included the Robo-Met.3D and FIB-SEM.

The *Robo-Met.3D* [60] uses a precision mechanical polishing system with an optical microscope. The system uses section-to-section control of slice thickness by maintaining grinding and polishing parameters and has demonstrated less than micron-level section thickness. It can complete up to 20 sections per hour depending on other variables such as resolution, quantity, and number of images taken. The Robo-Met.3D can be used with a wide variety of materials, but the samples must be characterizable with an optical microscope and a single polishing step must be adequate for material removal and polishing [3]. This method has characterized metal samples such as titanium alloys [61] and single-crystal nickel alloys [60, 62].

FIB-SEM [63] is the most commonly used method to obtain 3D microstructural data because it is common in many labs throughout the world. It focuses highly energetic ions to remove thin layers of material with a closed-loop system. Ideal for grains and structures less than or equal to 10 μm, it can generate data with nanometer resolution and it provides one to two orders of magnitude better resolution and section control thickness than other serial sectioning methods [3, 64]. FIB-SEM can easily incorporate instrumentation for structural, chemical, and crystallographic information, such as energy dispersive X-ray spectroscopy (EDS) for chemical mapping. FIB-SEM requires multiple days to collect data for submillimeter volumes [3] and users must

fine-tune the imaging parameters to get high quality 2D data [64]. It can be used for fragile or porous materials, such as porous SOFC electrodes [48, 64–74] and polymer electrolyte fuel cell cathodes [75]. Lithium-ion battery cathodes have also been characterized with FIB-SEM [47, 76].

Although serial sectioning instrumentation is common and widely available, the associated methods have many disadvantages. Serial sectioning (with the exception of FIB-SEM) often provides poor depth resolution. Alignment and accurate determination of the depth dimension can be challenging to correct. Cubic voxels are distorted and elongated. For surface imaging, the removed material must be inferred or interpolated from the planes above and below the material; if the planes are too far apart, this can cause serious misinterpretation of the final 3D structure [51]. Post-processing of the data also causes misinterpretation. For instance, Gunda et al. observed significant effects upon internal surface area and porosity, which later affected computation of transport properties [64]. In addition, compression from mechanical sectioning may cause material distortion. These challenges affect image presentation, processing, and structural measurements. As a result, the data is not genuinely 3D, but X-ray tomography overcomes many of these challenges [51].

X-ray tomography [77] mathematically reconstructs X-ray transmission (absorption) images at various projections to create 3D data. This method is nondestructive and can provide a range of resolution from 10 μm to the nanoscale [3, 51, 64, 78]. It is sensitive to changes in atomic number and density and it characterizes porosity effectively [3]. Tomographic reconstruction provides true 3D images [51]. It is also capable of measuring time-dependent parameters (4D data). Until recently, this method required high-intensity X-rays, such as from a synchrotron source, to reach an acceptable signal-to-noise ratio and resolution for investigation of microstructure [3]. Newer methods such as nano X-ray computed tomography (nano-XCT) can provide resolution on the nanometer scale and microcomputed tomography (MicroCT) pro-

vides micron-scale resolution [78–80]. Samples must be on the order of millimeters or even smaller to generate high resolution nano-XCT data [64]. In contrast, one method of MicroCT, Xradia X-ray microscopy combined with the resolution of interest (ROI) function, is not limited by the small sample size requirement and can achieve resolution equal to or less than one micron [81]. Eastwood et al. applied this method for efficient and effective characterization of a lithium-battery microstructure during discharge [78]. Others have applied X-ray microscopy to characterize microstructures of fuel cells [79, 80], limestone [82], nickel-based superalloys [83], gas-atomized and plasma-atomized powders [84], and biological samples, such as muscle tissue [85]. As described, X-ray tomography techniques have many advantages over serial sectioning methods and are preferable when materials are compatible with X-rays and the resolution is appropriate for the material of interest.

Each of the previously described methods has its advantages and disadvantages. An optimal outcome of a material's 3D microstructure reconstruction requires knowledge of the material of interest, its compatibility with a given method, and the imaging requirements to achieve an appropriate resolution and field of view for the representative geometry. FeS_2 cathodes are fragile, porous, heterogeneous materials with a wide distribution of feature sizes (1 - 50 μm). For these reasons, the MicroCT method within X-ray tomography is the most appropriate method for development of an experimental representative geometry in this situation.

1.6 Thesis Purpose and Approach

The goal of this thesis is to develop a greater understanding of how composition and processing conditions modify the microstructure and affect the electrical conductivity of Li/FeS_2 thermal battery cathodes, thus exploring the process-microstructure-property-performance relationship for thermal batteries. A greater understanding of this relationship is important because the electrical conductivity of the cathode is a critical property in battery performance. As the battery is activated, the conductivity must increase to minimize the resistance and maximize performance. While the temperature-dependent properties of the FeS_2 semiconducting material plays a large role in this, I propose that another important factor is the microstructural rearrangement which occurs with slumping shortly after thermal activation. I hypothesize that the electrical conductivity will increase after slumping because the FeS_2 particles will move into closer contact with each other, improving the percolation of electrons through a conductive network. Furthermore, I expect that changing the processing and composition parameters will affect the conductivity before and after slumping because manufacturing conditions influence microstructure.

To the best of the author's knowledge, the process-microstructure-property-performance relationship for electrical conduction within thermal battery cathode materials has never been studied, especially in a systematic manner. This relationship is important and could unlock information for optimal thermal battery design and optimized performance parameters. Currently, many factors of thermal battery design relies on legacy empirical methods that lack a more fundamental foundation. This thesis is a starting point for a systematic study of the effects of processing and composition upon thermal battery cathode microstructure and electrical properties.

The approach chosen for this work is both experimental and computational. The two methods provide for comparison between observations from the experimental,

real-world measurements, and a more fundamental perspective of the physics from computational simulations. In order to isolate the effect of the microstructural reorganization due to slumping on the electrical conductivity, all cathode measurements and simulations will occur at steady-state with solid-state electrolyte (not molten). Experimental electrical conductivity measurements will apply impedance spectroscopy and the effective electrical conductivity will be determined numerically by solving electrostatics differential equations on a measured geometry using the finite element method. Because the FeS_2 particles in this porous, heterogeneous material are highly irregular and consist of a wide particle size distribution, the FEM simulations will be applied to experimental, 3D representative geometries from MicroCT characterizations.

Chapter 2

Experimental Methods

The chapter begins the experimental design, powder and pellet preparation, sample assembly for electrical conductivity tests, and a description of the electrical conductivity tests performed with impedance spectroscopy. The chapter also describes how the cathode pellets' microstructures were characterized in three dimensions and reconstructed to provide experimental representative geometries for finite element modeling.

2.1 Design of Experiments

Three Li/FeS_2 cathode pellet composition and processing parameters were selected for this study: (1) FeS_2 particle size distribution, (2) FeS_2:EB (electrolyte and binder) composition ratio, and (3) pellet density. To limit the scope of this thesis, three values (represented as A, B, and C) for each parameter were selected. Minitab [86] was applied to determine a Design of Experiments (DOE) with nine three-variable combinations and a randomized experimental run order. An ideal experimental design would have required 81 combinations with at least three replicates per combination, however material availability and time constraints limited the DOE to nine combi-

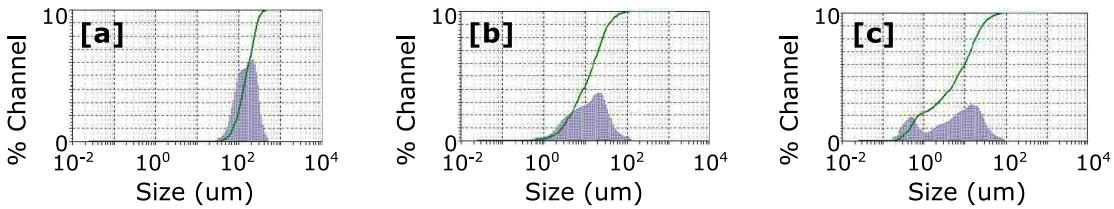

Figure 2.1: Particle size distributions (volume distributions) of raw and size-reduced FeS_2 powder.
[a] Raw powder without sonication.
[b] Reduced size powder (prior to seiving) without sonication.
[c] Reduced size powder (prior to seiving) with one minute of sonication.

Table 2.1: Statistics from particle size analysis of raw and reduced size powders.

Powder ID	Mean Diameter of the Volume Distribution (μm)	10% Volume < Size (μm)	50% Volume < Size (μm)	90% Volume < Size (μm)
Raw, no sonication	167.9	74.3	153.6	281.5
Reduced, no sonication	16.87	2.675	12.11	35.87
Reduced, 1 min sonication	10.72	0.435	6.61	26.04

nations with a minimum of three replicates each. The DOE statistics for nine pellet types in triplicate and the randomized experimental run order are reported in Table B.1 of the Appendix.

2.2 FeS_2 Powder and Cathode Pellet Preparation

Raw FeS_2 powder from a natural source was purchased from a vendor and sent to Union Process, Inc. (Akron, OH), for particle size reduction with a batch dry grind process. The target particle size distributions were 200, 150, 100, 50, and 1-5 μm. The

Table 2.2: ASTM E11 sieves, in the stack order used for sieving powder. Mesh opening sizes provided by Gilson Company, Inc. [87].

ASTM E 11 Sieve No.	Mesh Opening Size (μm)
170	90
200	75
230	63
270	53
325	45
400	38
450	32

grind process rate and grind time were varied and fractions were removed sequentially to determine achievable distributions. According to a report from Union Process, the initial (raw) FeS_2 powder rapidly reduced in size, surpassing the 100 and 200 μm target sizes. The material also appeared to agglomerate without sonication. Small samples from each fraction underwent particle size analysis before and after particle size reduction (Fig. 2.1, Table 2.1) at Union Process using a Microtrac Inc. S3000/S3500 laser diffraction particle size analyzer (Microtrac, Montgomeryville, PA) in water.

The fraction selected for this thesis was ground with 275 RPM for 10 minutes, selected for the amount of material available and the width of the particle size distribution. This distribution was wide enough to be sieved by ASTM E11 sieves with mesh opening sizes between 30 and 100 μm, selected by considering the particle size distribution and distributions successfully used with our pellet manufacturing process.

After particle size reduction, particles were separated by size when sieved for 35 minutes with a stack of ASTM E11 sieves (Gilson Company, Inc., Lewis Center, OH), assembled in the order shown in Table 2.2, and a W.S. Tyler RO-TAP Sieve Shaker

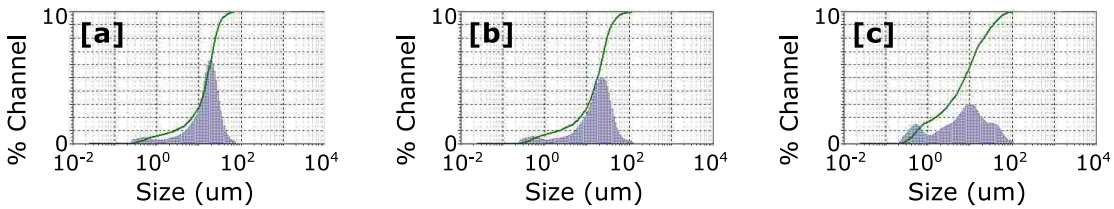

Figure 2.2: Particle size distributions (volume distributions) of sieved FeS_2 powder.
[a] Particle size distribution "A" with one minute of sonication.
[b] Particle size distribution "B" with one minute of sonication.
[c] Particle size distribution "C" with one minute of sonication.

(W.S. Tyler, Mentor, OH). The sieves pass particles with diameters smaller than the openings of each mesh hole and retained particles with diameters larger than the openings. For example, -400/+450 sieves isolate particles with diameters between 32 and 38 μm. The sieved powder fractions were separated and baked in a vacuum oven (Binder, Tuttlingen, Germany) at 103^{o}C for 16 hours plus several hours for the oven to cool after venting. Baking the powders removed moisture from exposure to ambient air while handled by Union Process. After receipt from Union Process, all powder was handled and stored in a dry laboratory maintained at low humidity (maximum 750 ppm water, or -23^{o}C frost point).

Following particle size reduction, sieving, and bake-out, three powder fractions were selected because they provided sufficient material mass to press at least six pellets of each type, necessary in case of defective pellets. Small samples from each of the selected powder fractions underwent particle size analysis with sonication in water at Union Process (Fig. 2.2, Table 2.3). The resultant distributions did not match the expected values from the sieve opening sizes. The particles may have been agglomerated prior to and during sieving, preventing smaller particles from reaching the finer sieves, and then sonication in water broke up agglomerations during particle size analysis. The measured size distributions were polydisperse rather than monodisperse, and the amount of agglomeration during pellet pressing is unknown.

Table 2.3: Statistics from particle size analysis of sieved powders.

Powder ID	Target Size Distribution (μm)	Mean Diameter of the Volume Distribution (μm)	10% Volume < Size (μm)	50% Volume < Size (μm)	90% Volume < Size (μm)
PSD A, 1 min sonication	32-38	16.64	2.7	15.77	30.13
PSD B, 1 min sonication	38-45	20.16	2.127	17.65	38.64
PSD C, 1 min sonication	45-53	13.08	0.545	7.60	35.17

Particle size analyses without sonication were not performed on the sieved powders, but would have been useful to determine the effect of sonication on agglomerated particles. These factors, the target size distributions, and the sonicated and measured distributions, will be considered in the analyses in Chapter 4 because the sieving method is commonly used to target particle size distributions in thermal battery pellet manufacturing.

The FeS_2 powders were combined in a Turbula®T2F (Willy A. Bachofen AG Maschinenfabrik, Muttenz, Switzerland) mixer with electrolyte and binder (EB) and lithiating agent powders to create three FeS_2:EB composition ratios (2.3, 2.9, 3.9). The powders included Li_2O lithiating agent (Sigma-Aldrich, St. Louis, MO), 45/55 wt % LiCl/KCl eutectic electrolyte, and MgO binder (Merck, no longer in business). Each combined powder was *fused*, or blended and heated, and then manually broken up and sieved through a No. 60 sieve with 250 μm opening size [87].

The fused powders were cold-pressed into pellets with a Wabash 50 ton hydraulic press (Wabash MPI, Wabash, IN). The powder mass was calculated from the target pellet density and thickness, and measured with a Mettler AE 240 balance

Table 2.4: Mean density, mean diameter of the volume distribution, and composition ratios of pellets selected for testing and analysis. Three pellets were selected for each pellet type. Reported density mean and standard deviation were calculated from these triplicate samples.

Pellet Type	AAA	BAC	CAB	ABB	BBA	CBC	ACC	BCB	CCA
Numerical Pellet Type	1	2	3	4	5	6	7	8	9
Target Size Distribution (μm)	32-38			38-45			45-53		
Target Density (g/cm^3)	2.76	2.91	3.06	2.76	2.91	3.06	2.76	2.91	3.06
Mean of Achieved Density (g/cm^3)	2.62	2.83	2.99	2.70	2.88	3.08	2.71	2.91	2.96
Standard Deviation of Achieved Density (g/cm^3)	0.03	0.06	0.02	0.05	0.03	0.04	0.06	0.01	0.03
Mean Diameter of the Volume Distribution (μm)	16.64			20.16			13.08		
FeS_2:EB Ratio	2.3	3.9	2.9	2.9	2.3	3.9	3.9	2.9	2.3

(Mettler-Toledo, LLC, Columbus, OH). Then, the powder was poured into a cylindrical, 1.2416" diameter manufacturing die, followed by uniaxial press activation at a specified tonnage, "stripping" the pellet under reduced pressure to ease it out of the die without breakage, and finally the pellet was released from the die. The tonnage setting was determined by a trial-and-error process until the target density was achieved, the press reached its maximum tonnage, or the powder was depleted, all which limited achievable densities. Table 2.4 summarizes the achieved pellet densi-

ties, mean diameter of the FeS_2 volume distributions, and FeS_2 composition ratios for pellets selected for electrical conductivity tests. Because the achieved densities deviated from the target values, the achieved densities will be used in all future analyses, rather than the target densities.

2.3 Sample Assembly Preparation

Impedance spectroscopy was applied for electrical conductivity tests. As discussed in Chapter 1, these tests require conductive electrodes on each side of the sample with two current and two voltage connections for a four-point measurement. The sample assembly design met these requirements.

Stainless steel electrodes were die-cut with a Multicage pneumatic press (Multicycl Inc., Bolton, Ontario, Canada) into lollipop-shaped pieces from 4 mil sheets of 304 stainless steel (Fig. 2.3A) and cleaned with reagent grade methanol prior to assembly. Two stainless steel pieces were resistance welded with a Miyachi Unitek (Amada Miyachi, Monrovia, CA) resistance welder to make each electrode. An Omega type K thermocouple (Omega Engineering, Inc., Stamford, CT) was placed between the two steel pieces of each electrode and resistance welded in place (Fig. 2.3B). Then, the thermocouple accuracy was tested and verified with an Omega Benchtop temperature controller (Omega Engineering, Inc., Stamford, CT).

Prior to insertion within the sample assembly, the thickness of each pellet was measured with a Starrett ST1147079 No. 3732 micrometer (The L.S. Starrett Company, Athol, MA) and the mass was measured with the Mettler balance. Thickness and mass measurements occurred in the run order specified by the DOE. Then, individual pellets were sandwiched between two electrodes and two pieces of mica (MicaFactory.com, location unknown) (Fig. 2.3C and D) to form a sample assembly. Staples

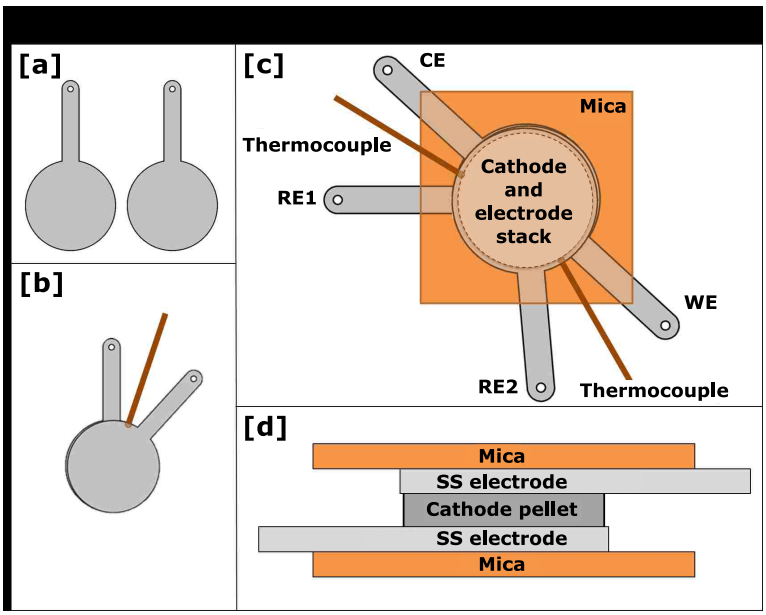

Figure 2.3: Sample assembly for electrical conductivity tests.
[a] Two lollipop-shaped pieces of stainless steel combined to form one electrode.
[b] A thermocouple welded between the two pieces of each electrode.
[c] A top-down view of the sample assembly. Connection locations between sample electrodes and the potentiostat are shown. The counter electrode (CE) and reference electrode 1 (RE1) were connected to the bottom steel electrode. The working electrode (WE) and reference electrode 2 (RE2) were connected to the top steel electrode.
[d] A side view of the sample assembly. Thermocouples are not shown.

located near the edges held the sample assembly together and the thermocouples in place.

Sample exposure to ambient moisture was minimized. Samples were prepared in a dry room and packaged in sealed plastic bags with dry room air for transportation to a VAC Omni-Lab 102282 glovebox (Vacuum Atmospheres, Hawthorne, CA) for testing. The glove box provided a controlled, dry Argon atmosphere with less than 1 ppm moisture, and rubber gloves on one side for user access (Fig. 2.4). Transportation required less than two minutes and the samples were immediately placed in the glove box antechamber and pumped down for glove box entry.

Figure 2.4: Argon glove box used for testing.

2.4 Electrical Conductivity Measurements

Electrical conductivity measurements were conducted using impedance spectroscopy, as discussed in Section 1.4.1. The instrumentation included a potentiostat, or a Solartron SI 1287 Electrochemical Interface (AMETEK, Inc., Berwyn, PA), and a Schlumberger SE 1255 Frequency Response Analyzer (AMETEK, Inc., Berwyn, PA). All measurements were made within an argon-filled glove box, which served as a Faraday cage to minimize interference. Cables between the glove box and instrumentation were shielded and unshielded cables within the glove box were twisted together tightly and made taut to minimize inductance. Calibration was performed and verified daily prior to testing with a Solartron 12861 ECI Test Module (AMETEK, Inc., Berwyn, PA).

The experimental setup included heat application on the top and bottom of the sample assembly, uniaxial compression, and electrical connections between the electrodes and potentiostat (Fig. 2.5-2.6). Two heater blocks containing cartridge heaters were controlled and monitored with a Honeywell temperature controller (Honeywell, Morristown, NJ) and lifted apart with a lever for sample insertion. The sample stage pivoted to prevent the sample from heating prior to or after testing. A small, flat

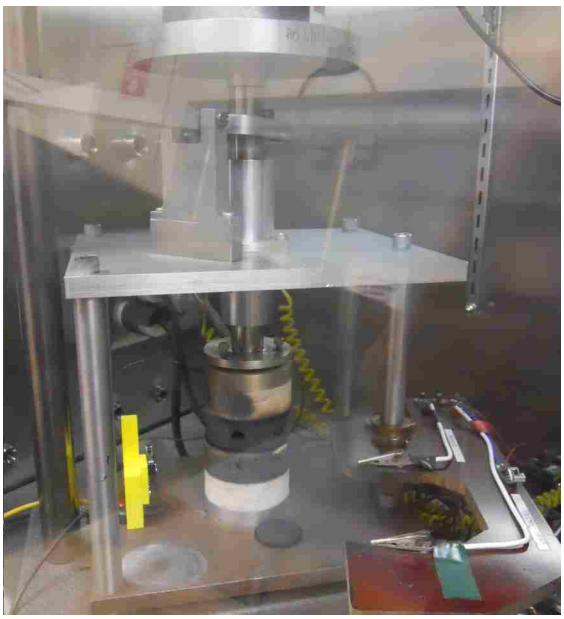

Figure 2.5: Experimental setup for electrical conductivity measurements.

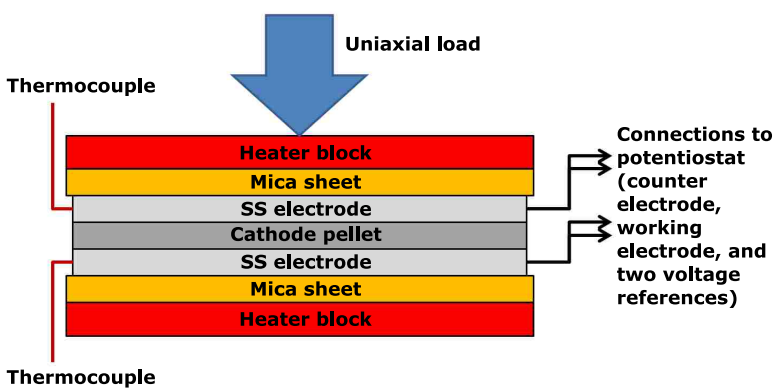

Figure 2.6: Diagram of experimental setup for electrical conductivity measurements.

metal disk with a diameter slightly larger than the pellet diameter was positioned between the top mica sheet and the top heater block to improve thermal contact with samples.

The setup included a weight stage above the top heater for additional sample compression. The upper portion of the experimental setup had a mass of 1659.3 g

and the weights on the weight stage totaled 398.6 g, for a sum of 2057.9 g, or 4.5369 lb_m, compressing each 1.2416" pellet with a total of 120.56 lb_f/in^2 (psi). Two hook clips, two alligator clips, and four wires connected samples to the glove box electrical output ports, which were connected to the potentiostat outside of the glove box with shielded cabling. Connections between the sample electrodes and the potentiostat are shown in Fig. 2.3c. Electrode thermocouples were connected to Omega Benchtop Controllers within the glove box for temperature measurements of the sample during heating and compression.

Cathode sample impedance was measured in the order specified by the DOE with the heater blocks set to either 25^{o}C, 100^{o}C, or 200^{o}C. Heater blocks were given at least 30 minutes to stabilize prior to measurement and the temperature was monitored to verify that stabilization was reached. Samples were heated under compression for ten minutes prior to measurement to reach thermal equilibrium. Time was measured with a traceable digital timer (Fisher Scientific, Pittsburgh, PA). The sample electrode temperatures were recorded at the time of impedance measurements. The impedance experiment type was DC potential vs. reference. Settings included 1-10^4 Hz sweep frequency and 10 mV AC amplitude, with the low pass filter, bias rejection, and auto attenuator settings all activated. Impedance measurements were taken on solidified pellets before and after slumping. Slumping was induced by compressing and heating samples at 500^{o}C for two minutes. No impedance measurements occurred during slumping, when the electrolyte was molten, for experimental ease. The goal was to measure only the electrical conductivity, rather than both ionic and electrical conductivities.

Following impedance measurements, impedance data were fit to equivalent circuits using ZPlot software [88]. Every sample exhibited a phase shift near zero and imaginary impedance component (Z") approaching zero (Fig. 2.7). Because this is indicative of purely resistive behavior, each spectrum was fit to a single resistor circuit

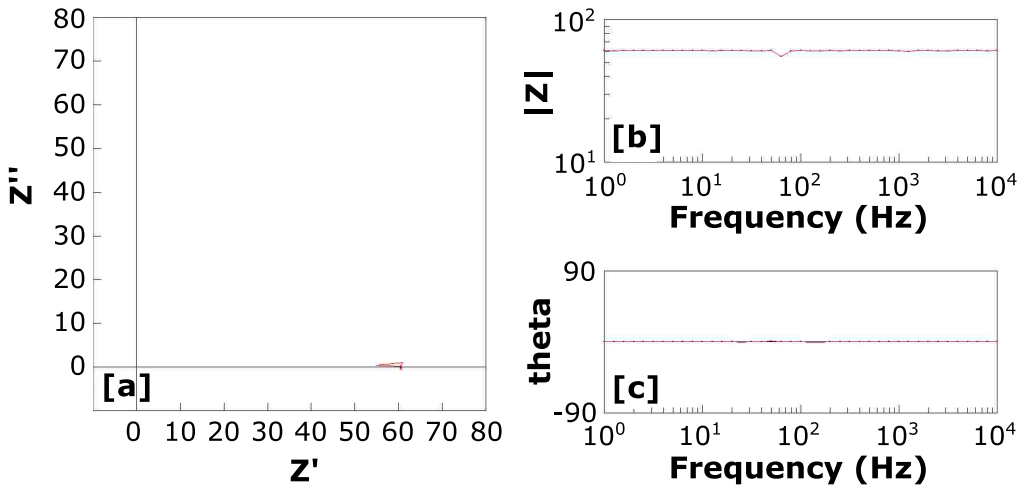

Figure 2.7: Impedance spectra for one slumped sample at 100°C. The trends shown here were typical of all samples.
[a] Nyquist plot showing the real component of impedance (Z') vs. the imaginary component of impedance (Z").
[b,c] Bode plot. [b] Plot of freqency vs. impedance magnitude (|Z|).
[c] Plot of frequency vs. phase shift (theta). The phase shift approached zero with a jump near 60 Hz due to interference from lab lighting.

(R_{fit}) in ZPlot with very little error. The postslump pellet thicknesses (l) were measured after cooling in the DOE run order, using the same micrometer as before. Then, the electrical conductivity (σ) was calculated for each measurement by applying R_{fit}, l, and the cross-sectional area (A) to Eqn. 2.1.

$$\sigma = \frac{l}{R_{fit}A} \tag{2.1}$$

Table 2.5: Comparison of methods for 3D characterization.

Methods	Advantages	Disadvantages
Focused Ion Beam (FIB) + Scanning Electron Microscopy (SEM)	Energy Dispersive Spectroscopy (EDS) for chemical analysis, no/controllable water contamination, automated, well-controlled slice thickness	Insufficient FOV and sample volume
Microtome + SEM	Appropriate FOV and pixel size, EDS for chemical analysis, no/controllable water contamination, well-controlled slice thickness	Issues due to pellet fragility, less controlled sample orientation, time consuming, expensive
Manual serial sectioning + SEM	Appropriate FOV and pixel size, EDS for chemical analysis, no/controllable water contamination	Time to master technique, pullout and pellet fragility, less controlled sample orientation and slice thickness, time consuming, expensive
Manual serial sectioning + optical microscope	Appropriate FOV, no/controllable water contamination, ability to identify FeS_2 less expensive	Time to master technique, pullout and pellet fragility, less controlled sample orientation and slice thickness, time consuming
Robo-Met.3D (robotic serial sectioning) with silicone resin vacuum impregnation	Appropriate FOV, ability to identify FeS_2, well controlled orientation and slice thickness, mostly automated	Water contamination, issues due to pellet fragility, time consuming, expensive
ZEISS Xradia 520 Versa 3D X-ray microscope (microcomputed tomography)	Appropriate FOV, no/controllable water contamination, ability to identify FeS_2, automated, nondestructive, fast	Availability, possibly cost of equipment

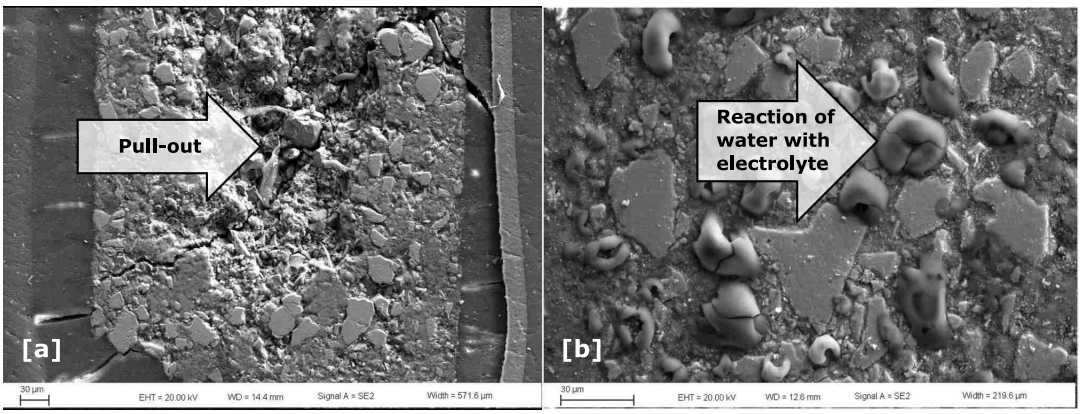

Figure 2.8: Challenges associated with preparation for SEM.
[a] Secondary SEM image of an FeS_2 cathode pellet cross-section showing significant pull-out of FeS_2 particles.
[b] Secondary SEM image of water contamination due to reaction between electrolyte and ambient moisture.

2.5 Microstructure Characterization

2.5.1 Method Selection

Selection of a 3D microstructure characterization method required consideration of many parameters in order to achieve a quality representative geometry. Assuming that the electrolyte, binder, lithiating agent, and pore space is homogeneously distributed between FeS_2 particles, the characterization method selection focused on the size and distribution of FeS_2 particles. The target field of view (FOV) was ten times the diameter of the largest features (the largest FeS_2 particles) and the target pixel size was one-tenth of the diameter of the smallest features (the smallest FeS_2 particles). These measurements were estimated using the particle size distributions provided in Section 2.2. The ideal FOV was more accurately determined in a study of the representative volume element (RVE) in Section 3.5.2. Next, FeS_2 particles had to be easily identifiable with the characterization method selected to permit the thresholding and segmentation steps for representative geometry reconstruction.

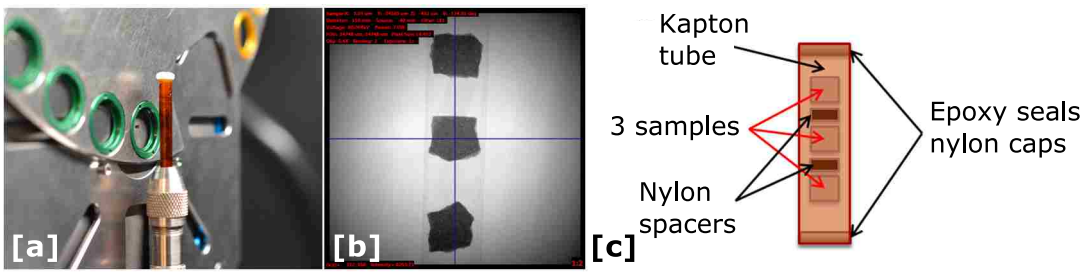

Figure 2.9: Setup for MicroCT.
[a] A Kapton tube containing three samples is shown in the X-ray microscope. The tube was placed on its axis of rotation as close as possible to the source while preventing collision of the tube with the instrumentation.
[b] An X-ray projection demonstrates coordinate selection in preparation for automated characterization of three samples in one Kapton tube.
[c] A simple diagram depicts sample alignment within a Kapton tube.

Then, susceptibility of the electrolyte to water contamination, even from ambient moisture, and cathode fragility were considered due to common issues in preparation for scanning electron microscopy (SEM) characterization (Fig. 2.8). Available time and funding were also considered. All investigated methods with their associated advantages and disadvantages are presented in Table 2.5.

2.5.2 Microcomputed Tomography

A ZEISS Xradia 520 Versa 3D X-ray microscope (Carl Zeiss Microscopy GmbH, Jena, Germany) was selected for 3D characterization [81]. Samples were prepared for MicroCT (see Section 1.5.2) in a dry lab by cutting 3 mm x 3 mm squares from the center of each selected pellet. Three pellet fractions were rolled in a 2 mil plastic sheet, each fraction separated by a piece of nylon plastic, and the roll was placed in a 4 mm diameter Kapton (polyimide) tube (Fig. 2.9a-c), selected for Kapton's low permeability to water vapor and high X-ray transmittance. Small cylinders of nylon and one-minute epoxy sealed the tube ends to prevent contamination from ambient moisture.

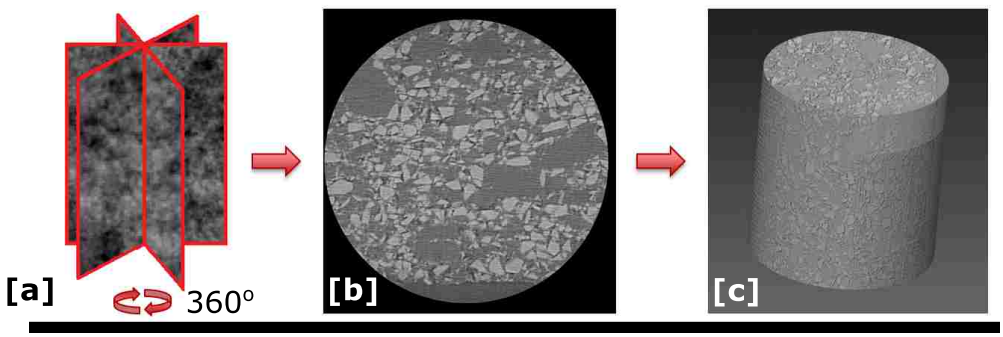

Figure 2.10: Progression from X-ray projections to a reconstructed volume.
[a] Each plane depicts one raw projection per angle. Only three projection planes are shown for simplicity, but 4,001 projections over 360^o generate a cylindrical volume characterized by MicroCT.
[b] A single TIFF image from the reconstructed projections. The circular shape is a cross-section perpendicular to the sample's axis of rotation.
[c] A volume constructed from nearly 1,000 TIFF files.

Eighteen characterizations (nine pellet types, before and after slumping) were completed using the automation settings on the X-ray microscope with a 80 kV, 82-88 μA source. Prior to each series of automated acquisitions, coordinates were selected within each sample to ensure proper centering. During acquisition, 4,001 X-ray projections around a single rotation axis characterized the selected sample volume (Fig. 2.10). After acquisition, each series of raw projections was reconstructed and exported as a stack of nearly 1,000 TIFF files with 0.5 μm pixel size after determination of the optimal center shift (between 27.8-36.2, depending on the sample) and beam hardening constant (0.06) for the sample, all using Xradia software.

2.5.3 Geometry Reconstruction

Avizo software [89] was applied to reconstruct each stack of TIFFs into a three-dimensional cylindrical geometry (Fig. 2.10b-c, 2.11a). The geometry was cropped to the largest rectangular prism that could fit into the cylindrical volume (Fig. 2.11b). The planar surfaces of the rectangular prism allowed for easy identification of sur-

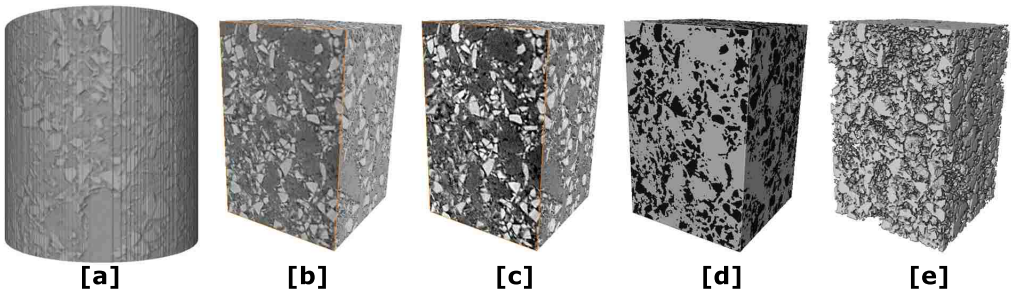

Figure 2.11: Workflow from the TIFF reconstruction to the FeS_2 representative geometry, prior to meshing.
[a] Cylindrical volume reconstructed from TIFFs.
[b] Cropped volume.
[c] Contrast enhancement.
[d] Segmentation and thresholding using the Watershed algorithm. FeS_2 particles appear black.
[e] Isolation of FeS_2 particles by subtraction of the EBLP phase.

faces along the x, y, and z axes. Then, contrast enhancement (contrast setting = 2) (Fig. 2.11c) improved the ability to differentiate FeS_2 particles from surrounding material by enhancing the intensity distributions and decreasing oversegmentation in the next step, thresholding and segmentation. Avizo's Watershed algorithm achieved thresholding and segmentation of the microstructure into two phases: (1) the FeS_2 phase and (2) the electrolyte, binder, lithiating agent, and pore (EBLP) phase (Fig. 2.11d), and islands, or isolated pixels within regions of the opposite phase, were removed. The Watershed algorithm settings, specifically the gradient threshold and phase ranges, were selected with a trial-and-error process for each reconstruction in order to achieve $\leq 5\%$ relative error of the reconstructed FeS_2 phase volume fraction, calculated with respect to each pellet's experimental FeS_2 volume fraction. The volume fraction was sensitive to image processing settings. Last, subtraction of the EBLP phase from the binary volume then isolated the FeS_2 particle phase to form a representative geometry for the computational simulations (Fig. 2.11e).

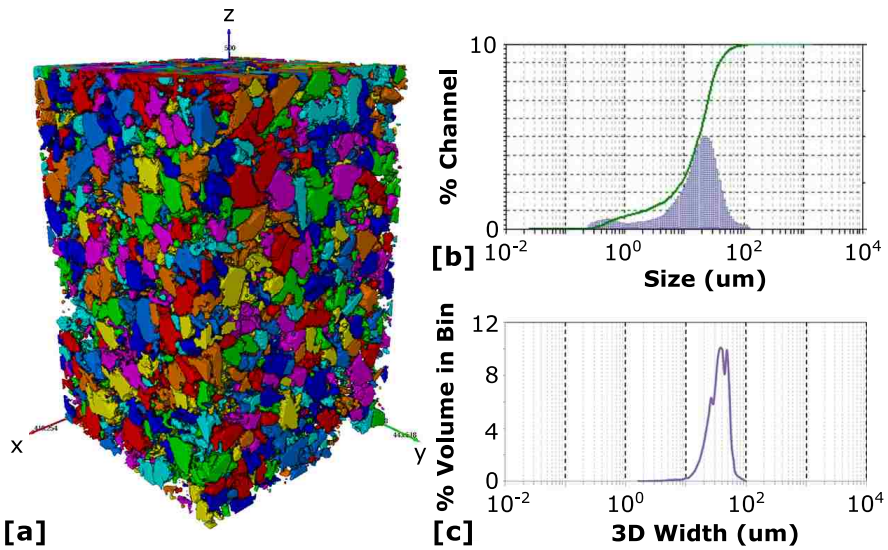

Figure 2.12: Computational and experimental particle size distributions.
[a] Computational particle separation of a MicroCT characterization.
[b] Experimental particle size distribution.
[c] Computational particle size distribution.

The quality of the geometry reconstruction was verified by comparing the FeS_2 volume fraction and particle size distribution with experimental values. The FeS_2 volume fraction (with respect to the total domain volume) was measured with Avizo's volume fraction module. Then, the relative error of the volume fraction was calculated by comparing the volume fractions from the Watershed segmentation to the experimental values. The mean relative error was -1.40% with a standard deviation of 2.11%, calculated from all eighteen reconstructions (Section 2.5.2). The deviation from experimental values was unsurprising because of the sensitivity of the reconstruction to the image processing methods, and the pixel size (0.5 μm) may have been insufficient to resolve smaller features.

Measurement of the FeS_2 reconstruction's particle size distribution was only measured for the first MicroCT characterization. The particle size distribution of the geometry reconstruction was compared to the corresponding particle size analysis

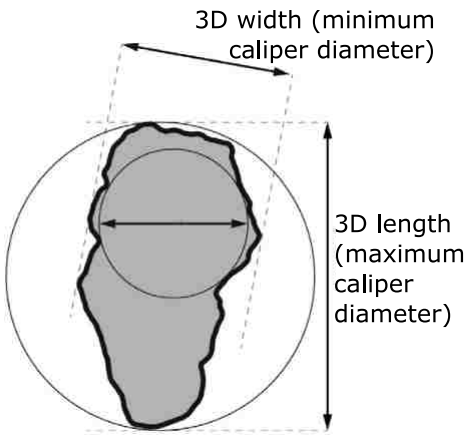

Figure 2.13: Diagram of how 3D particle measurements were performed. Adapted from Bagheri et al. [90].

performed with sonication, rather than the target size distribution, because distinct particles were expected to be visible from the MicroCT characterization. First, particles were identified and separated. Particle edges were dilated by one voxel in every direction, holes within particles were filled, and then the particles were eroded by one voxel in each direction and separated into distinct particles (Fig. 2.12a). After separating the particles, Avizo's label analysis module measured the 3D width and 3D length, also known as the minimum and maximum caliper diameters [90], respectively, of each particle (Fig. 2.13). These measurements were selected because the particles are irregularly shaped, and these measurements were easily compared to the "size" parameter generated from the complex light scattering techniques of the experimental particle size analyses. Each reconstructed particle's volume was tabulated as well. Then, the number of particles with a given size were binned by 3D width and 3D length. Each bin's volume percentage was calculated, and computational results were compared to the "% Channel" parameter from the experimental particle size analysis associated with the FeS_2 powder used to manufacture the characterized pellet (Fig. 2.12b-c). Only the 3D width is shown because the 3D length distribution was very similar. The computational results show a volume distribution similar to the experi-

mental results, but particles smaller than 1 µm did not appear in the computational distribution. This could be due to insufficient MicroCT resolution, because 0.5 µm pixels are not small enough to fully resolve 1 µm particles, or because the smaller particles appeared as one particle when characterized with MicroCT. This reveals that, while MicroCT was the best choice among other characterization methods for this material, the balance between domain size and resolution presents a challenge when characterizing polydisperse distributions.

Following reconstruction and verification of quality, the geometries were ready for meshing. This process will be discussed in Section 3.2.3.

Chapter 3

Computational Methods

3.1 Computational Cathode Analysis: Processing, Composition, and Slumping

Chapter 2 illustrated a method to determine the effect of processing parameters, composition, and slumping on the electrical conductivity of thermal battery cathodes. Section 1.4.2 described various computational approaches used to estimate effective properties, such as the effective electrical conductivity, and why the finite element method (FEM) was selected for this research. Application of this numerical method can provide a more fundamental understanding of the relationship between composition, processing parameters, and the effective electrical conductivity before and after slumping. This study is fundamental because model fidelity relies on correct selection of physics relevant to the system observed. In this case, electrostatics transport equations (Section 3.3) are applied to observe how electricity moves through the microstructure, and the results will unravel how processing and composition affect the electrical conductivity by affecting the microstructure.

Variation of processing and composition parameters was described in Section 2.2. The same parameters are applied for the computational study because the geometric representations used for this study originated from eighteen MicroCT characterizations (Section 2.5.2) of the same cathode pellets (nine pellet types, each type before and after slumping). Also, similar the experimental methods, cathode analyses are simplified by modeling the cathode with a solid electrolyte at steady state before and after slumping. This permits isolation of the effects of microstructural reorganization due to slumping. More specific details concerning the model will be covered in the following sections on application of the finite element method (Section 3.2), governing equations and boundary conditions (Section 3.3), and model verification exercises (Sections 3.4-3.5).

3.2 Numerical Methods

3.2.1 A Brief Introduction to the Finite Element Method

The modern finite element method is a computational technique to solve differential and integral equations in science and engineering. The method developed largely from the variational and weighted residual approaches, such as the Ritz and Galerkin formulations [40]. These methods approximate u, the solution to a differential equation, as a linear combination of unknowns, c_j, and appropriately chosen basis functions, ϕ_j. The linear combination describes the solution over the entire domain, and the *basis functions*, also known as *approximation fuctions*, are chosen to satisfy all of the problem's boundary conditions. Because the domain may be geometrically complex, it is represented as subdomains with simple geometric shapes, or *finite elements*. Finite elements allow systematic generation of basis functions to describe a given domain. Construction of the basis functions often employs interpolation theory, in which case

the basis functions are also called *interpolation functions*. From the basis functions, the variational and weighted residual methods are applied to solve differential and integral equations. The algebraic relationships between the unknowns and basis functions form the *finite element model*. This thesis applied the Galerkin FEM, detailed further in Appendix A and [40].

3.2.2 Sierra Mechanics

Aria, a coupled multiphysics Galerkin finite element program within Sierra Mechanics [91], was used to solve the finite element model on meshes with first order elements. A Trilinos linear solver applied the method of conjugate gradients (CG) and Jacobi preconditioning with a residual tolerance of 1×10^{-4} to solve the system of linear equations. Newton's method was used for the nonlinear solver, with 20 maximum nonlinear iterations and nonlinear residual tolerance of 1×10^{-12} for the governing equations (Section 3.3.1, Eqn. 3.1). The platform on which Aria was run was one of two multiprocessor, shared memory servers with 40 and 80 processors each, both using the Linux operating system. Individual simulations completed when the convergence requirements were satisfied, typically within two hours depending on the number of processors. Postprocessing variable outputs included the voltage, current density, and electric field.

3.2.3 Geometric Representations

Section 2.5.3 described the construction of the FeS_2 microstructure. Following isolation of the FeS_2 phase, Avizo smoothed the particles and meshed them with a triangular surface mesh. Each particle mesh had approximately four million elements with 3 μm mean edge length. Mesh quality was checked by evaluating and manually

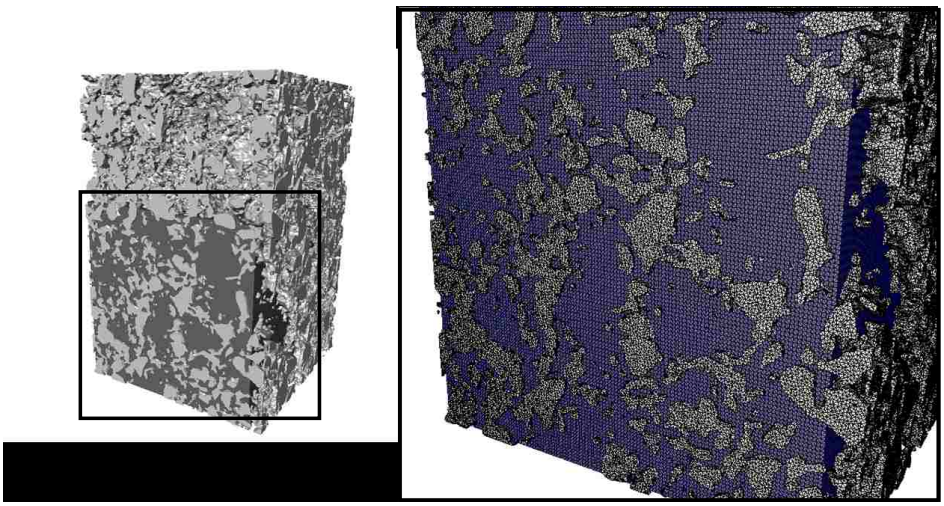

Figure 3.1: Particle and background meshes, shown overlapped.

fixing, if necessary, element intersections, orientations, and holes. The particle mesh was exported as an STL file for computational simulations (refer to Section 3.2.4). This process was repeated for all eighteen reconstructions (Section 2.5.2). Then, a geometry representing the background mesh was generated in CUBIT [92] as a cube with 300 μm edges, the largest cube able to fit within the bounds of all eighteen MicroCT reconstructions. A cube was chosen to maintain uniform lengths during anisotropy evaluation (Section 3.5.3). The cube was meshed in CUBIT with a hexahedral mesh, which was then converted to a tetrahedral mesh and exported as a Genesis file. The background mesh had nearly 83 million elements with 1.25 μm edge length. Fig. 3.1 illustrates the particle and background meshes.

3.2.4 Conformal Decomposition Finite Element Method

The *conformal decomposition finite element method* (CDFEM) [93] is a novel capability within Aria developed to model free and moving boundary problems with complex topological changes, such as simulations of flowing suspensions [94]. This process prevents issues such as mesh tangling in transient models, but a significant additional

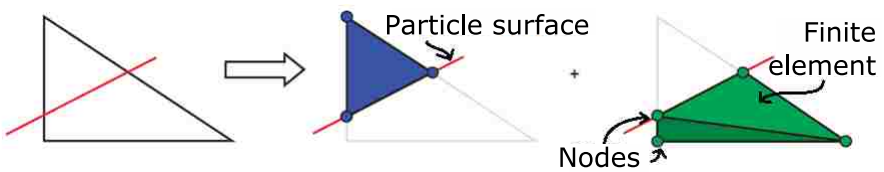

Figure 3.2: The effect of CDFEM on a particle surface, adapted from Noble et al [93].

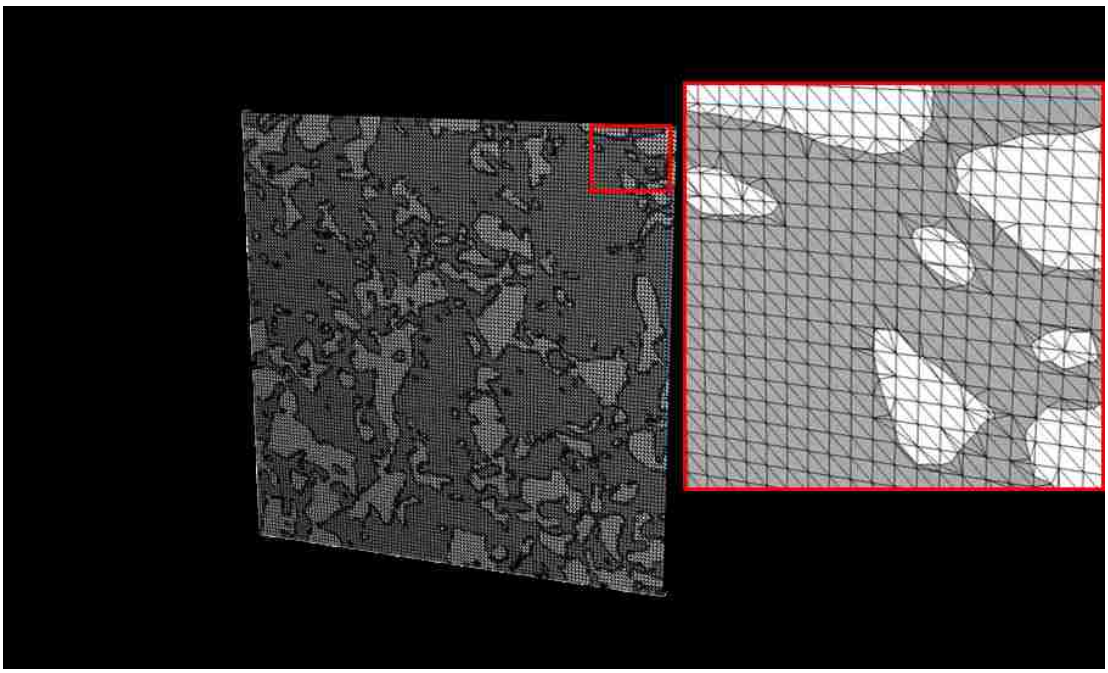

Figure 3.3: CDFEM applied to a cathode geometry.

advantage was also realized by CDFEM pertaining to meshing complex geometries. CDFEM was selected for this research for its ability to efficiently and effectively model complicated geometries, such as the FeS_2 particles generated from MicroCT reconstructions. This attribute of CDFEM was demonstrated when it was applied to complex geometric representations reconstructed from FIB/SEM by Roberts et al. [45] for a study of mechanical deformation and stress due to lithium intercalation in lithium ion-electrodes.

Table 3.1: Electrical conductivities of FeS_2 chemical components and the conductivities assigned in the model.

Component	Electrical Conductivity (1/Ωm)	Model Conductivity (1/Ωm)
FeS_2	0.2 - 5623.2 at 298K [12]	10
LiCl/KCl electrolyte	approximated $\leq 10^{-10}$	0.01
MgO binder	10^{-8} - 10^{-16} at 298K [95]	
Li_2O lithiating agent	approximated $\leq 10^{-10}$	
Pore space	approximated $\leq 10^{-10}$	

The CDFEM algorithm [45, 93] efficiently generates a single conformal mesh for an entire domain containing particles with complex geometries. It reads into Aria both the background and particle meshes, then decomposes nonconformal background mesh elements that exist along the boundaries of particles, creating smaller elements. Decomposition is followed by node enrichment along the interfaces (Fig. 3.2).

3.3 Model Setup

The three-dimensional, porous, composite cathode material was represented as a two-phase material for simplification. Each phase was given a constant electrical conductivity (Table 3.1). The two phases were (1) solid FeS_2 particles and (2) electrolyte, binder, lithiating agent, and pores (EBLP). This approximation is valid because the electrical conductivity of the FeS_2 semiconductor is much greater than the electrical conductivity of the EBLP components, especially below the electrolyte's melting point. Simulations applied the simplification that the electrolyte was not molten, therefore the EBLP components were nonconductive compared to the FeS_2 and were treated as insulators, or dielectric materials ($\sigma \leq 10^{-10}$ 1/Ωm [96]). Reference values for the MgO binder supported this assumption, and electrical conductivities for

LiCl/KCl eutectic (below its melting point) and Li_2O and were not found in the literature. Gas trapped in the pore space was also assumed to behave as an electrical insulator. Section 3.4 provides verification for the model conductivities reported in Table 3.1.

3.3.1 Governing Equations

The governing equations for electrostatics transport are used to model cathode electrical conductivity. Most conductive materials exhibit behavior according to Ohm's law (Eqn. 3.1), where at constant temperature, the current density vector ($\mathbf{J}$) is proportional to the electric field vector ($\mathbf{E}$) with the proportionality described by the electrical conductivity tensor ($\boldsymbol{\sigma}$). This expression also relates the electric field to the vector representing the rate of change of the electric potential scalar, $\boldsymbol{\nabla} V$. Ohm's law can be inserted into the steady-state form of the equation of continuity for current, Eqn. 3.2. For more detail concerning the FEM model equations, see Appendix Section A.3.

$$\mathbf{J} = \boldsymbol{\sigma}\mathbf{E} = -\boldsymbol{\sigma}\boldsymbol{\nabla} V \tag{3.1}$$

$$\boldsymbol{\nabla} \cdot \mathbf{J} = 0 \tag{3.2}$$

3.3.2 Boundary Conditions

Experimentally, electrical measurements can be performed two ways: (1) voltage is applied, and current is measured, and (2) current is applied, and the voltage drop is measured. Similarly, the electrical conductivity was estimated from the governing equations with two methods: (1) voltage was controlled and the current flux was measured, and (2) the current flux was controlled and the voltage drop was measured.

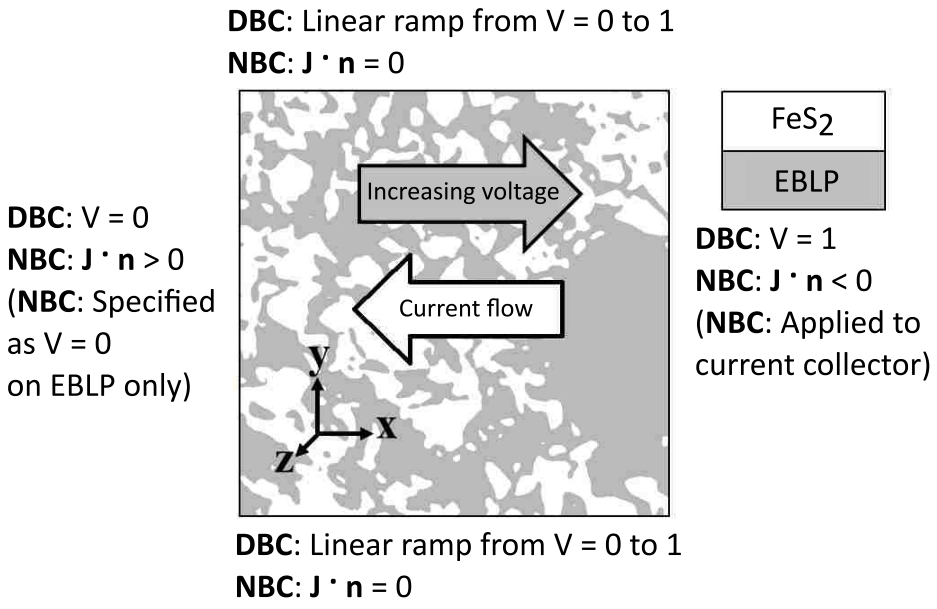

Figure 3.4: Boundary conditions specified for two simulations: Dirichlet boundary conditions (DBC) and Neumann boundary conditions (NBC). In this diagram, the voltage is applied in the $+x$ direction and current flows in the $-x$ direction.

These two methods, which employ different boundary conditions, bound the upper and lower electrical conductivity limits [97]. Dirichlet boundary conditions (DBC) determine the upper bound and Neumann boundary conditions (NBC) determine the lower bound. When the domain is large enough, the bounds converge to a single conductivity. Fig. 3.4 depicts the boundary conditions for each simulation applied to a cubic domain. For the Dirichlet boundary conditions, a constant potential was applied on the outer surfaces perpendicular to current flow and a linear voltage ramp was specified on all outer surfaces parallel to the current flow. For the Neumann boundary conditions, the current density flux ($\mathbf{J} \cdot \mathbf{n}$) was of equal magnitude with opposite signs on the outer surfaces perpendicular to current flow. The current flux was applied to a steel current collector ($\sigma = 10000$ 1/Ωm) on one side of the geometry to permit current to conduct naturally into the cathode, rather than forcing a constant current density direction and magnitude at the cathode surface. The voltage on

the EBLP phase was "pinned" to 0V on the cathode face furthest from the current collector. In addition, zero flux was specified on all outer surfaces parallel to the current flow.

The results shown in Fig. 3.5 show application of both sets of boundary conditions to a cathode geometry. Application of both sets of boundary conditions generated a linearly increasing voltage ramp along the x axis (Fig. 3.5a-b). The upper voltage limit appears higher for the DBCs in this example, however additional simulations with different cathode geometries but the same boundary conditions revealed that in some cases the maximum voltage of the NBCs exceeded that of the DBCs. Figs. 3.5c-d illustrate nearly uniform current densities with current density vectors pointing primarily toward the $-x$ direction, indicating current flow in the opposite direction of increasing voltage, as expected. The magnitude of current density appears greater in narrow connections between particles (Fig. 3.5d) in the NBC case. This demonstration illustrates that the Dirichlet boundary conditions, which define the upper bound, are voltage-controlled [97], and the Neumann boundary conditions, which define the lower bound, are current-controlled. Together, these two physical models provide a method to bound the effective electrical conductivity of composite microstructures.

Simulations with these two sets of boundary conditions require different methods to calculate the effective electrical conductivity of the composite, $\boldsymbol{\sigma}_{\text{eff}}$, which accounts for the conductivities of constituent phases. Eqns. 3.3 and 3.4 describe the effective conductivity calculations for the solutions calculated with Dirichlet and Neumann boundary conditions, respectively. These calculations were performed in Python [98]. In the following equations, $i = x$, y, or z; $\boldsymbol{\sigma}_{ii,\text{eff}}$ represents the effective electrical conductivity tensor component along axis i; J_i is the current density component along axis i; V is volume; L_i is the length along axis i; and E_i is the electric field component along axis i.

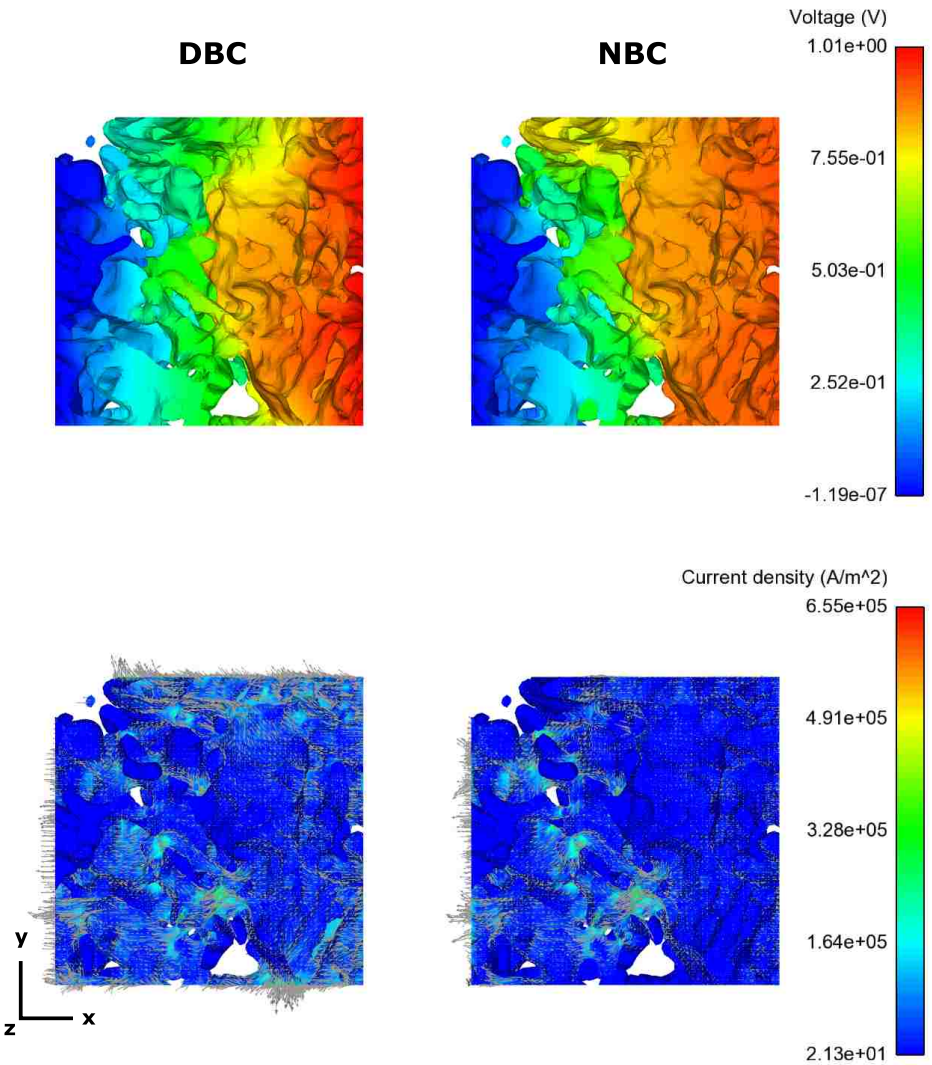

Figure 3.5: Example results of model setup applied to a cubic cathode geometry. Only the FeS_2 phase is depicted. Results from Dirichlet (left) and Neumann (right) boundary conditions are shown. This geometry represents one of the 1/64 subdomains applied for the domain volume verification exercises (Section 3.5.2).
[a, b] Electric potential field, V. Units = volts.
[c, d] Current density, **J**. Both magnitude (color) and direction (arrows) are indicated. Units = A/m^2.

$$\boldsymbol{\sigma}_{ii,\text{eff}} = -\frac{\frac{1}{\text{V}}\int\limits_{\text{V}} J_i \,\text{dV}}{\Delta V_i / L} \tag{3.3}$$

$$\boldsymbol{\sigma}_{ii,\text{eff}} = \frac{J_i}{\frac{1}{\text{V}}\int\limits_{\text{V}} E_i \,\text{dV}} \tag{3.4}$$

In the Dirichlet case, voltage was specified and current was measured. Eqn. 3.3 was solved by finding the volume integral of the current flux component along the primary axis of current flow and by specifying electric potential change along the axis of current flow, ΔV_i, as a 1V voltage drop. Alternatively, for the Neumann case, the current flux was specified and voltage was measured. Eqn. 3.4 was solved by applying the volume integral of the electric field component along the primary axis of current flow combined with the specified current flux, J_i. This value was found to be dependent on the domain volume, and was determined by averaging the flux over a surface perpendicular to the current flow in a modified NBC simulation, where voltage (V = 1V), rather than flux, was specified on the current collector. For the 0.027 mm^3 domain, J_i was applied as -4.5×10^3 A/m^2.

3.4 Verification Exercises: Simple Geometry

Verification exercises were performed to observe sensitivity of the model and method to important parameters such as background mesh size (h), the $\sigma_{\text{FeS}_2}/\sigma_{\text{EBLP}}$ ratio, domain size, and effects of anisotropy. Each of these parameters influence the fidelity of the computational results and should be tested to determine the optimal value of these input parameters, as well as limitations of the achievable parameters. First, verification exercises were performed on a simple idealized geometry, followed by application to a cathode geometry.

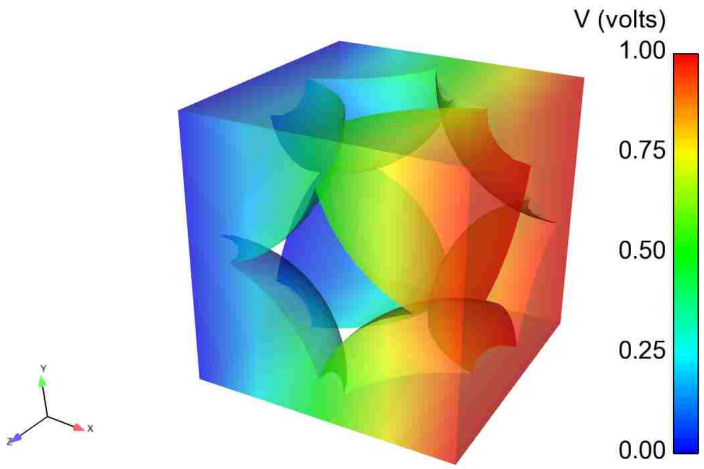

Figure 3.6: Simple geometry used for the verification exercises, shown with the electric potential field, V. Only the particles are depicted.

CDFEM was applied to a simple geometric representation (Fig. 3.6) with eight overlapping spheres ($r = 1.05\,\mu\text{m}$), representing FeS_2 particles, within a cubic background volume ($\text{V} = 8\,\mu\text{m}^3$). The sphere centers intercepted the cube's vertices, and the spheres were united where they overlapped with each other. The geometries were selected to mimic the composite cathode material with two phases, where the more conductive phase was connected throughout the material and in contact with outer surfaces along the x axis, and voltage was applied according to Dirichlet boundary conditions. The geometry sizes were chosen for ease of scaling. The geometries were generated and meshed with CUBIT. The surface triangular mesh size was 1 μm and the tetrahedral background mesh size was varied. The effects of background mesh resolution and electrical conductivity ratios ($\sigma_{\text{FeS}_2}/\sigma_{\text{EBLP}}$) were observed for verification.

Fig. 3.7 shows the relative error for the surface area and volume fraction (calculated with respect to the surface mesh) and the effective electrical conductivity (calculated with respect to results from the finest mesh, $h = 0.03125\,\mu\text{m}$). The order of convergence between the two smallest meshes was approximately 0.26, 2.16, and

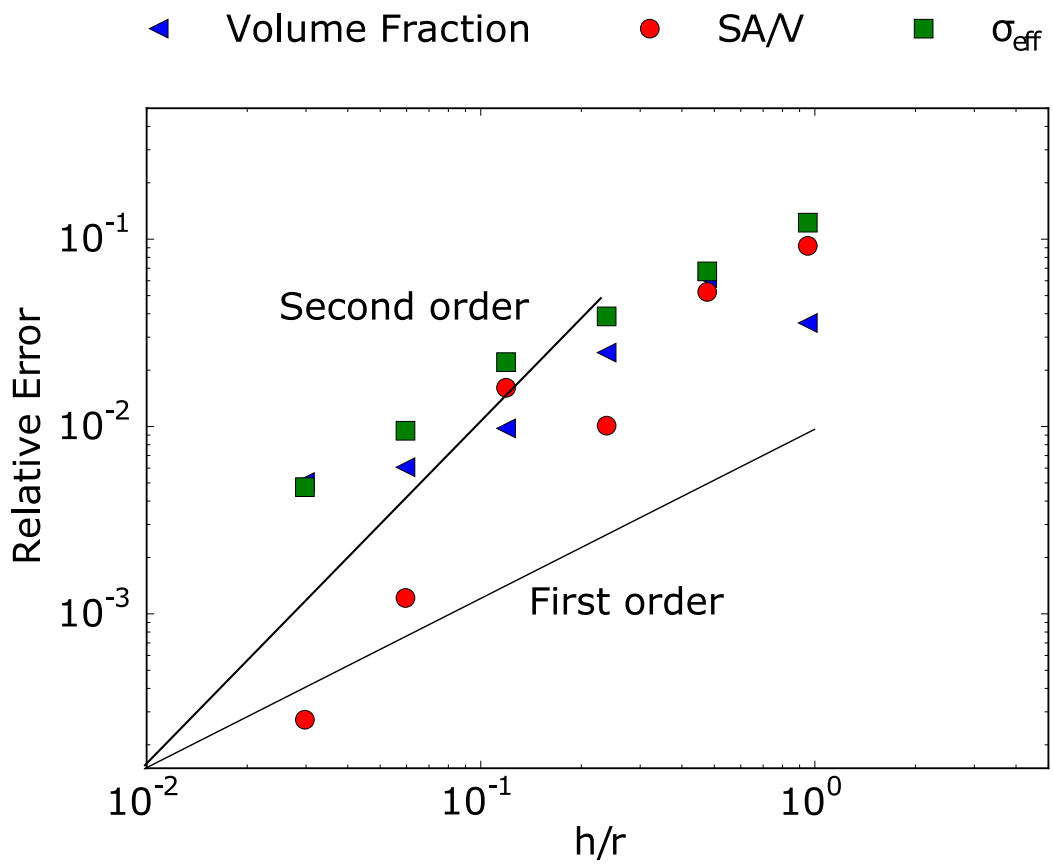

Figure 3.7: Mesh resolution study for CDFEM verification exercise on a simple geometry. The relative error of volume fraction and surface area over volume (SA/V) were calculated with respect to the surface mesh. The relative error of σ_{eff} was calculated with respect to the geometry with the finest mesh resolution, $h = 0.03125\,\mu\text{m}$.

1.87 for the relative error of volume fraction, SA/V, and σ_{eff}, respectively. The effect of background mesh refinement on the surface area and volume fraction demonstrates how the background mesh determines the final mesh resolution. When the mesh is coarse, smooth surfaces are coarsened, resulting in changes to the volume and surface area. This affects conduction through the particles, observed by changes to σ_{eff}. Mesh refinement smooths and resolves the surfaces until they more closely resemble the geometry represented by the particle surface mesh. The ratio of the background mesh resolution to the particle radius, h/r, provided a method of comparing what

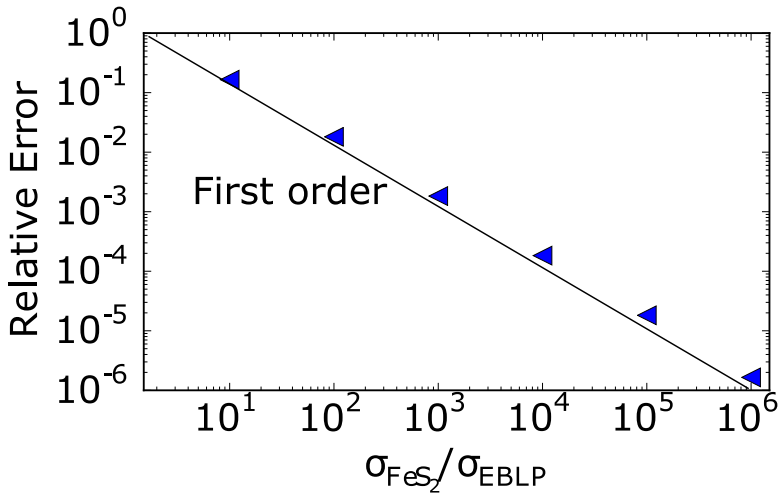

Figure 3.8: The effects of $\sigma_{\mathrm{FeS_2}}/\sigma_{\mathrm{EBLP}}$ on the relative error. Relative error was calculated with respect to σ_{eff} calculated from a simulation that applied $\sigma_{\mathrm{FeS_2}}/\sigma_{\mathrm{EBLP}} = 10^7$.

happens to particles when the background mesh resolution is varied. An $h/r = 0.12$ limits the relative error to approximately 1%, and smaller ratios continue to decrease the error. An $h/r \geq 1$ causes distortion of the geometry. A coarse background mesh (compared to the particle size) will eliminate small particles, resulting in a decreased particle volume fraction. In addition, particles with small gaps between them (also relative to the background mesh) can be joined, resulting in an increased particle volume fraction. These observations were expected to affect the cathode geometry because of the wide FeS_2 particle size distribution.

Literature values for the electrical conductivity ratio ($\sigma_{\mathrm{FeS_2}}/\sigma_{\mathrm{EBLP}}$) in Table 3.1 differ by several orders of magnitude. Using the lowest $\sigma_{\mathrm{FeS_2}}$ and the highest conductivity from all components in the EBLP phase, $\sigma_{\mathrm{FeS_2}}/\sigma_{\mathrm{EBLP}} = 10^7$. The sensitivity of σ_{eff} to $\sigma_{\mathrm{FeS_2}}/\sigma_{\mathrm{EBLP}}$ was tested by applying conductivity ratios between 10 and 10^7 with the same geometry (spheres in a cube, Fig. 3.6) and a background mesh with $h = 0.0625\,\mu\mathrm{m}$ ($h/r = 0.06$).

Fig. 3.8 illustrates the relative error of σ_{eff} with respect to σ_{eff} calculated from a simulation with $\sigma_{FeS_2}/\sigma_{EBLP} = 10^7$. First order convergence was observed. A ratio $\sigma_{FeS_2}/\sigma_{EBLP} \geq 10^3$ provided relative error less than 1%. This verified that reducing the conductivity ratio is a reasonable simplification. Thus, simulations on the actual cathode geometries applied $\sigma_{FeS_2}/\sigma_{EBLP} = 10^3$, as shown in Table 3.1.

3.5 Verification of Cathode Reconstructions

Following verification exercises on a simple geometry, additional exercises were performed on a geometric representation reconstructed from MicroCT. All verification simulations used only the first geometric representation from eighteen MicroCT characterizations. Voltage and current were applied along the x axis, $h = 1.25\,\mu\text{m}$, electrical conductivity was constant for a given phase, and the domain volume was 0.027 mm^3. The upper and lower conductivity limits was determined for each simulation using the Dirichlet boundary conditions, and in some cases the Neumann boundary conditions were applied.

The background mesh resolution was varied to study its effects upon conductivity, FeS_2 volume fraction, and SA/V, similar to the method used for verification on the simpler geometry (Section 3.4). The background mesh sizes varied, while the particle mesh resolution remained constant.

3.5.1 Mesh Resolution

The effect of mesh resolution was studied by repeatedly halving the background mesh size, h, until the simulation failed in Aria (Fig. 3.9). The smallest achievable mesh resolution was $h = 1.25\,\mu\text{m}$. This achieves $h/r = 0.41$ (where $r = 1/2$ of the *mean* particle diameter of the reconstructed geometry) or $h/r = 4.2$ (where $r = 1/2$ of

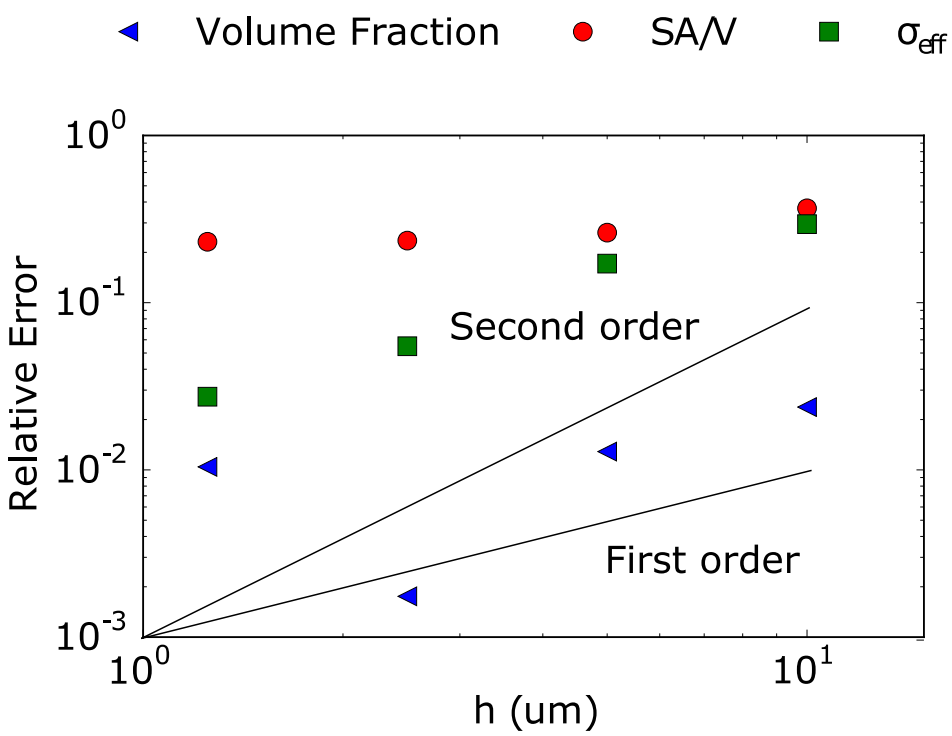

Figure 3.9: Error calculated from the mesh resolution sensitivity study applied to a cathode geometry. The volume fraction and SA/V error is calculated with respect to the surface meshed (STL) particle volume fraction and SA/V, and the error for σ_{eff} is calculated with respect to the value obtained from the smallest achievable mesh, $h = 1.25\,\mu\text{m}$.

the *minimum* particle diameter of the reconstructed geometry). As discussed in Section 3.4, an $h/r \leq 0.12$ leads to $\leq 1\%$ relative error, and $h/r > 1$ changes the geometry by eliminating small features and connecting features with small gaps between them. Thus, with respect to the mean particle diameter, the mesh resolution seems sufficient; in contrast, with respect to the minimum particle diameter, the mesh is far too coarse. Recalling the discussion in Section 3.4, particles smaller than the most resolved background mesh are eliminated from the CDFEM mesh and gaps between particles are not resolved, which alters the volume fraction, SA/V, and ultimately, the conductivity because the percolation network is altered.

Fig. 3.9 demonstrates this affect, as it illustrates how the error changes with mesh refinement. Shown are the relative error for volume fraction and SA/V (both calculated with respect to the surface meshed particles) and the error calculated with respect to the conductivity from the most resolved mesh. The order of convergence between the two smallest meshes was approximately 0.02 and 2.39 for the relative error SA/V and σ_{eff}, respectively. The conductivity error is quickly converging to the value from the most resolved mesh. In contrast, the relative error of the volume fraction is noisy and does not appear to be converging, and the SA/V error is converging very slowly, if at all. This is likely due to the coarseness of the CDFEM mesh compared to small or smooth features. Again, as mentioned in Section 3.4, if the mesh is too coarse, it will alter small features and either eliminate the small features altogether or connect features that, if resolved better, would be separated. This affects the particle surface area, volume, and volume fraction. If the CDFEM mesh could be resolved further, particularly in areas with smaller gaps and features, the results would improve.

A background mesh with $h = 1.25\,\mu\text{m}$ was applied to all eighteen reconstructions. The relative error calculated from comparision of the experimental volume fraction to the binarized reconstruction, surface mesh, and CDFEM mesh is shown in Fig. 3.10. This plot shows that the effects of image processing and binarization via a Watershed algorithm led to relative error within $\pm 5\%$. Binarization was followed by smoothing algorithms in surface meshing, which further changed the volume of FeS_2 (Fig. 3.11), with relative error $\pm 10\%$. The smoothing algorithms applied for efficient generation of a surface mesh changed the geometry, resulting in volume loss. Then, application of CDFEM further altered the volume fraction to a relative error $\pm 10\%$. The background mesh resolution was not resolved enough to maintain the volume fraction of the surface mesh, but it was similar. These results demonstrate that the best achievable background mesh resolution altered the geometry and could affect the effective conductivity results.

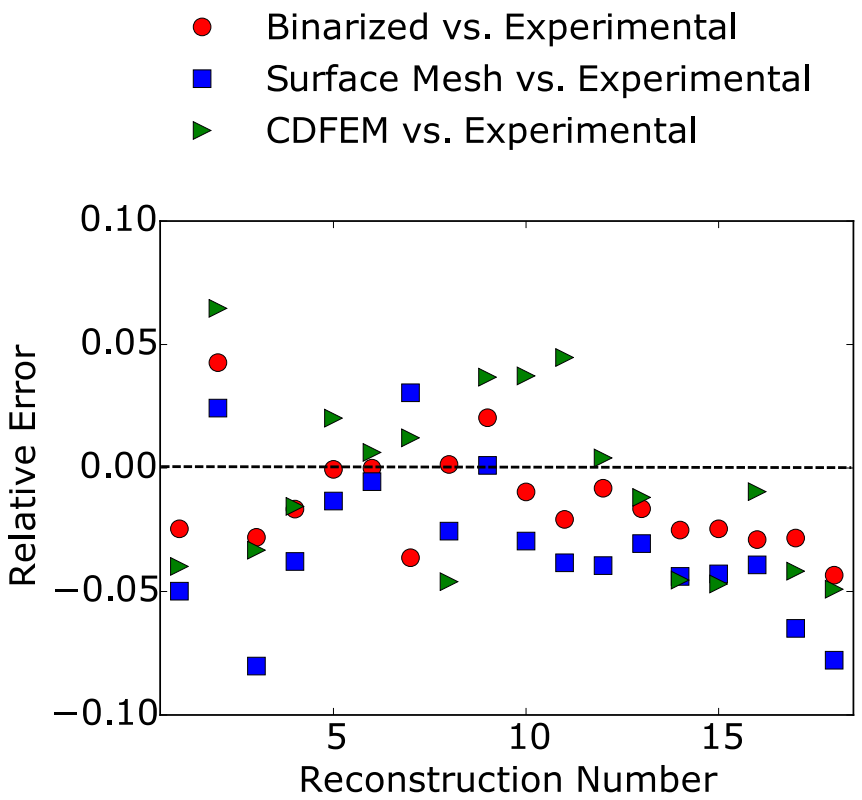

Figure 3.10: Relative error of the FeS_2 volume fraction, calculated with respect to experimental volume fractions.

3.5.2 Domain Volume

Kanit et al. [99] described a *representative volume element* (RVE) as the minimum sample needed to statistically represent the properties of a composite, heterogeneous material. The RVE can also be described as the simulation volume required to achieve the mean value of an effective property with 1% relative error using only ten spatially randomized simulations. The RVE depends on the physical property of interest, the contrast of phase properties, volume fractions of each phase, the acceptable level of error for the effective property estimation, the number of simulations, boundary conditions, and the phase distribution morphology. An extensive RVE study with four or five subdomain volumes was not performed, but the method described by Kanit

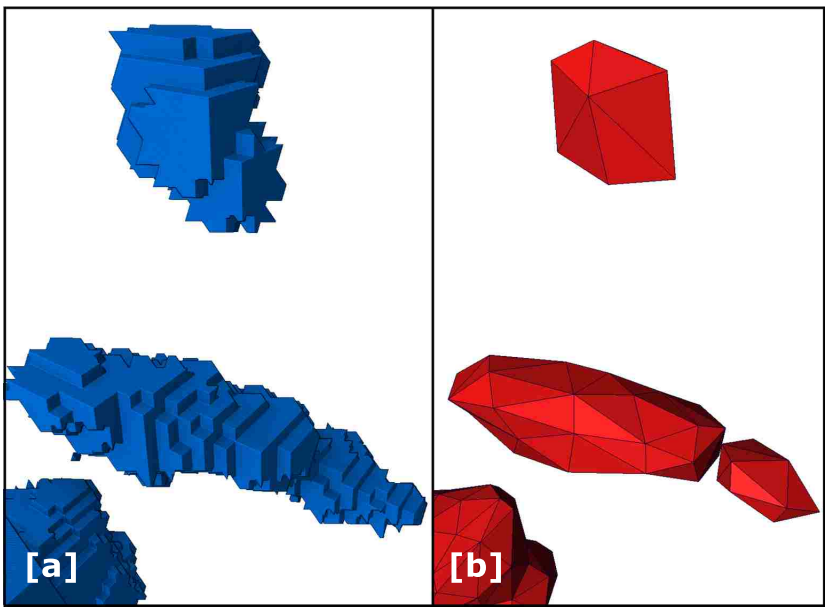

Figure 3.11: [a] A voxelated geometric representation of a few FeS_2 particles. [b] The same particles, shown with a surface mesh of the resolution used for cathode simulations. This example shows changes in the geometry due to surface meshing, such as volume loss due to excessive smoothing.

et al. was applied to study the effects of domain volume on the effective electrical conductivity.

Three volume sizes were selected as subdomain volumes of the full 0.027 mm^3 (300 µm edge length) domain (Table 3.2). n cubic subdomains with randomized locations within the full domain were generated for simulations applying each set of boundary conditions (Dirichlet and Neumann), for a total of $2n$ simulations for each subdomain. Then, the RVE for each set of boundary conditions, the number of simulation replicates ($n_{\text{projected}}$) necessary for 1% relative error for a given domain volume, and the expected relative error for a given domain volume were calculated.

The results presented in Figs. 3.12 and 3.13 show that the standard deviations from the DBCs and NBCs overlap. A full set of NBC simulations is not shown because these simulations have not yet run successfully on volumes larger than 1/8 of

Table 3.2: Subdomain volume size and replicate number. n simulations were run for every subdomain size and boundary conditions. The largest subdomain and the full domain (*) were not successfuly run with Neumann boundary conditions.

Subdomain Edge Length (μm)	n
300*	1*
225	3
150	10
75	10

the full domain. However, the successful results illustrate that greater error derives from the domain size than from the applied boundary conditions. Also, the mean conductivities show that the NBC is not always lower, as was expected, but because the standard devations overlap, this is not statistically significant. Both sets of boundary conditions show that the standard deviation, $n_{\text{projected}}$ and the relative error decrease as the domain volume increases, as expected [99]. Thus, the domain volume for the processing, composition, and slumping simulations (0.027 mm^3) is expected to vary when different boundary conditions are applied.

The RVE for Dirichlet boundary conditions was found to be approximately 0.310 mm^3. In addition, for 1% relative error associated with the 0.027 mm^3 domain, $n_{\text{projected}} = 91$ (Fig. 3.13). Without the largest subdomain simulations, the RVE and $n_{\text{projected}}$ for the NBC case could not be calculated. From this, it can be expected that the effective conductivities obtained with the 0.027 mm^3 domain are not truly representative of the microstructure characterized and reconstructed by MicroCT, and the volumes needed for the RVE is not currently attainable using this method and the resolution required for the sizes of FeS_2 particles. This may be due to the large regions, or pockets, of EBLP appearing in Fig. 3.14, which are very large compared to the full domain. Thus, if a more accurate effective conductivity estimation was

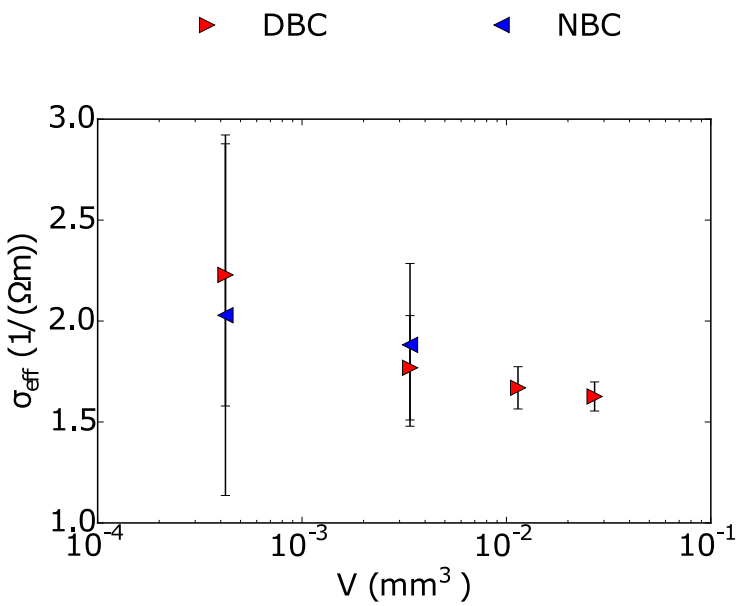

Figure 3.12: Mean effective electrical conductivities plotted with respect to simulation domain volume. Error bars represent the standard deviation calculated from n simulations. The full domain is also shown, with error bars calculated from the RVE method [99].

needed, iteratively generated small subdomains could more realistically be used to obtain a mean conductivity with 1% error.

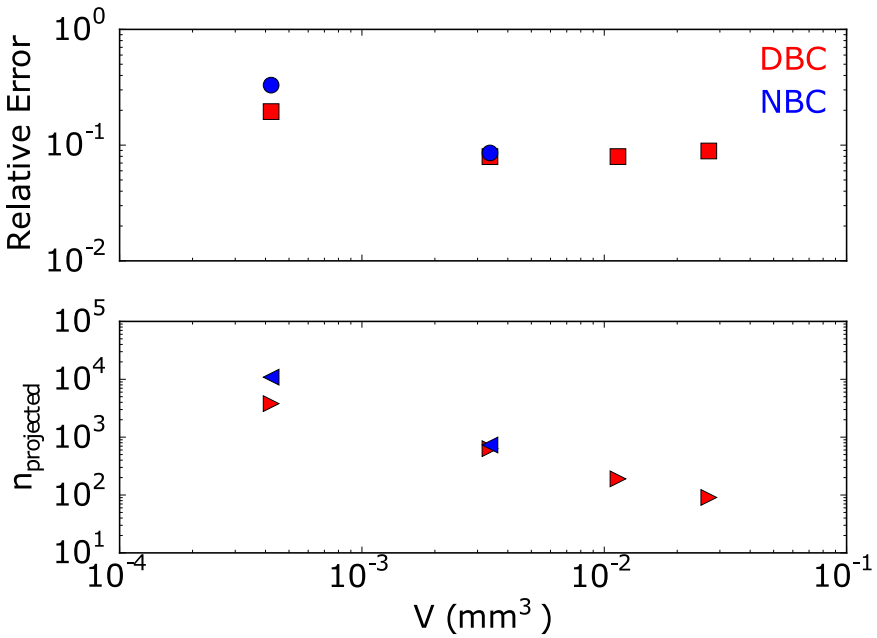

Figure 3.13: Number of simulation replicates required for 1% relative error and relative error for a given simulation domain volume.

3.5.3 Anisotropy

All boundary conditions in Fig. 3.4 were rotated to apply the voltage and current along the x, y, and z axes to determine if the effective electrical conductivity was *isotropic*, or consistent throughout the material in every direction, or anisotropic. As illustrated in Fig. 3.15, the mean values for $\sigma_{ii,\text{eff}}$ and standard deviations overlapped to a small extent. The σ_{yy} range was greater than the other two axes, though by a small amount. This result suggests that, within the established error, the conductivity was nearly uniform in all directions of current flow (along the axes). Uniform conductivity is a characteristic of isotropic conductivity, and will be applied as a simplification to all simulations on cathode geometries.

The verification methods in the previous sections established that the cathode simulation domain is limited by CDFEM mesh resolution and volume. With this

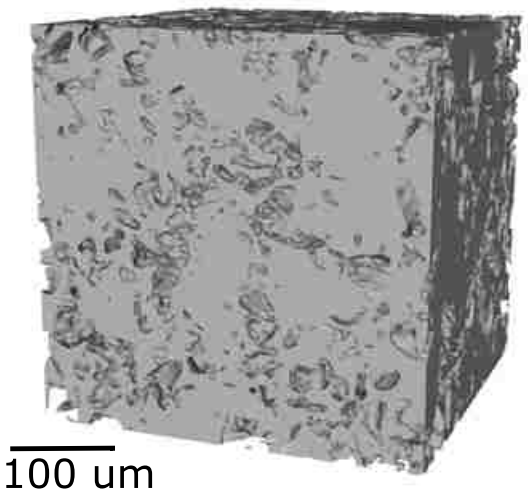

Figure 3.14: Isolated reconstruction of EBLP.

awareness, the background mesh resolution for all eighteen reconstructions applied a 1.25 μm background mesh over a 0.027 mm^3 geometry with $\sigma_{FeS_2}/\sigma_{EBLP} = 10^3$. All geometries are assumed to be isotropic. Only DBC results are reported because NBC simulations were not run successfully for the 0.027 mm^3. Reasons for this are currently unknown and undergoing investigation.

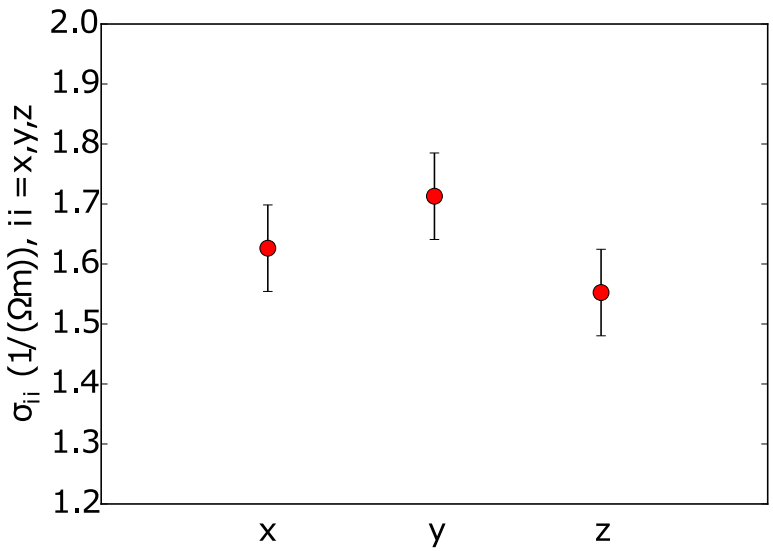

Figure 3.15: Effective conductivity results for each axis. The expected standard deviation for this domain size [99] is represented by error bars. Only one sample was analyzed.

Chapter 4

Results and Discussion

This chapter begins with a discussion of the results from experiments and FEM simulations and consideration of regression models, followed by implications of these results with respect to the process-microstructure-property-performance relationship.

4.1 Processing, Composition, and Slumping

Figure 4.1 shows the effects of processing, composition, and temperature on electrical conductivity before and after slumping. Prior to slumping, conductivity increased with temperature, density, and FeS_2 composition. The particle size distribution was shown to have little or no clear effect. The conductivity increase with temperature was expected due to the semiconducting properties of FeS_2. As temperature increases, greater thermal energy excites an increasing population of electrons across the conduction band. The effect of density and composition upon conductivity prior to slumping is unsurprising. Greater density provides greater contact between particles and less porosity, which creates better conduction of electricity through the microstructure. Similarly, greater FeS_2 content, indicated by the increase in the composition variable, means that more conductive particles are present for electrical conduction. A

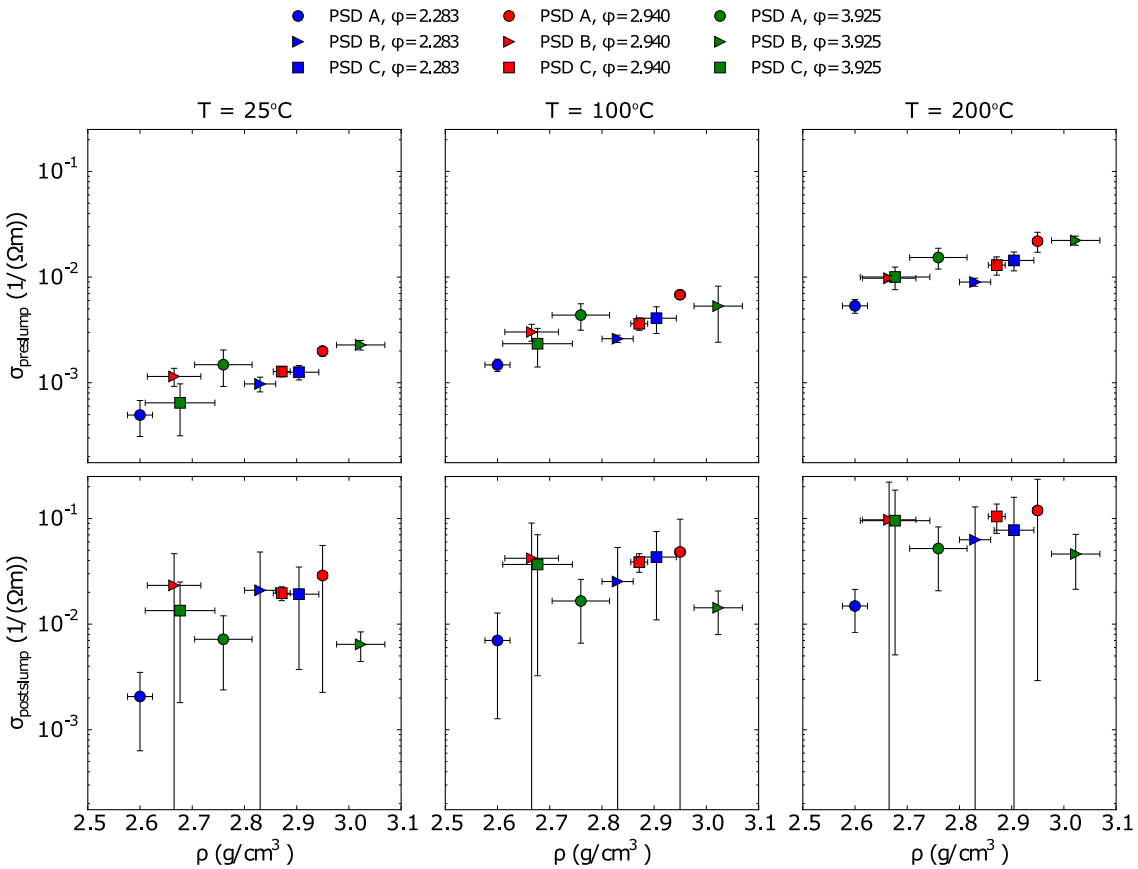

Figure 4.1: Mean electrical conductivity of experimental data for preslumped (top) and postslumped (bottom) samples at 25, 100, and 200^{o}C. Error bars represent standard deviations, calculated from triplicate samples.

lack of influence due to the particle size distribution may be from the use of particle size distributions that were too similar to observe a clear effect. If disagglomeration of FeS_2 occurred during the pellet manufacturing process, particularly pressing, the distributions may have been polydisperse and overlapping, as shown the particle size distributions in Fig. 2.2. In combination, these results demonstrate an ability to experimentally predict electrical conductivity from density, composition, and temperature prior to slumping.

After slumping, no trend due to processing or composition variables is visible, but the conductivity continued to increase with temperature. The conductivity also increased after slumping. Overlapping standard deviations indicate a lot of noise among replicates. Also, before slumping, the conductivities at a given temperature varied over nearly one order of magnitude. After slumping, the conductivities varied over more than one order of magnitude at a given temperature, and the variability increased.

The postslump results indicated that *the effect of processing and composition, within the ranges tested, is erased after slumping.* The amount of error associated with these results makes it difficult to determine the cause. Slumping involved heating the cathode past the salt's melting point, thus creating contact between the molten salt and FeS_2 particles during slumping. Measurement occurred after the salt returned to its solid state, however from these results it is apparent that the material was altered during slumping. Slumping may have enhanced the effects of minor and trace elements in FeS_2 that were already present prior to slumping. Minor and trace elements are significant because they can cause the conductivity of natural FeS_2 to vary by four orders of magnitude at one temperature [12]. In addition, the effects of oxidation, which can affect FeS_2 particles within minutes of exposure to oxygen [100], could have altered the conductivity. For instance, contact with the molten salt may have altered oxide layers on the particles. Characterization of the extent of these issues was not performed for this thesis. However, the effect of confounding variables such as these is apparent and was enhanced by the slumping process.

The simulation results are shown in Fig. 4.2. Both the preslumped and postslumped data from FEM simulations indicate little to no trend with respect to processing or composition parameters, or slumping. The purpose of the mesoscale simulations was to probe effects of processing and composition on the microstructure before and after slumping. Because no clear trend was observed, these results suggest

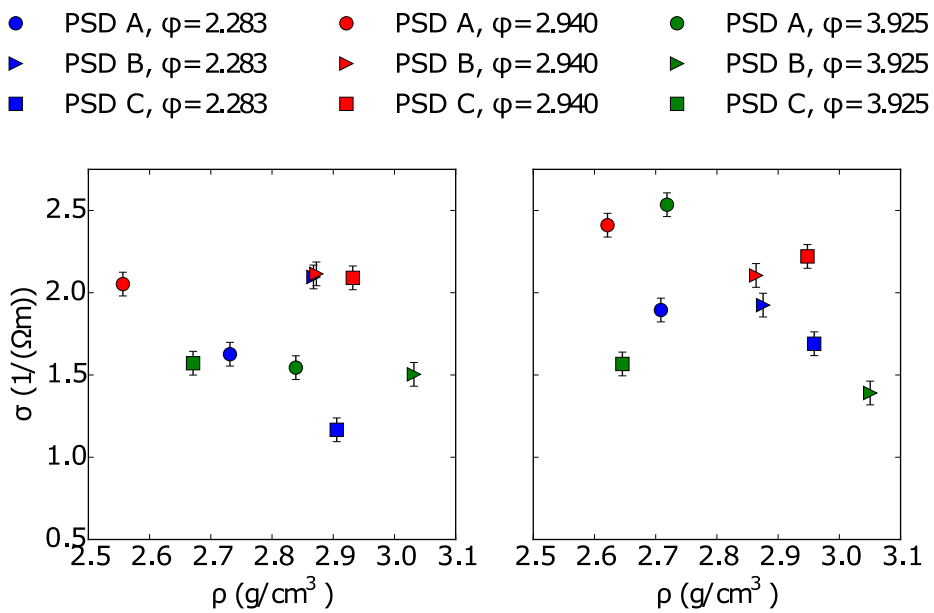

Figure 4.2: Electrical conductivity of preslumped (left) and postslumped (right) DBC simulations. The densities indicate the preslumped densities of the pellets characterized by MicroCT. Error bars represent standard deviations expected for this domain size [99].

that the selected range of processing and composition parameters, as well as slumping, did not affect the microstructure as it was studied. The results do *not* mean that the microstructure is not influenced by these parameters. The simulation study was limited by (1) the model physics, (2) domain size, (3) mesh resolution, and (4) the characterization method.

The model physics was limited because the simulations were simplified compared to the experimental situation. The simulations did not capture all of the physics involved in the experimental data, and they were not intended to. The effects of temperature, impurities, and oxidation were not replicated in the simulation because microstructural effects were the simulation focus. The simulations treated the microstructure as a bicomposite material with uniform properties throughout each phase, unaffected by variable material properties or environmental factors. Variabil-

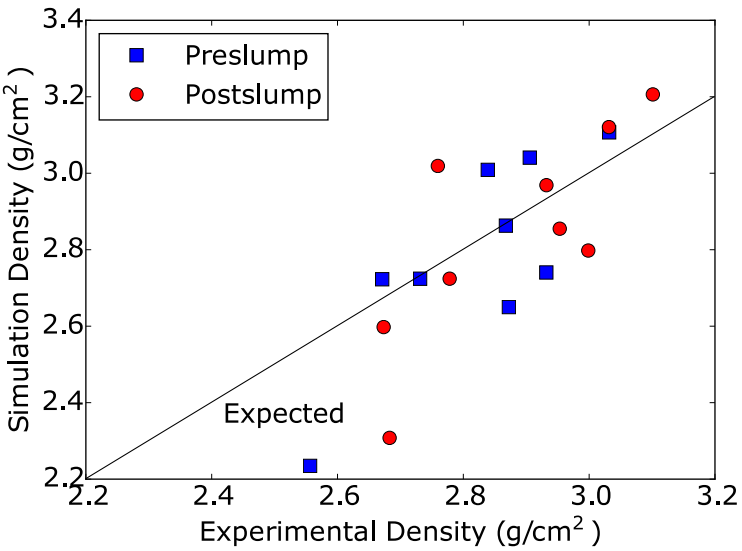

Figure 4.3: Comparison of the preslumped densities for the pellets characterized by MicroCT and the densities of the simulation domain after CDFEM.

ity among triplicate experimental results reveals that the cathode properties were not perfectly uniform.

The simulations were also limited by domain size, discussed in Section 3.5. The effect of domain volume on the apparent density is visible in Fig. 4.3, which shows how the experimental density compared to the apparent density of the simulations after application of CDFEM. This limitation suggests spatial density variations within the characterized pellets, meaning that the density of each domain volume likely deviated from the bulk pellet density. For this reason, the density was corrected using a linear relationship between FeS_2 volume fraction and density, which provided a more accurate plot of the simulation results (Fig. 4.4). A better method would have considered the porosity and content of each component within each simulation domain, but because the cathode geometry was simplified to two phases, these values were unknown and the linear approximation was applied.

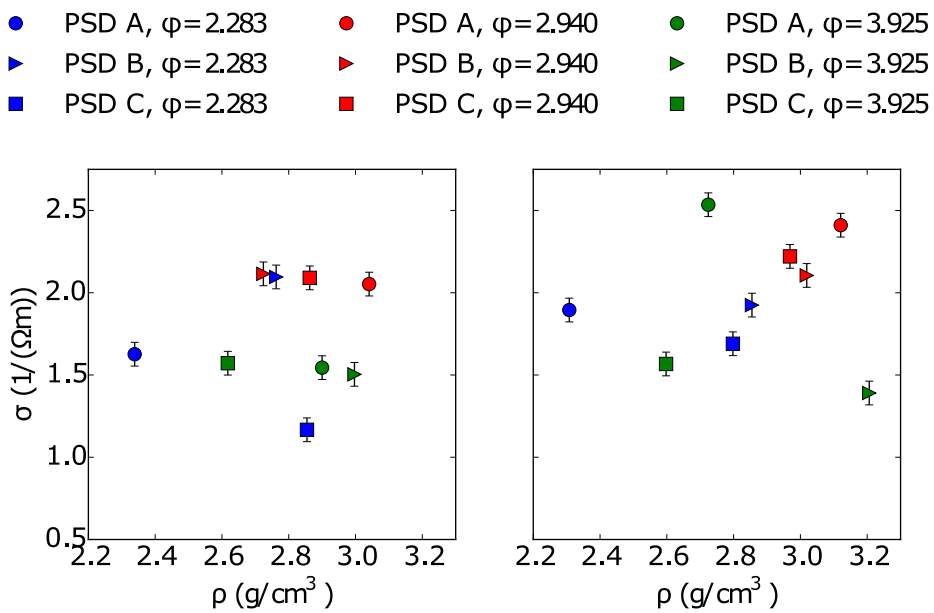

Figure 4.4: Electrical conductivity of preslumped (left) and postslumped (right) DBC simulations using corrected densities. Error bars represent standard deviations expected for this domain size [99].

The data presented in Fig. 4.4 show a change in simulation results compared to the uncorrected densities in Fig. 4.2, but the preslumped results continue to lack the clear density trend obtained from the experimental results, as well as effects from the composition ratio. This comparison suggests that the simulations lack fidelity compared to the experiments, likely because of the imposed simplifications.

The corrected postslumped simulation results in Fig. 4.4 show a slight where conductivity increases with density after slumping. This was not observed experimentally. This could be due to greater contact between particles, forming a more extensive percolation network for electron conduction through the material. If this is a true observation, this simulaton is valuable because the experimental results were extremely variable and the effects of density were indeterminable. More data would help determine if this is an actual trend or just noise.

Another limitation of the simulations was the mesh resolution, discussed in Section 3.5. From these verification exercises it was found that in addition to a greater domain volume, better mesh refinement in areas with small features could improve the validity of the simulation results. Without this improvement, a coarse background mesh causes elimination of small particles and connection of small gaps, which alter the microstructure representation.

And lastly, the characterization method was limited by sample preparation for and orientation in MicroCT system. This would have most significantly affected the comparison of preslumped to postslumped results. The eighteen samples characterized by MicroCT were eighteen different pellets fractions, two of each pellet type. These two pellets were similar and of the same type, but were two different pellets. One was slumped and the other was not. Had the MicroCT characterization been limited to the same nine pellet fractions, each before and after slumping, the simulation results could have been very different. Characterization of the same region within the pellet fractions would have also improved the validity of the results. Furthermore, the sample orientation within the MicroCT system would have improved the simulations. As the MicroCT was performed for this thesis, the pellet orientation was not fixed, so the orientation of the pellets during characterization is not known. This means that the axis of pellet pressing and slumping was unknown. These details were overlooked during experimental planning, and it was expected that a change due to processing, composition, or slumping would have been observed using the applied method. However, the simulations may have been more sensitive to these changes if the microstructural characterization had been performed more carefully. Furthermore, the pixel size was too large to capture the smallest FeS_2 particles. Further improvement of this characterization method could resolve these particles.

These results illustrate the importance of model physics, domain volume, mesh resolution, and microstructure characterization when comparing simulations to ex-

perimental results. These limitations caused the simulations to lack validity, but the experimental results could also be improved to minimize noise in the data.

An additional method of analysis was applied to extract the strength of composition and processing effects before and after slumping: regression analysis. This method of statistical analysis permits quantification of the importance of each parameter relative to all other parameters, as well as quantification of the regression model's goodness-of-fit (R^2 values) and its ability to predict future results (R^2_{fit} values). Regression analysis applied Minitab's regression model fit tool. In each regression model, first order terms and all second-order interactions were considered. Continuous input variables included as-pressed pellet density (ρ), mean of each targeted particle size distribution (α, based on the sieve openings), composition ratio of FeS_2 to EB (ϕ), and temperature (T, in Kelvins). The simulation regressions applied the corrected densities. The FeS_2 particle size distributions were treated as continuous variables despite their polydisperse nature because the processing method, sieving, targeted specific particle size distributions with standard sieve sizes. The regression equation is described by Eqn. 4.1, and Table 4.1 shows the coefficients and goodness-of-fit determined from the regression equations. Residual plots (Appendix B.2) provide an evaluation of the goodness of each regression model fit to the data, in addition to the R^2 values in Table 4.1. The only regression fits that were strong and had predictive value were the preslump experimental fit and the postslump experimental fit.

$$\sigma = C_1 + C_2\rho + C_3\alpha + C_4\phi + C_5T + C_6\rho\alpha + C_7\rho\phi + C_8\rho T + C_9\alpha\phi + C_{10}\alpha T + C_{11}\phi T \quad (4.1)$$

The sensitivity of the general regression equation to individual variables was probed by taking the partial derivative of the regression equation with respect to the variable of interest, multiplied by that same variable (Eqns. 4.2-4.5). This

Table 4.1: Regression model results for fitting data to σ. ρ = pellet density (prior to slumping) in g/cm^3; α = mean diameter of the targeted particle size distribution, based on the sieve opening sizes, in µm; ϕ = composition ratio of FeS_2 to EB; and T = temperature, in Kelvins.

Variable	None	ρ	α	ϕ	T	$\rho\alpha$	$\rho\phi$
Coefficient	C_1 (1/Ωm)	C_2 (cm^3/Ωm*g)	C_3 (1/Ωmµm)	C_4 (1/Ωm)	C_5 (1/ΩmK)	C_6 (cm^3/ Ωm*gµm)	C_7 (cm^3/Ωm*g)
Experiment, Preslump	-0.0136	-0.012	0.00531	-0.0159	-0.000403	-0.001527	0.00697
Experiment, Postslump	-1.6	0.628	0.0154	0.283	-0.00057	-0.0074	-0.1119
Simulation, Preslump	8.94	-4.48	-0.26	1.966	-	0.139	0
Simulation, Postslump	2.78	0.013	-0.097	0	-	0.0271	0
Variable	ρT	$\alpha\phi$	αT	ϕT			
Coefficient	C_8 (cm^3/ Ωm*gK)	C_9 (1/Ωmµm)	C_{10} (1/ΩmµmK)	C_{11} (1/ΩmK)	R^2	R^2_{pred}	
Experiment, Preslump	0.000169	-0.000216	-0.000001	0.000016	88.42	84.48	
Experiment, Postslump	0.000175	0.00059	0.00001	0	33.03	10.96	
Simulation, Preslump	-	-0.0464	-	-	92.6	0.0	
Simulation, Postslump	-	0	-	-	97.74	93.96	

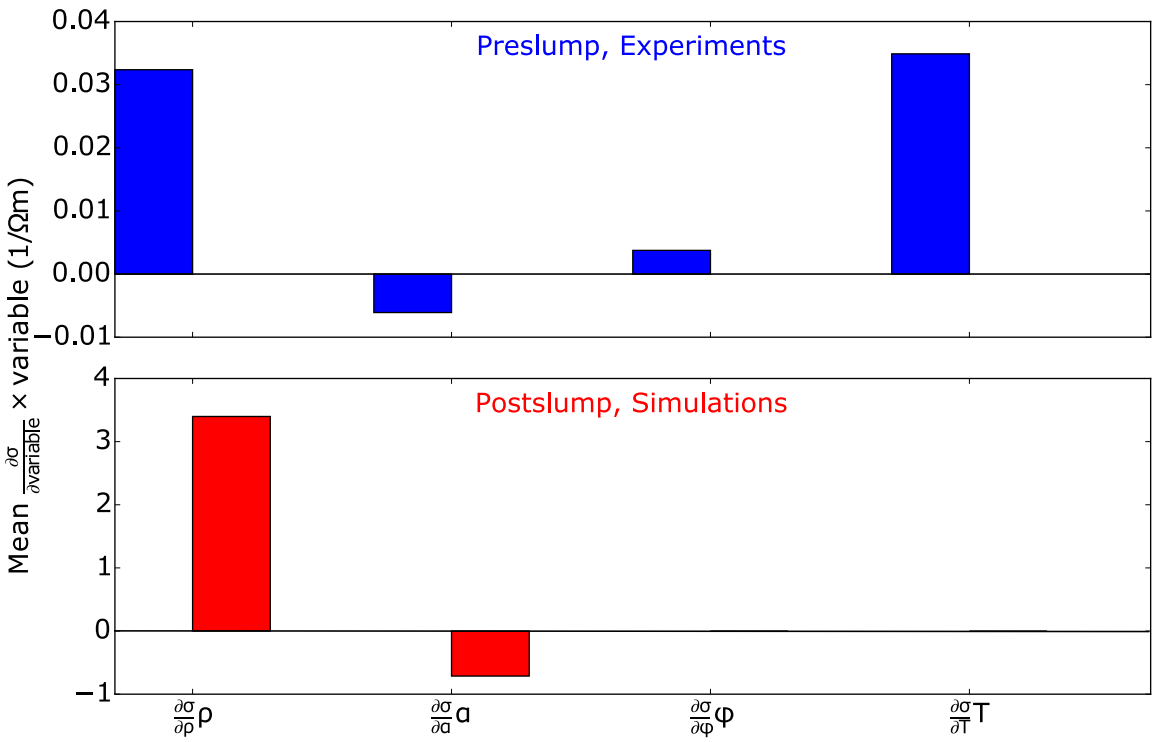

Figure 4.5: Plot of Eqns. 4.2-4.5, applied to preslump experimental and postslump simulation results. Bar graph magnitude represents the mean $\left(\frac{\partial\sigma}{\partial \text{variable}} \times \text{variable}\right)|_{\text{min values}}$ and $\left(\frac{\partial\sigma}{\partial \text{variable}} \times \text{variable}\right)|_{\text{max values}}$. Additional results (experimental postslump and simulation preslump) were omitted due to their poor predictive value (see R^2_{pred} in Table 4.1).

method provided a quantitative comparison of the importance of each variable for the actual values (density, composition, etc.) tested in this study. Fig. 4.5 depicts the relative importance of each variable, calculated by taking the mean of $\left(\frac{\partial\sigma}{\partial \text{variable}} \times \text{variable}\right)|_{\text{min values}}$ and $\left(\frac{\partial\sigma}{\partial \text{variable}} \times \text{variable}\right)|_{\text{max values}}$.

$$\frac{\partial \sigma}{\partial \rho}\rho = \rho(C_2 + C_6\alpha + C_7\phi + C_8T) \tag{4.2}$$

$$\frac{\partial \sigma}{\partial \alpha}\alpha = \alpha(C_3 + C_6\rho + C_9\phi + C_{10}T) \tag{4.3}$$

$$\frac{\partial \sigma}{\partial \phi}\phi = \phi(C_4 + C_7\rho + C_9\alpha + C_{11}T) \tag{4.4}$$

$$\frac{\partial \sigma}{\partial T}T = T(C_5 + C_8\rho + C_{10}\alpha + C_{11}\phi) \tag{4.5}$$

From Fig. 4.5, the most important preslump experimental parameters include density and temperature, followed by particle size distribution and composition. The most important postslump simulation parameters are density and particle size distribution. These results are particularly interesting because they reveal similar trends in the experiments and simulations, particularly increasing conductivity with density and decreasing conductivity with increasing particle size. The trends shown here coincide with physics; conductivity increases with density, FeS_2 composition, and temperature, and decreases with increasing FeS_2 particle size. The physical relevance of all parameters except particle size were discussed earlier. An increasing particle size reduces the number of achievable points of contact between conductive particles, but as the particle radius decreases, more contact is possible. This increases conductivity. Thus, the regression fits demonstrate a physically relevant model that can predict the relationship between conductivity, composition, processing parameters, and temperature for both preslump experimental and postslump simulation results. The regression model's ability to predict postslump experimental and preslump simulation results is limited.

In combination, the results from the experiments, simulations, and regression analysis showed that processing and composition has a strong effect on the experimental preslump electrical conductivity and postslump simulation conductivity. The experimental effect of processing and composition appears to be erased after slump-

ing, and the effect upon conductivity before slumping in the simulations is absent. These results indicate that more effort remains to obtain experimentally validated simulations.

With respect to thermal battery performance, the results suggest that an effect of slumping should be visible upon thermal activation. When a Li/FeS_2 thermal battery is heating prior to activation, it should become more electrically conductive, even before ionic conductivity takes effect when the electrolyte melts. After the electrolyte melts and the cathode slumps, the conductivity should be enhanced from decreased cathode resistance, which could improve performance. The magnitude of this effect is unknown because the effect of slumping when the electrolyte is molten was not studied, but the effect is expected from the observed experimental results. Following activation and electrolyte solidification, the effects of processing and composition (within the ranges studied) would be erased. In addition, a lack of uniform FeS_2 properties could impact results. This implies that application of the observations made from this thesis could improve thermal battery design and performance.

Future work to improve this research would include (1) chemical analysis and purification of the FeS_2 prior to pellet pressing, (2) protection from or characterization of oxide layer formation, (3) investigation of the reason for variability in the postslumped results, (4) increased simulation domain volume, (5) improved mesh resolution on small features, and (6) improvement of the MicroCT characterization method to improve the FEM model fidelity. Together, these changes could provide greater predictive value for the link between processing, microstructure, properties, and performance.

Chapter 5

Conclusions

This thesis presented a combined experimental and computational approach to determine the relationship between Li/FeS_2 thermal battery cathode composition and processing parameters and electrical conductivity. The influence of these composition and processing parameters was observed before and after slumping, the mechanical deformation induced by thermal activation and microstructure reorganization. The experimental approach employed impedance spectroscopy for electrical conductivity tests and MicroCT characterization of cathode pellets for generation of representative geometries for the computational approach. This computational approach applied CDFEM and Ohm's law to estimate the effective electrical conductivity of the cathode microstructures reconstructed from MicroCT.

The experimental results showed a predictive relationship between composition, processing parameters, and temperature before slumping. With increasing FeS_2 composition, as-pressed pellet density, and temperature the electrical conductivity increased. Regression analysis also revealed that the conductivity decreased with increasing FeS_2 particle size. After slumping, this predictive relationship was erased, although the conductivity increased further after slumping and continued to increase with temperature. The experimental results showed scatter at every temperature,

especially after slumping. This could be attributed to enhanced observation of effects from minor or trace elements or surface oxidation from atmospheric exposure. Further confounding of data could be due to the polydisperse nature of the FeS_2 particle size distributions and similar ranges tested for processing and composition parameters, selected for their feasability with respect to pellet manufacturing. The experimental results could improve with FeS_2 powder purification processes, prevention of FeS_2 exposure to oxygen and moist air, and monodisperse powders. In addition, these results suggest that slumping should improve thermal battery performance by minimizing the resistance in the cathode during activation, nonuniform FeS_2 properties may impact performance, and that the tested ranges of composition and processing parameters are not expected to impact results.

Simulation results revealed a weak or absent relationship between the cathode composition and processing parameters prior to slumping, with a dependence on the density after slumping. Regression analysis of postslump data revealed an inverse relationship between particle size distribution and conductivity. This suggests that the simulations lacked fidelity compared to the experimental results, but were valuable because they probed the effect of microstructure when the postslumped experimental results were noisy. The simulations would likely improve by accounting for variable material properties, improving the MicroCT characterization, increasing the simulation domain size (or many simulations over randomly located subdomains), and increasing mesh resolution for small features.

These results demonstrate the limitations of this computational model to predict the relationship between processing, microstructure, properties, and performance. However, improvement of the model could better probe this fundamental relationship, as well as save time, money, and material required for experiments. Experiments will always remain necessary, but the number of experiments required for a given study could be reduced by applying a computational approach, such as FEM. Further de-

velopment of this method could enhance performance prediction from microstructure and material property characterization.

Appendices

A Application of the Finite Element Method

B Minitab Statistics

C Discharge

D Vacuum Impregnation and Serial Sectioning with the Robo-Met.3D

Appendix A

Application of the Finite Element Method

The following sections apply the Galerkin FEM to the problem of interest. The chapter begins with the derivation of the applicable differential equation (Eqn. A.7), followed by development of the weak-form of the residual equation for the finite element model.

A.1 Derivation of the Model Differential Equation

The electric current density ($\mathbf{J}$) relates to the current (I) flowing through a surface (S) of arbitrary shape and macroscopic size by Eqn. A.1, where $\mathbf{n}$ refers to the normal vector [101].

$$I = \int_{\mathrm{S}} \mathbf{J} \cdot \mathbf{n} \, dA \tag{A.1}$$

The electric current entering an enclosed surface (S), and thus the volume (V) enclosed by it, are related by the divergence theorem in Eqn. A.2. In this equation, $\mathbf{n}$ refers to the outward normal vector and I is positive.

$$I = -\oint_{\mathrm{S}} \mathbf{J} \cdot \mathbf{n}\,\mathrm{dA} = \int_{\mathrm{V}} -\boldsymbol{\nabla} \cdot \mathbf{J}\,\mathrm{dV} \tag{A.2}$$

Furthermore, current is defined as the rate of charge (Q) transport through a surface, and relates to the charge density (ρ) by Eqn. A.3.

$$I = \frac{dQ}{dt} = \int_{\mathrm{V}} \frac{\partial \rho}{\partial t}\mathrm{dV} \tag{A.3}$$

The expressions in the volume integrals in Eqns. A.2 and A.3 equate to form the equation of continuity for current, Eqn. A.4, which for steady-state conduction reduces to Eqn. A.5.

$$\frac{\partial \rho}{\partial t} - \boldsymbol{\nabla} \cdot \mathbf{J} = 0 \tag{A.4}$$

$$\boldsymbol{\nabla} \cdot \mathbf{J} = 0 \tag{A.5}$$

Conducting materials exhibit behavior according to Ohm's law (Eqn. A.6), where at a constant temperature, the current density ($\mathbf{J}$) is proportional to the electric field ($\mathbf{E}$) with the proportionality described by the electrical conductivity ($\boldsymbol{\sigma}$). This equation also relates the electric field and the electric potential (V).

$$\mathbf{J} = \boldsymbol{\sigma}\mathbf{E} = -\boldsymbol{\sigma}\boldsymbol{\nabla}V \tag{A.6}$$

Eqns. A.5 and A.6 combine to form Eqn. A.7, assuming an orthotropically conducting medium, where each axis has a unique, but constant, σ. If the material is

isotropic, σ becomes constant in every direction. Eqn. A.7 relates the electric potential to electrical conductivity. With respect to composite materials, such as Li/FeS_2 thermal battery cathodes, this property is also known as the effective electrical conductivity, $\boldsymbol{\sigma}_{\text{eff}}$. Eqns. A.7 and A.8 describe the differential equation for this finite element model in a three-dimensional medium with domain Ω and boundary Γ. Eqn. A.8 is equivalent to Eqn. A.7, but in differential form with rectangular Cartesian coordinates.

$$-\boldsymbol{\nabla} \cdot (\sigma_{ii} \boldsymbol{\nabla} V) = 0 \text{ in } \Omega \tag{A.7}$$

$$-\frac{\partial}{\partial x}\left(\sigma_{xx}\frac{\partial V}{\partial x}\right) - \frac{\partial}{\partial y}\left(\sigma_{yy}\frac{\partial V}{\partial y}\right) - \frac{\partial}{\partial z}\left(\sigma_{zz}\frac{\partial V}{\partial z}\right) = 0 \text{ in } \Omega \tag{A.8}$$

A.2 Finite Element Approximations and Basis Functions

As mentioned in Section 3.2.1, the domain is divided into subdomains, or finite elements. Each finite element consists of a geometry, to describe the element shape, and an order of approximation for the unknown. The finite element domain is denoted by Ω^e with boundary Γ^e. Finite element shapes include triangles and quadrilaterals, and the order of approximation can be linear, quadrilateral, or even higher. The assembly of elements representing a domain (Ω^h), also known as the *mesh*, may not equal the true domain (Ω) if the geometry is too complex to replicate exactly (Fig. 3.11).

Basis functions are generated to approximate the voltage, or potential, over a finite element according to Eqn. A.9, where ψ_j^e is the basis function associated with the element and V_j^e represents the values of $V^e(x, y, z)$ at specific points, or *nodes*, on the element. The set of nodes used to describe an element's geometry must be

unique for the definition of basis functions. Node enrichment occurs when nodeless variables (c_j) are added (Eqn. A.10).

$$V(x,y,z) \approx V^e(x,y,z) = \sum_{j=1}^{n} V_j^e \psi_j^e(x,y,z) \tag{A.9}$$

$$V(x,y,z) \approx V^e(x,y,z) = \sum_{j=1}^{n} V_j^e \psi_j^e(x,y,z) + \sum_{j=1}^{m} c_j \phi_j(x,y,z) \tag{A.10}$$

Basis functions must satisfy the problem's boundary conditions exactly. Typically, basis functions are polynomials. The basis functions are applied to satisfy the governing differential equation over each element domain, and the unknowns are found. This results in a set of n algebraic equations (V_n^e) among the nodal values, a set also known as the finite element model. The finite element model can take on various forms. The *weak-form*, used in this thesis, employs basis functions equivalent to the weighting functions, as in the Ritz-Galerkin method.

A.3 Weak-Form Galerkin Development

Eqns. A.11 to A.16 derive the weak-form of Eqn. A.8. The weak-form is aptly named because differentiation is moved from V^e to a weighting function, thus weakening the continuity requirement. Eqn. A.11 represents the *weighted residual function* of Eqn. A.8, where the expression in square brackets is the *residual*, or error of the approximation, and $w(x,y,z)$ is the weighting function. The *weighted-residual finite element model* consists of a set of n linearly independent algebraic equations for every n independent selections of w. Because this model contains second-order differential equations, the basis functions (ψ_j^e) must also be twice differentiable with respect to x, y, and z. Thus, ψ_j^e must be quadratic or higher-order in x, y, and z coordinates.

$$0 = \int_{\Omega^e} w \left[-\frac{\partial}{\partial x}\left(\sigma_{xx}\frac{\partial V^e}{\partial x}\right) - \frac{\partial}{\partial y}\left(\sigma_{yy}\frac{\partial V^e}{\partial y}\right) - \frac{\partial}{\partial z}\left(\sigma_{zz}\frac{\partial V^e}{\partial z}\right)\right] dxdydz \quad \text{(A.11)}$$

Next, integration by parts redistributes the differentiation so that V^e and w are each differentiable only once with respect to x, y, and z. To do this, identities of the multivariable chain rule (Eqn. A.12) and the component form of the divergence theorem (Eqn. A.13) lead to Eqn. A.14.

$$\frac{\partial}{\partial x_i}(wf) = \frac{\partial w}{\partial x_i}f + w\frac{\partial f}{\partial x_i},\ -w\frac{\partial f}{\partial x_i} = \frac{\partial w}{\partial x_i}f - \frac{\partial}{\partial x_i}(wf) \quad \text{(A.12)}$$

$$\int_{\Omega^e} \frac{\partial}{\partial x_i}(wf)dxdydz = -\oint_{\Gamma^e}(wf)n_{x_i}d\mathrm{S} \quad \text{(A.13)}$$

where $x_i = x_1, x_2, x_3 = x, y, z$,

$f(x,y,z) = \sigma_{ii}\dfrac{\partial V^e}{\partial x_i}$,

dS is an infinitesimal arc length along the boundary Γ^e, and

n_{x_i} is the component of a unit normal vector along the x_i axis,

$\mathbf{n_i} = \sum_{i=1}^{3} n_{x_i}\mathbf{e_{x_i}}$ on the boundary Γ^e

$$0 = \int_{\Omega^e}\left(\sigma_{xx}\frac{\partial w}{\partial x}\frac{\partial V^e}{\partial x} + \sigma_{yy}\frac{\partial w}{\partial y}\frac{\partial V^e}{\partial y} + \sigma_{zz}\frac{\partial w}{\partial z}\frac{\partial V^e}{\partial z}\right)dxdydz$$
$$- \oint_{\Gamma^e} w\left(\sigma_{xx}\frac{\partial V^e}{\partial x}n_x + \sigma_{yy}\frac{\partial V^e}{\partial y}n_y + \sigma_{zz}\frac{\partial V^e}{\partial z}n_z\right)d\mathrm{S} \quad \text{(A.14)}$$

In Eqn. A.14, V^e is the *primary variable* because it is the dependent unknown variable, and the *secondary variable*, or the coefficient of w in the boundary term,

is J_n (Eqn. A.15). When V is specified on the boundary, this refers to an *essential boundary condition*, and when J is specified on the boundary, this is a *natural boundary condition*.

$$J_n = \sigma_{ii} \frac{\partial V^e}{\partial x_i} n_{x_i} \tag{A.15}$$

where J_n is the projection of the current flux vector $\mathbf{J}$ along $\mathbf{n_i}$

Combination of Eqns. A.14 and A.15 leads to the weak-form in Eqn. A.16. The weak-form can be separated into bilinear ($B(w,V)$) and linear forms ($l(w)$). $B(w,V)$ (Eqn. A.17), which is linear in both w and V, yields a coefficient or conductivity matrix $\mathbf{K}$, and $l(w)$ (Eqn. A.18) yields $\mathbf{F}$, which together form the finite element equations $\mathbf{KV} = \mathbf{F}$.

$$0 = \int_{\Omega^e} \left(\sigma_{xx} \frac{\partial w}{\partial x} \frac{\partial V^e}{\partial x} + \sigma_{yy} \frac{\partial w}{\partial y} \frac{\partial V^e}{\partial y} + \sigma_{zz} \frac{\partial w}{\partial z} \frac{\partial V^e}{\partial z} \right) dxdydz - \oint_{\Gamma^e} w J_n d\mathrm{S} \tag{A.16}$$

$$B(w,V) = \int_{\Omega^e} \left(\sum_{i=1}^{3} \sigma \frac{\partial w}{\partial x_i} \frac{\partial V^e}{\partial x_i} \right) dxdydz \tag{A.17}$$

$$l(w) = \oint_{\Gamma^e} w J_n d\mathrm{S} \tag{A.18}$$

In the weak-form, V^e must be linear in x, y, and z to avoid identically zero terms, and V^e is continuous across all elements. V^e, approximated as Eqn. A.9, and w, set as ψ_i^e approximation functions to obtain n algebraic equations with n unknowns, brings us from Eqn. A.16 to the weak-form Galerkin model, Eqn. A.19.

$$0 = \sum_{j=1}^{n} \left\{ \int_{\Omega^e} \left[\frac{\partial \psi_i^e}{\partial x} \left(\sigma \frac{\partial \psi_j^e}{\partial x} \right) + \frac{\partial \psi_i^e}{\partial y} \left(\sigma \frac{\partial \psi_j^e}{\partial y} \right) + \frac{\partial \psi_i^e}{\partial z} \left(\sigma \frac{\partial \psi_j^e}{\partial z} \right) \right] dxdydz \right\} V_j^e - \oint_{\Gamma^e} \psi_i^e J_n d\mathrm{S} \quad \text{(A.19)}$$

$$\sum_{j=1}^{n} K_{ij}^e V_j^e = J_i^e \quad \text{(A.20)}$$

where

$$K_{ij}^e = \int_{\Omega^e} \left[\frac{\partial \psi_i^e}{\partial x} \left(\sigma \frac{\partial \psi_j^e}{\partial x} \right) + \frac{\partial \psi_i^e}{\partial y} \left(\sigma \frac{\partial \psi_j^e}{\partial y} \right) + \frac{\partial \psi_i^e}{\partial z} \left(\sigma \frac{\partial \psi_j^e}{\partial z} \right) \right] dxdydz \quad \text{(A.21)}$$

$$J_i^e = \oint_{\Gamma^e} \psi_i^e J_n d\mathrm{S} \quad \text{(A.22)}$$

which is matrix notation is

$$\mathbf{K}^e \mathbf{V}^e = \mathbf{J}^e \quad \text{(A.23)}$$

where the coefficient matrix $\mathbf{K}^e$ is symmetric due to its bilinear form

Eqns. A.19 - A.23 complete the weak-form Galerkin development for the finite element model.

Appendix B

Statistics

B.1 DOE Analysis

B.2 Residual Plots for Regression Models

Table B.1: Statistical analysis of the DOE generated by Minitab.

Factorial Design Augmented According to D-Optimality	
Number of Candidate Design Points	81
Number of Design Points to Augment/Improve	27
Number of Design Points in Optimal Design	27
Condition Number	3
D-Optimality (determinant of (XTX))	387420489
A-Optimality (trace of inverse (XTX))	0.481481
G-Optimality (average leverage/maximum leverage)	1
V-Optimality (average leverage)	0.259259
Maximum Leverage	0.259259

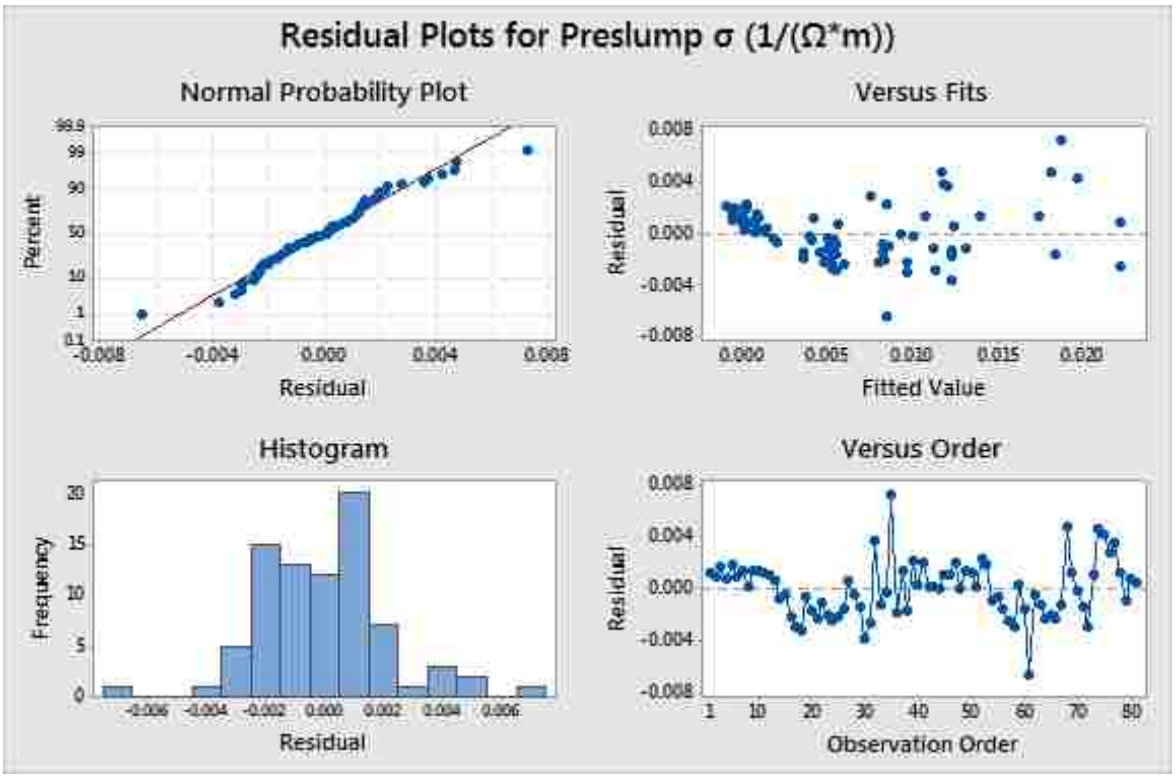

Figure B.1: Residual plots of the regression model equation for experimental conductivity prior to slumping. The nearly linear trend in the Normal Probability Plot (top left) shows a good fit of the regression model to the data. The funneling pattern shown in Residuals vs. Order (bottom right) occurred because the temperature increased with run order. The samples were divided into two sets, causing the funnel twice with respect to order.

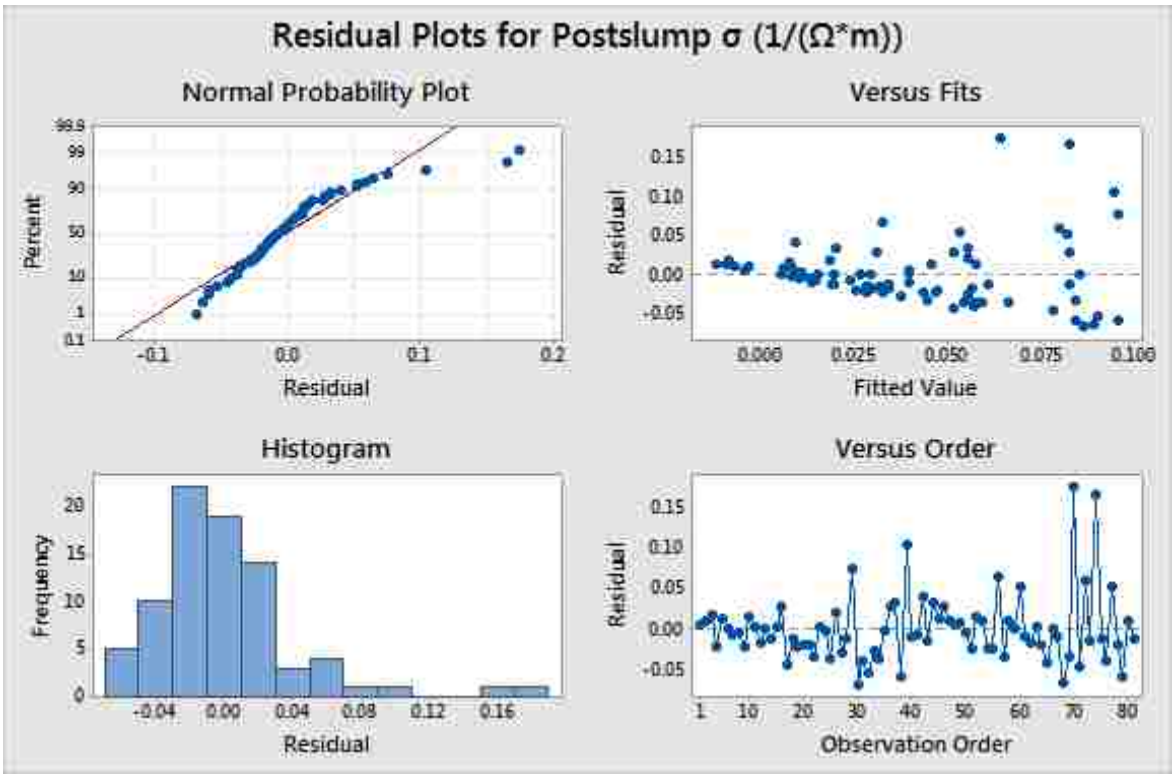

Figure B.2: Residual plots of the regression model equation for experimental conductivity after slumping. The nonlinear trend in the Normal Probability Plot (top left) shows a poor fit of the regression model to the data. The funneling pattern shown in Residuals vs. Order (bottom right) occurred because the temperature increased with run order. The samples were divided into two sets, causing the funnel twice with respect to order.

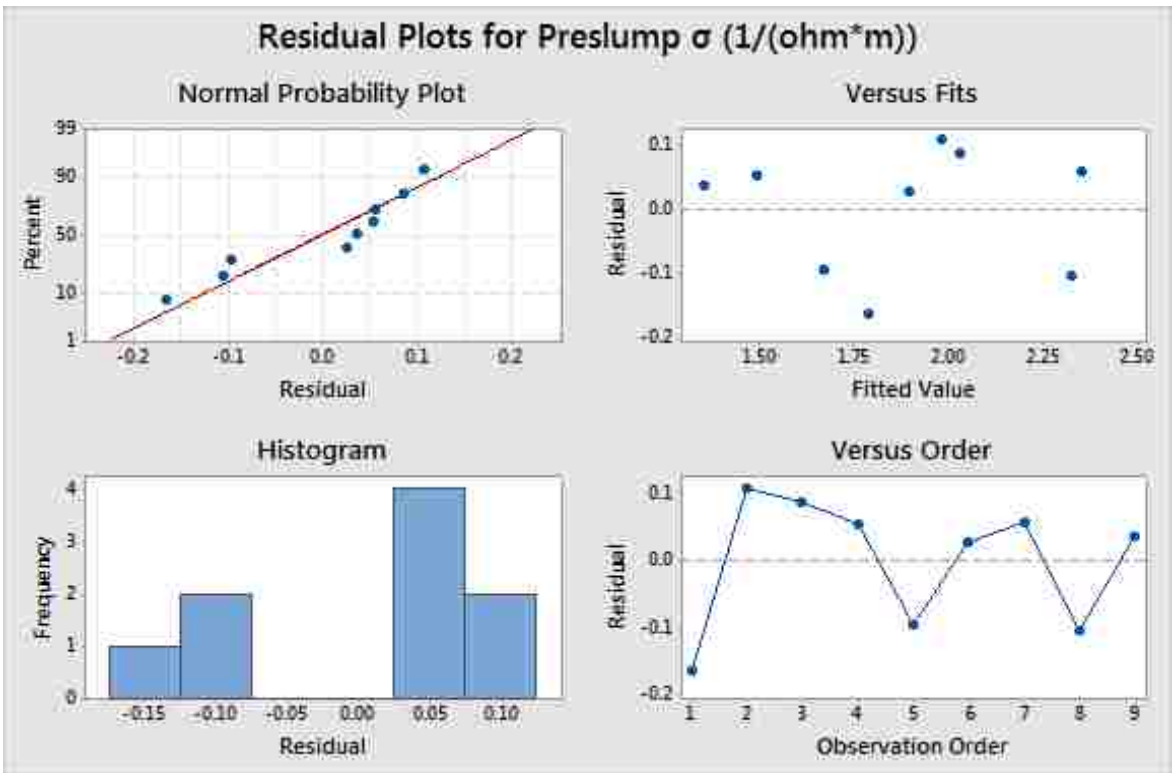

Figure B.3: Residual plots of the regression model equation for FEM simulation conductivity prior to slumping. The trend in the Normal Probability Plot (top left) and random distribution in Residuals vs. Fits (top right) and Residuals vs. Order (bottom right) indicate that the regression model is a good fit of the data.

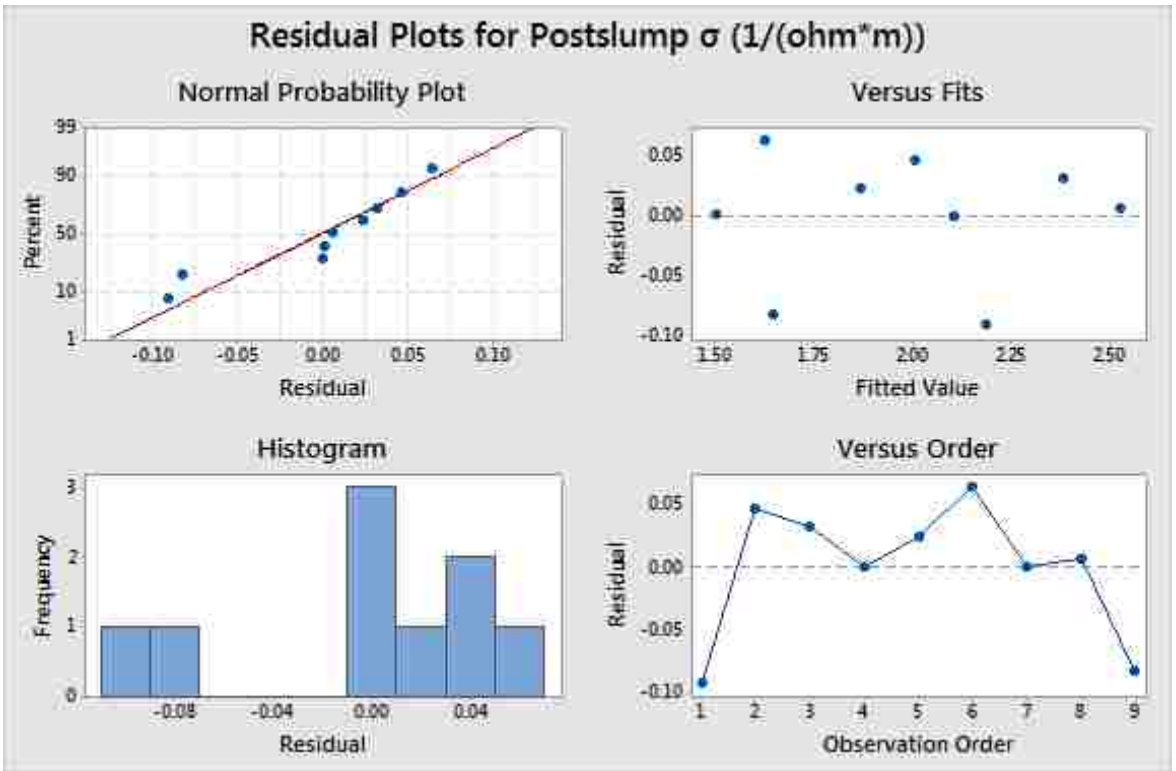

Figure B.4: Residual plots of the regression model equation for FEM simulation conductivity prior to slumping. The nearly linear trend in the Normal Probability Plot (top left), nearly normal distribution in the Histogram (bottom left), and random distribution in Residuals vs. Fits (top right) and Residuals vs. Order (bottom right) indicate that the regression model is a good fit of the data.

Appendix C

Discharge

Section 1.3 described the cathode electrochemistry in an activated Li/FeS_2 thermal battery. The first product from the reduction of FeS_2, $Li_3Fe_2S_4$ (the "Z-phase"), exhibits a conductivity nearly two orders of magnitude lower than that of FeS_2 [13]. Formation of the Z-phase during discharge affects cathode impedance and overall cell performance. The effect of this electrochemical reaction upon the cathode effective conductivity was simulated by generating an arbitrarily chosen 3 μm less conductive outer layer on all FeS_2 particles. The outer layer conductivity was 0.1 $(\Omega m)^{-1}$, and the core remained a constant 10 $(\Omega m)^{-1}$. Dirichlet boundary conditions were applied to the geometry.

The effect of adding a less conductive surface layer to the FeS_2 particles is shown in Fig. C.1. The plot illustrates that the mean effective conductivity decreases by one order of magnitude when a less conductive layer of 3 μm is added to FeS_2 particles. This reflects what is expected during discharge when the electrochemistry proceeds to produce the less conductive Z phase. However, this set of simulations does not provide the full picture. This study of discharge effects will be expanded at a later time, and will include variations of the thickness of the less conductive outer layer.

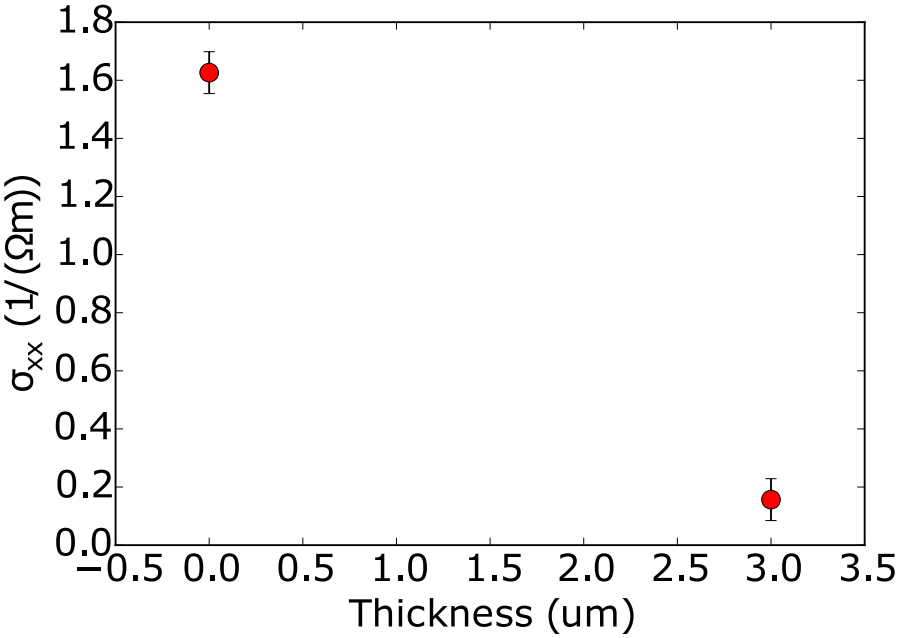

Figure C.1: Effective electrical conductivities of FeS_2 particles with a less conductive outer layer. Outer layer thickness is indicated. Error bars indicate the expected standard deviation for this domain volume [99].

Appendix D

Vacuum Impregnation and Serial Sectioning with the Robo-Met.3D

Initial serial sectioning results performed by the Robo-Met.3D with water as the solvent and the initial KX impregnation process provided poor characterization results (Fig. D.2). The data was unusuable for 3D reconstruction for a representative geometry because the resolution was not fine enough and the edges experienced significant material loss. Customization of the Robo-Met.3D with lapping oil and hexane, combined with the optimized vacuum impregnation process, improved results greatly. Characterization of a cross-section by SEM showed a noticeable decrease in pull-out and surface roughess with little effect upon the orientation of iron disulfide particles (Fig. D.1). The serial sectioning results also improved, though the quality was still not fine enough to meet the resolution requirements described in Chapter 1 (Fig. D.2). Another avenue for 3D microstructure characterization, MicroCT, was pursued when the instrumentation became available.

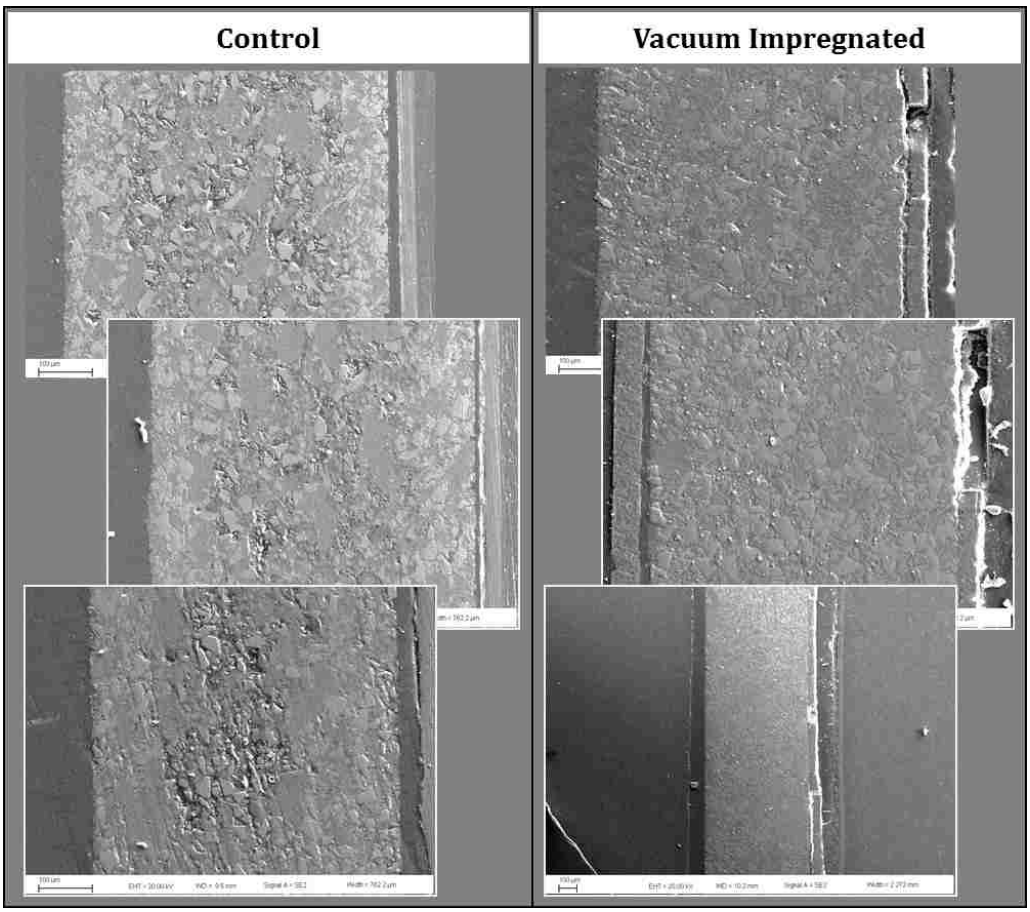

Figure D.1: Secondary SEM images of pellet cross-sections. The impregnated pellet was prepared with the optimized vacuum impregnation process. The control pellet shows pull-out and surface roughness that was nearly eliminated by the impregnation process.

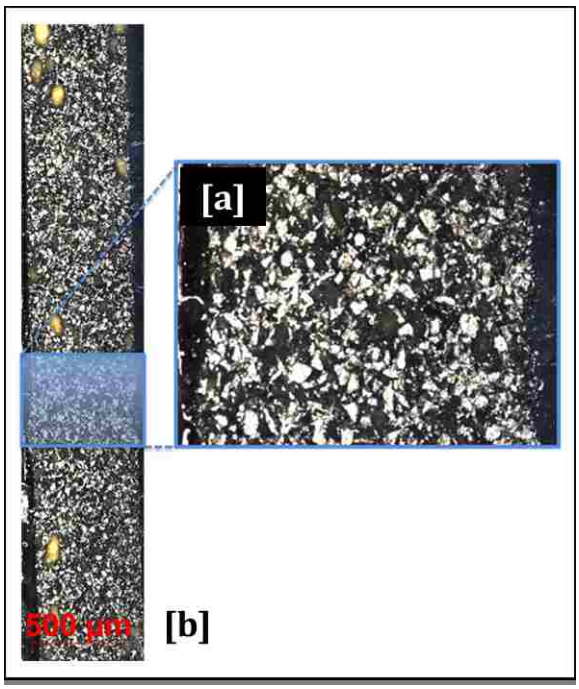

Figure D.2: One of the highest quality cross-sections as prepared and imaged by the Robo-Met.3D. Image [a] shows a magnified location from [b].

Bibliography

[1] Ronald A. Guidotti and Patrick Masset. Thermally activated ("thermal") battery technology: Part I: An overview. *J. Power Sources*, 161(2):1443–1449, 2006.

[2] C. M. Lamb. *Linden's Handbook of Thermal Batteries*, chapter "Thermal Batteries". McGraw-Hill, New York, 4th edition, 2011.

[3] S. Ghosh and D. Dimiduk, editors. *Computational Methods for Microstructure-Property Relationships*. Springer, New York, 2011.

[4] D. Linden and T. B. Reddy. *Linden's Handbook of Thermal Batteries*, chapter Basic Concepts. McGraw-Hill, New York, 4th edition, 2011.

[5] D. Linden and T. B. Reddy. *Linden's Handbook of Thermal Batteries*, chapter An Introduction to Primary Batteries. McGraw-Hill, New York, 4th edition, 2011.

[6] J. Phillips and S. Mohanta. *Linden's Handbook of Thermal Batteries*, chapter Nickel-Zinc Batteries. McGraw-Hill, New York, 4th edition, 2011.

[7] T. B. Reddy. *Linden's Handbook of Thermal Batteries*, chapter An Introduction to Secondary Batteries. McGraw-Hill, New York, 4th edition, 2011.

[8] Patrick J. Masset and Ronald A. Guidotti. Thermal activated ("thermal") battery technology: Part IIIa: FeS_2 cathode material. *J. Power Sources*, 177(2):595 – 609, 2008.

[9] R. A. Guidotti and F. W. Reinhardt. Deformation study of separator pellets for thermal batteries. Technical Report SAND 90-2318, Sandia Natl. Lab., Albuquerque, NM, 1995.

[10] C. W. Wang, K. A. Cook, and A. M. Sastry. Conduction in multiphase particulate/fibrous networks: Simulations and experiments on Li-ion anodes. *J.*

Electrochem. Soc., 150:A385–A397, 2003. `http://jes.ecsdl.org/content/150/3/A385` (accessed Oct 19, 2014).

[11] B. G. Streetman. *Solid State Electronic Devices.* Prentice Hall, Englewood Cliffs, NJ, 3rd edition, 1990.

[12] P.K. Abraitis, R.A.D. Pattrick, and D.J. Vaughan. Variations in the compositional, textural and electrical properties of natural pyrite: A review. *Int. J. Miner. Process.*, 74(1-4):41–59, 2004.

[13] R. A. Guidotti, F. W. Reinhardt, and W. F. Hammetter. Screening study of lithiated catholyte mixes for a long-life Li(Si)/FeS_2 thermal battery. Technical Report SAND 85-1737, Sandia Natl. Lab., Albuquerque, NM, 1988.

[14] G. L. Di Benedetto, R. R. Carpenter, D. B. Swanson, and B. D. Wightman. Enhanced nanostructuring of iron disulfide for thermal battery cathode materials. Orlando, FL, June 2014. Proc. Power Sources Conf., 46th.

[15] M. Au. Nanostructured thermal batteries with high power density. *J. Power Sources*, 115:360–366, 2003. `http://www.sciencedirect.com/science/article/pii/S0378775302006274` (accessed Sep 25, 2014).

[16] S. S. Wang. Rotating disk characterization of factors limiting the performance of Li/FeS_2 cells. *J. Electrochem. Soc.*, 135:1675–1678, 1988.

[17] H. Czichos, T. Saito, and L. Smith. *Springer Handbook of Materials Measurement Methods.* Springer Science+Business Media, Inc., Berlin, Heidelberg, 2006.

[18] Y. Chiang, D. P. Birnie, and W. D. Kingery. *Physical Ceramics: Principles for Ceramic Science and Engineering.* John Wiley & Sons, Inc., New York, 1997.

[19] L. J. van der Pauw. A method of measuring specific resistivity and Hall effect of discs of arbitrary shape. *Philips Res. Rep.*, 13:1–9, 1958.

[20] Digby D. Macdonald. Reflections on the history of electrochemical impedance spectroscopy. *Electrochim. Acta*, 51(8–9):1376 – 1388, 2006. Electrochemical Impedance Spectroscopy Selection of papers from the 6th International Symposium (EIS 2004) 16-21 May 2004, Cocoa Beach, FL, {USA}.

[21] M. Yamashita. Resistivity correction factor for four-probe method on circular semiconductors I. *Jpn. J. Appl. Phys.*, 26:1550–1554, 1987.

[22] E. Barsoukov and J. R. Macdonald. *Impedance Spectroscopy: Theory, Experiment, and Applications.* John Wiley & Sons, Inc., Hoboken, NJ, 2005.

[23] D. C. Giancoli. *Physics for Scientists and Engineers with Modern Physics*. Pearson Prentice Hall, Upper Saddle River, NJ, 4th edition, 2009.

[24] S. Torquato. *Random Heterogeneous Materials: Microstructure and Macroscopic Properties*. Springer, New York, 2002.

[25] S. Rul, F. Lefevre-schlick, E. Capria, Ch. Laurent, and A. Peigney. Percolation of single-walled carbon nanotubes in ceramic matrix nanocomposites. *Acta Mater.*, 52(4):1061–1067, 2004.

[26] Chunsheng Lu and Yiu-Wing Mai. Anomalous electrical conductivity and percolation in carbon nanotube composites. *J. Mater. Sci.*, 43(17):6012–6015, 2008.

[27] S.F. Wang and A.A. Ogale. Continuum space simulation and experimental characterization of electrical percolation behavior of particulate composites. *Compos. Sci. Technol.*, 46(2):93–103, 1993.

[28] X. Wu, S. Qi, J. He, and G. Duan. High conductivity and low percolation threshold in polyaniline/graphite nanosheets composites. *J. Mater. Sci.*, 45(2):483–489, 2010.

[29] M. Niklaus and H.R. Shea. Electrical conductivity and young's modulus of flexible nanocomposites made by metal-ion implantation of polydimethylsiloxane: The relationship between nanostructure and macroscopic properties. *Acta Mater.*, 59(2):830–840, 2011.

[30] Yun-Jia Li, Man Xu, Jun-Qiang Feng, and Zhi-Min Dang. Dielectric behavior of a metal-polymer composite with low percolation threshold. *Appl. Phys. Lett.*, 89(7), 2006.

[31] Qing Huang, Lian Gao, Yangqiao Liu, and Jing Sun. Sintering and thermal properties of multiwalled carbon nanotube-$BaTiO_3$ composites. *J. Mater. Chem.*, 15:1995–2001, 2005.

[32] L. Weber, J. Dorn, and A. Mortensen. On the electrical conductivity of metal matrix composites containing high volume fractions of non-conducting inclusions. *Acta Mater.*, 51(11):3199 – 3211, 2003.

[33] A. Mikrajuddin, F.G. Shi, S. Chungpaiboonpatana, K. Okuyama, C. Davidson, and J.M. Adams. Onset of electrical conduction in isotropic conductive adhesives: A general theory. *Mater. Sci. Semicond. Process.*, 2(4):309 – 319, 1999.

[34] A. Ochsner and T. Fiedler. *Cellular and Porous Materials*, chapter Effective Thermal Properties of Hollow-Sphere Structures: A Finite Element Approach, pages 31–72. Wiley-VCH, Weinheim, 2008.

[35] Msc nastran - multidisciplinary structural analysis.

[36] Ansys - simulation driven product development. Online.

[37] Marc. Online.

[38] Abaqus - dassault systemes. Online.

[39] Adina - finite element analysis software. Online.

[40] J. N. Reddy and D. K. Gartling. *The Finite Element Method in Heat Transfer and Fluid Dynamics*. CRC Press, Boca Raton, FL, 3rd edition, 2010.

[41] X. Cheng and A.M. Sastry. On transport in stochastic, heterogeneous fibrous domains. *Mech. Mater.*, 31(12):765–786, 1999.

[42] Florent Dalmas, Remy Dendievel, Laurent Chazeau, Jean-Yves Cavaille, and Catherine Gauthier. Carbon nanotube-filled polymer composites. Numerical simulation of electrical conductivity in three-dimensional entangled fibrous networks. *Acta Mater.*, 54(11):2923–2931, 2006.

[43] R.D. Bradshaw, F.T. Fisher, and L.C. Brinson. Fiber waviness in nanotube-reinforced polymer composites II: Modeling via numerical approximation of the dilute strain concentration tensor. *Compos. Sci. Technol.*, 63(11):1705–1722, 2003. Modeling and Characterization of Nanostructured Materials.

[44] Xi-Qiao Feng, Zhi Tian, Ying-Hua Liu, and Shou-Wen Yu. Effective elastic and plastic properties of interpenetrating multiphase composites. *Appl. Compos. Mater.*, 11(1):33–55, 2004.

[45] Scott A. Roberts, Victor E. Brunini, Kevin N. Long, and Anne M. Grillet. A framework for three-dimensional mesoscale modeling of anisotropic swelling and mechanical deformation in lithium-ion electrodes. *J. Electrochem. Soc.*, 161(11):p F3052–F3059, 2014.

[46] H. Mendoza, S. A. Roberts, V. Brunini, and A. M. Grillet. Mechanical deformation of lithium-ion electrode networks using reconstructed microstructures. Submitted for publication.

[47] Andreas H. Wiedemann, Graham M. Goldin, Scott A. Barnett, Huayang Zhu, and Robert J. Kee. Effects of three-dimensional cathode microstructure on the performance of lithium-ion battery cathodes. *Electrochim. Acta*, 88:580–588, 2013.

[48] J. Joos, T Carraro, M. Ender, B. Ruger, A. Weber, and E. I. Tiffée. Detailed microstructure analysis and 3D simulations of porous electrodes. *ECS Trans.*, 35(1):2357–2368, 2011.

[49] B. Ruger, B.ger, A. Weber, and E. Ivers-Tiffée. 3D-modelling and performance evaluation of mixed conducting (miec) cathodes. *ECS Trans.*, 7(1):2065–2074, 2007.

[50] C. Kreller, M. Drake, S. B. Adler, H. Chen, Yu He, K. Thornton, J. R. Wilson, and S. A. Barnett. Modeling SOFC cathodes based on 3-D representations of electrode microstructure. *ECS Trans.*, 35(1):815–822, 2011.

[51] J. C. Russ, editor. *The Image Processing Handbook*. CRC Press, Boca Raton, FL, 4th edition, 2002.

[52] J. C. Russ. *Practical Stereology*. Plenum Press, New York, 1986.

[53] M. Jutzeler, A.A. Proussevitch, and S.R. Allen. Grain-size distribution of volcaniclastic rocks 1: A new technique based on functional stereology. *J. Volcanol. Geotherm. Res.*, 239-240:1–11, 2012.

[54] D. E. Stephenson, B. C. Walker, C. B. Skelton, E. P. Gorzkowski, D. J. Rowenhorst, and D. R. Wheeler. Modeling 3D microstructure and ion transport in porous Li-ion battery electrodes. *J. Electrochem. Soc.*, 158(7):A781–A789, 2011.

[55] R. Edwin Garcia and Yet-Ming Chiang. Spatially resolved modeling of microstructurally complex battery architectures. *J. Electrochem. Soc.*, 154(9):A856–A864, 2007.

[56] Jiang Wei Wang, Yu He, Feifei Fan, Xiao Hua Liu, Shuman Xia, Yang Liu, C. Thomas Harris, Hong Li, Jian Yu Huang, Scott X. Mao, and Ting Zhu. Two-phase electrochemical lithiation in amorphous silicon. *Nano Lett.*, 13(2):709–715, 2013. PMID: 23323743.

[57] J. Alkemper and P. W. Voorhees. Quantitative serial sectioning analysis. *J. Microsc.*, 201(3):388–394, 2001.

[58] J. Alkemper and P. Voorhees. 3d material analysis, jun 2002. US Patent App. 09/747,493.

[59] Y. Adachi, N. Sato, M. Ojima, M. Nakayama, and Y. Wang. Development of fully automated serial-sectioning 3D microscope and topological approach to pearlite and dual-phase microstructure in steels. In *1st International Conference on 3D Materials Science 2012, 3DMS 2012*, pages 37–42, 2012.

[60] Jonathan E. Spowart, Herbert E. Mullens, and Brian T. Puchala. Collecting and analyzing microstructures in three dimensions: A fully automated approach. *JOM*, 55(10):35–37, 2003.

[61] J. M. Sosa, S. Koduri, V. Dixit, P. C. Collins, S. Niezgoda, S. R. Kalidindi, and H. L. Fraser. Application of novel techniques to the three-dimensional characterization of microstructural features in $\alpha + \beta$ titanium alloys. In *Microsc. Microanal.*, August 2010.

[62] Spowart J. E. Madison, J., D. J. Rowenhorst, and T. M. Pollock. The three-dimensional reconstruction of the dendritic structure at the solid-liquid interface of a Ni-based single crystal. *JOM*, 60(7):26–30, July 2008.

[63] P. Sudraud, G. Ben Assayag, and M. Bon. Focused-ion-beam milling, scanning-electron microscopy, and focused-droplet deposition in a single microcircuit surgery tool. *J. Vac. Sci. Technol., B*, 6(1):234–238, 1988.

[64] N. Gunda, C. Hae-Won, A. Berson, B. Kenney, K. Karan, J. Pharoah, and S. Mitra. Focused ion beam-scanning electron microscopy on solid-oxide fuel-cell electrode: Image analysis and computing effective transport properties. *J. Power Sources*, 196:3592–3603, 2011. `http://www.sciencedirect.com/science/article/pii/S0378775310022482` (accessed Sep 23, 2014).

[65] K. Matsuzaki, N. Shikazono, and N. Kasagi. Three-dimensional numerical analysis of mixed ionic and electronic conducting cathode reconstructed by focused ion beam scanning electron microscope. *J. Power Sources*, 196:3073–3082, 2011. `http://ac.els-cdn.com/S0378775310021348/1-s2.0-S0378775310021348-main.pdf?_tid=7103e100-4371-11e4-b342-00000aacb35d&acdnat=1411511703_b083c9e1a2e76decd4a67a0d3ffd53d4` (accessed Sep 23, 2014).

[66] K. Lee, N. Vito, and E. Wachsman. Comprehensive quantification of Ni-Gd0.1Ce0.9O1.95 anode functional layer microstructures by three-dimensional reconstruction using a FIB/SEM dual beam system. *J. Power Sources*, 228:220–228, 2013. `http://www.sciencedirect.com/science/article/pii/S0378775312018022` (accessed Sep 23, 2014).

[67] G. Nelson, W. Harris, J. Lombardo, J. Izzo, W. K. Chiu, P. Tanasini, M. Cantoni, J. V. Herle, C. Comninellis, J. Andrews, Yijin Liu, P. Pianetta, and

Y. Chu. Comparison of x-ray nanotomography and FIB-SEM in quantifying the composite LSM/YSZ SOFC cathode microstructure. *ECS Trans.*, 35(1):2417–2421, 2011.

[68] H. Iwai, N. Shikazono, T. Matsui, H. Teshima, M. Kishimoto, R. Kishida, D. Hayashi, K. Matsuzaki, D. Kanno, T. Saito, H. Muroyama, K. Eguchi, N. Kasagi, and N. H. Kasagi. Quantification of Ni-YSZ anode microstructure based on dual beam FIB-SEM technique. *ECS Trans.*, 25(2):1819–1828, 2009.

[69] K. Matsuzaki, D. Kanno, H. Teshima, N. Shikazono, and N. Kasagi. Three-dimensional numerical simulation of Ni-YSZ anode polarization using reconstructed microstructure from FIB-SEM images. *ECS Trans.*, 25(2):1829–1836, 2009.

[70] H. Choi, D. Gawel, A. Berson, J. Pharaoh, and K. Karan. Comparison between FIB-SEM experimental 3-d reconstructions of SOFC electrodes and random particle-based numerical models. *ECS Trans.*, 35(1):997–1005, 2011.

[71] B. Ruger, J. Joos, A. Weber, T. Carraro, and E. Ivers-Tiffée. 3D electrode microstructure reconstruction and modelling. *ECS Trans.*, 25(2):1211–1220, 2009.

[72] E. Wachsman and E. N. Armstrong. Towards a fundamental understanding of the oxygen reduction mechanism. *ECS Trans.*, 35(1):1955–1963, 2011.

[73] D. Gostovic, K. A. O'Hara, N. J. Vito, E. D. Wachsman, and K. S. Jones. Multiple length scale characterization of doped lanthanum manganate composite cathodes. *ECS Trans.*, 16(51):83–93, 2009.

[74] J. Wilson, W. Kobsiriphat, R. Mendoza, H. Chen, T. Hines, J. Hiller, D. Miller, K. Thornton, P. Voorhees, S. B. Adler, D. R. Mumm, and S. Barnett. Three dimensional reconstruction of solid oxide fuel cell electrodes using focused ion beam - scanning electron microscopy. *ECS Trans.*, 7(1):1879–1887, 2007.

[75] C. Ziegler, S. Thiele, and R. Zengerle. Direct three-dimensional reconstruction of a nanoporous catalyst layer for a polymer electrolyte fuel cell. *J. Power Sources*, 196:2094–2097, 2011. `http://www.sciencedirect.com/science/article/pii/S0378775310016502` (accessed Sep 23, 2014).

[76] Zhao Liu, J. Scott Cronin, Yu chen K. Chen-Wiegart, James R. Wilson, Kyle J. Yakal-Kremski, Jun Wang, Katherine T. Faber, and Scott A. Barnett. Three-dimensional morphological measurements of $LiCoO_2$ and $LiCoO_2/Li(Ni_{1/3}Mn_{1/3}Co_{1/3})O_2$ lithium-ion battery cathodes. *J. Power Sources*, 227:267–274, 2013.

[77] J. C. Elliott and S. D. Dover. X-ray microtomography. *J. Microsc.*, 126(2):211–213, 1982.

[78] David S. Eastwood, Vladimir Yufit, Jeff Gelb, Allen Gu, Robert S. Bradley, Stephen J. Harris, Daniel J. L. Brett, Nigel P. Brandon, Peter D. Lee, Philip J. Withers, and Paul R. Shearing. Lithiation-induced dilation mapping in a lithium-ion battery electrode by 3D X-ray microscopy and digital volume correlation. *Adv. Energy Mater.*, 4(4), 2014.

[79] F. R. Brushett, M. S. Naughton, J. W. D. Ng, L. Yin, and P. J. A. Kenis. Analysis of Pt/C electrode performance in a flowing-electrolyte alkaline fuel cell. *Int. J. Hydrogen Energy*, 37:2559–2570, 2012. `http://www.sciencedirect.com/science/article/pii/S0360319911024529` (accessed Nov 24, 2014).

[80] H. Jhong, F. R. Brushett, L. Yin, D. M. Stevenson, and P. J. A. Kenis. Combining structural and electrochemical analysis of electrodes using micro-computed tomography and a microfluidic fuel cell. *J. Electrochem. Soc.*, 159:B292–B298, 2012. `http://jes.ecsdl.org/content/159/3/B292` (accessed Dec 19, 2014).

[81] Carl Zeiss Microscopy GmbH. ZEISS Xradia 520 Versa Product Information, Version 1.1. `www.zeiss.com/microscopy/en_us/products/x-ray-microscopy` (accessed March 16, 2015).

[82] A M Soltan, W-A Kahl, M Wendschuh, and M Hazem. Microstructure and reactivity of calcined mud supported limestones. *Miner. Process. Extr. Metall.*, 121(1):5–11, 2012.

[83] K. Matuszewski, H. Matysiak, J. Jaroszewicz, W. De Nolf, K. Kubiak, and K. J. Kurzydlowski. Influence of bridgman process conditions on microstructure and porosity of single crystal Ni-base superalloy CMSX-4. *Int. J. Cast Met. Res.*, 27(6):329–335, 2014.

[84] M. Naveed Ahsan, Andrew J. Pinkerton, Richard J. Moat, and Judith Shackleton. A comparative study of laser direct metal deposition characteristics using gas and plasma-atomized Ti-6Al-4V powders. *Mater. Sci. Eng., A*, 528(25-26):7648–7657, 2011.

[85] Garcia-Gil, Eva Santos-Garcias, Elena Fulladosa, Janine Laverse, Matteo Alessandro Del Nobile, and Pere Gou. High pressure induces changes in texture and microstructure of muscles in dry-cured hams. *Innovative Food Sci. Emerging Technol.*, 22:63–69, 2014.

[86] Inc. Minitab. Minitab statistical software - minitab. Online.

[87] Gilson Company, Inc. ASTM Test Sieves. `www.globalgilson.com/astm-test-sieves` (accessed Apr 8, 2014).

[88] Scribner Associates. Software downloads: Zplot and zview. Online.

[89] *Avizo 9 User's Guide*. Konrad-Zuse-Zentrum fur Informationstechnik Berlin (ZIB), Germany and FEI, SAS, 2015.

[90] G. H. Bagheri, C. Bonadonna, I. Manzella, and P. Vonlanthen. On the characterization of size and shape of irregular particles. *Powder Technol.*, 270:141–153, 2015. `http://www.sciencedirect.com/science/article/pii/S0032591014008651` (accessed Aug 6, 2015).

[91] P. K. Notz, S. R. Subia, M. M. Hopkins, H. K. Moffat, and D. R. Noble. SIERRA Multimechanics Module: Aria User Manual - Version 4.34. Technical Report SAND 2007-xxxx, Sandia Natl. Lab., Albuquerque, NM, August 2014.

[92] Cubit 15.0 user documentation. Online.

[93] D. Noble, E. Newren, and J. Lechman. A conformal decomposition finite element method for modeling stationary fluid interface problems. *Int. J. Numer. Methods Fluids*, 63:725–742, 2010.

[94] Jeremy B. Lechman, Martin B. Nemer, and David R. Noble. Toward application of conformal decomposition finite elements to non-colloidal particle suspensions. *Int. J. Numer. Methods Fluids*, 68(11):1409–1421, 2012.

[95] D. Sangeeta and J. R. LaGraff. *Inorganic Materials Chemistry Desk Reference*. CRC Press, Boca Raton, FL, 2nd edition, 2005.

[96] W. D. Callister. *Materials Science and Engineering: An Introduction*. John Wiley & Sons, Inc., New York, 4th edition, 1997.

[97] M. Ostoja-Starzewski and J. Schulte. Bounding of effective thermal conductivities of multiscale materials by essential and natural boundary conditions. *Phys. Rev. B*, 54:278–285, 1996. `http://journals.aps.org/prb/pdf/10.1103/PhysRevB.54.278` (accessed May 12, 2015).

[98] Welcome to python.org. Online.

[99] T. Kanit, S. Forest, I. Galliet, V. Mounoury, and D. Jeulin. Determination of the size of the representative volume element for random composites: Statistical and numerical approach. *Int. J. Solids Struct.*, 40:3647–3679, 2003. (accessed July 30, 2015).

[100] A. P. Chandra and A. R. Gerson. The mechanisms of pyrite oxidation and leaching: A fundamental perspective. *Surf. Sci. Rep.*, 65:293–315, 2010. (accessed Aug 26, 2015).

[101] J. R. Reitz, F. J. Milford, and R. W. Christy. *Foundations of Electromagnetic Theory*. Addison-Wesley Publishing Company, Inc., Reading, MA, 4th edition, 1979.